Faculty of Science and Technology

Vertical nitrate fluxes in the Arctic Ocean

—

Achim Randelhoff

A dissertation for the degree of Philosophiae Doctor – December 2016

Cover photo by Birgit Nesheim

Vertical Nitrate Fluxes in the Arctic Ocean

Achim Randelhoff

December 2016, Tromsø, Norway

UNIVERSITETET I TROMSØ

NORSK·POLARINSTITUTT

SUPERVISION

DR. ARILD SUNDFJORD
Norwegian Polar Institute

PROF. MARIT REIGSTAD
Department of Arctic and Marine Biology, University of Tromsø

PROF. ILKER FER
Geophysical Institute, University of Bergen, and
Bjerknes Centre for Climate Research

PROF. ODD ERIK GARCIA
Department of Physics and Technology, University of Tromsø

Ipsa quoque adsiduo labuntur tempora motu,
non secus ac flumen. Neque enim consistere flumen
nec levis hora potest, sed ut unda inpellitur unda
urgeturque eadem veniens urgetque priorem,
tempora sic fugiunt pariter pariterque sequuntur
et nova semper; nam quod fuit ante, relictum est,
fitque, quod haud fuerat, momentaque cuncta novantur.

—P. OVIDII NASONIS Metamorphoseon Liber XV

SUMMARY

Upward mixing of remineralized nutrients is essential for photosynthesis in the upper ocean. Weak vertical mixing, which restricts nutrient supply, and sea ice, which leads to low light levels, conspire to severely inhibit marine primary productivity in the Arctic Ocean. However, little has been known about their relative contributions. No large-scale quantitative estimates of the vertical nutrient supply had previously been presented, which has impeded an understanding of its role in shaping the ecology and carbon cycle of the Arctic Ocean.

In order to estimate the vertical flux of nitrate into the surface layer in contrasting hydrographic and dynamic regimes, profiles of turbulent microstructure and nitrate concentrations were measured as part of a number of cruises and ice camps in the area extending from eastern Fram Strait into the Nansen Basin. These have been supplemented with obervations of the seasonal nutrient cycle at a mooring in the same area, and a reanalysis of available data on nitrate concentrations and turbulent mixing in other parts of the central Arctic Ocean.

Hydrography was found to be the biggest driver of variability in nitrate fluxes. Strong stratification, wherever encountered, restricted nitrate supply, often in concert with concurrently weak turbulent mixing, both in the seasonal nitracline (0.3–0.7 mmol N m^{-2} d) and the deep basin (0.01–0.2 mmol N m^{-2} d). Thus deep winter mixing supplies the bulk of the nitrate pool on the relatively productive shelves (e.g. 2.5 mmol N m^{-2} d in the inflow of Atlantic Water during winter), but in the strongly stratified Canadian Basin, fluxes are low year-round (on the order of 0.01 mmol N m^{-2} d) and place a tight limit on new production. Only the weakly stratified Atlantic derived water in the Nansen Basin close to Fram Strait seems to have a certain potential to support future increases in new production under a seasonal ice cover.

LIST OF PAPERS

I Randelhoff, A. and J. D. Guthrie (2016), Regional patterns in current and future export production in the central Arctic Ocean quantified from nitrate fluxes, *Geophysical Research Letters*, *43*, 8600–8608, doi:10.1002/2016gl070252.

II Randelhoff, A., A. Sundfjord, and M. Reigstad (2015), Seasonal variability and fluxes of nitrate in the surface waters over the Arctic shelf slope, *Geophysical Research Letters*, *42*, 3442–3449, doi:10.1002/2015gl063655.

III Randelhoff, A., I. Fer, and A. Sundfjord, Turbulent upper-ocean mixing affected by meltwater layers during Arctic summer, *revised manuscript submitted to Journal of Physical Oceanography*.

IV Randelhoff, A., I. Fer, A. Sundfjord, J.-É. Tremblay, and M. Reigstad (2016), Vertical fluxes of nitrate in the seasonal nitracline of the Atlantic sector of the Arctic Ocean, *Journal of Geophysical Research: Oceans*, *121*, 5282–5295, doi:10.1002/2016JC011779.

CONTENTS

1

Introduction and Background

1.1 Vertical fluxes and primary production

The growth of marine phytoplankton is confined to the uppermost layer of the ocean called the euphotic zone. Organic matter has a tendency to sink and thus exports essential nutrients to depth. This flux is called export production. In this way, the world ocean is partitioned into a photic, nutrient poor surface layer and the aphotic, nutrient rich deeper layers. Without any further exchange processes between these two pools, nutrients would be quickly buried in the sea floor and not support photosynthesis. An upward flux of nutrients is therefore crucial for maintaining primary production in the ocean (Margalef, 1978). The new production is limited by the net community production, i.e. the net increase in primary producer's biomass that can then be exported (see text box below).

Especially in the oligotrophic ocean, the vertical supply of inorganic nutrients constrains new production. Lewis et al. (1986) showed that the upward flux of nitrate matched its uptake by primary producers. Christian et al. (1997) found that the slower remineralization of carbon with depth matched the stoichiometry of carbon, nitrogen and phosphorus in the upward fluxes. The export of particulate matter thereby helps removing carbon from the surface layer and thus the atmosphere. Upward mixing of deeper water and its nutrients provides the lever on this process dubbed the biological pump, which represents the oceanic buffering capacity of atmospheric levels of carbon dioxide. The present and future of the nutrient supply to the photic zone in the world ocean has also received considerable attention regarding the future of marine ecosystems, since changes in the nutrient loading will have the ability to drive marked changes in the marine community structure (e.g. Li et al., 2009; Peter and Sommer, 2013; Sommer et al., 2016).

The upward flux can be both advective (like coastal upwelling or Ekman

The many measures of primary production

Net primary production (NPP) is all assimilation of inorganic nutrients into organic matter, adjusted only for autotrophic respiration, that is, respiration by the primary producers themselves. The production that is based on allochthonous nutrients (i.e., nutrients not formed locally; in practice taken to be nitrate) is termed "new production" (NP), while the remainder is "regenerated production", generally taken to result from uptake of ammonium (Dugdale and Goering, 1967). In this framework, only new production can contribute to vertical export of nutrients when the budget is balanced over several years. The net community production (NCP) is the primary production adjusted for all respiration, both by autotrophs and heterotrophs. NCP is then the upper limit of export production (Eppley and Peterson, 1979).

pumping) or diffusive (like turbulent mixing). In the absence of conditions consistently favourable for upwelling (such as coastal upwelling zones, subpolar gyres, and cyclonic eddies), turbulent (diapycnal) diffusion accounts for most of this upward transport. Importantly, strong stratification reduces the vertical mixing coefficient (Section 2.3), which in the Arctic Ocean (AO) restricts the nitrate flux into the photic zone.

1.2 Hydrographic setting

The Arctic Ocean's hydrography is dominated by the input of three distinct water masses: Warm, Atlantic Water through Fram Strait and the Barents Sea, relatively fresh Pacific Water through Bering Strait and river freshwater runoff, mainly through the Siberian and (to a smaller extent) the Canadian shelf (e.g. Dickson et al., 2007; Woodgate, 2013). The relatively weakly stratified Atlantic-derived water spreads along the eastern margins of the deep basin, while strongly stratified Pacific derived water masses spread into the western parts of the deep basin (e.g. Rudels et al., 2004, 2015). Thus deep winter mixed layers prevail in the East, and strong perennial stratification in the West (Fig. 1.1). On top of that comes the seasonal progression of sea ice melt derived freshwater input into the upper ocean, which is presented in Section 1.3. The seasonal pycnocline forms only in the summer months and does not significantly influence the overall shape of the nitrate gradient across the deeper, perennial pycnocline that is evident for the Nansen and Amundsen Basin profiles in Fig. 1.1.

As we will see in Section 3, the distinction between seasonal and perennial stratification gives rise to two distinct types of nitraclines, seasonal and perennial. A discussion of the implications of the hydrography for vertical and lateral gradients of nutrient concentrations can be found in Section 3.

1.3 The seasonal cycle

Due to the seasonal cycle of sunlight, photosynthesis at high latitudes is concentrated around a few summer months. Accordingly, concentrations of both phytoplankton and nutrients in the upper ocean vary mainly with seasons. In the spring, the nutrient pool is rapidly depleted, often aided by an explosive spring bloom. Throughout summer, nutrient concentrations remain low and the ecosystem switches to a recycling state, relying on regenerated nutrients (e.g., ammonium, NH_4^+). In fall, primary production ceases again, and the mixed layer nutrient pool is replenished to the concentrations it had at the end of the previous winter.

The abundance of nutrients in this pool is an important factor in spring blooms, but exactly what is responsible for the timing of the spring bloom, remains controversial (see e.g. Behrenfeld and Boss, 2014). A recurring theme are however intensities and depths of mixing, often related to the restratification of the water column (e.g. Sverdrup, 1953; Huisman et al., 1999). In the Arctic Ocean, phytoplankton blooms are often associated with retreat of the ice cover (Perrette et al., 2011). As ice melt implies both an increase in the amount of photosynthetically available radiation and an increasingly stable stratification, it is not straightforward to distinguish between light or mixing as triggering mechanisms in the field.

1.4 Approach and objectives

Dissolved inorganic nitrogen is, in most instances, the limiting nutrient in the Arctic Ocean (Tremblay and Gagnon, 2009, and references therein), so nitrogen is usually used as the base "currency" of biogeochemical models of the Arctic Ocean (see e.g. Popova et al., 2012; Slagstad et al., 2015). In addition, availability of high-quality optical nitrate sensors (Johnson and Coletti, 2002, and subsequent publications by this group) makes it possible to autonomously record high-resolution nitrate concentration data without the need for wet chemistry. This allowed us to measure nitrate concentration and gradients at a much greater vertical, lateral and temporal resolution than could be afforded by traditional bottle samples. The quantification of vertical nitrate fluxes can serve as a means to study the effects of turbulence and hydrography on primary production because organic matter is often found to follow a fixed stoichiometry, the so-called "Redfield ratio" (see the seminal paper by Redfield et al., 1963). While the importance of the vertical nitrate flux for Arctic marine ecology and nutrient cycling is frequently stressed, it has largely remained unquantified so far (Tremblay et al., 2015, but see Bourgault et al. (2011) for an exception).

The main objective of this dissertation is precisely to fill that gap, that is to quantify the vertical turbulent nitrate supply to the photic zone, both on a seasonally stratified inflow shelf (the Barents Sea shelf slope area) and in the perennially stratified deep Arctic Ocean. The hydrography and mixing in the seasonally stratified upper Arctic Ocean will be of particular importance to understand the physical environment in which marine primary producers grow. Along the way, I describe both large-scale patterns and the seasonal distribution of NO_3^- concentrations around the Barents Sea shelf slope, and place these in a pan-Arctic context.

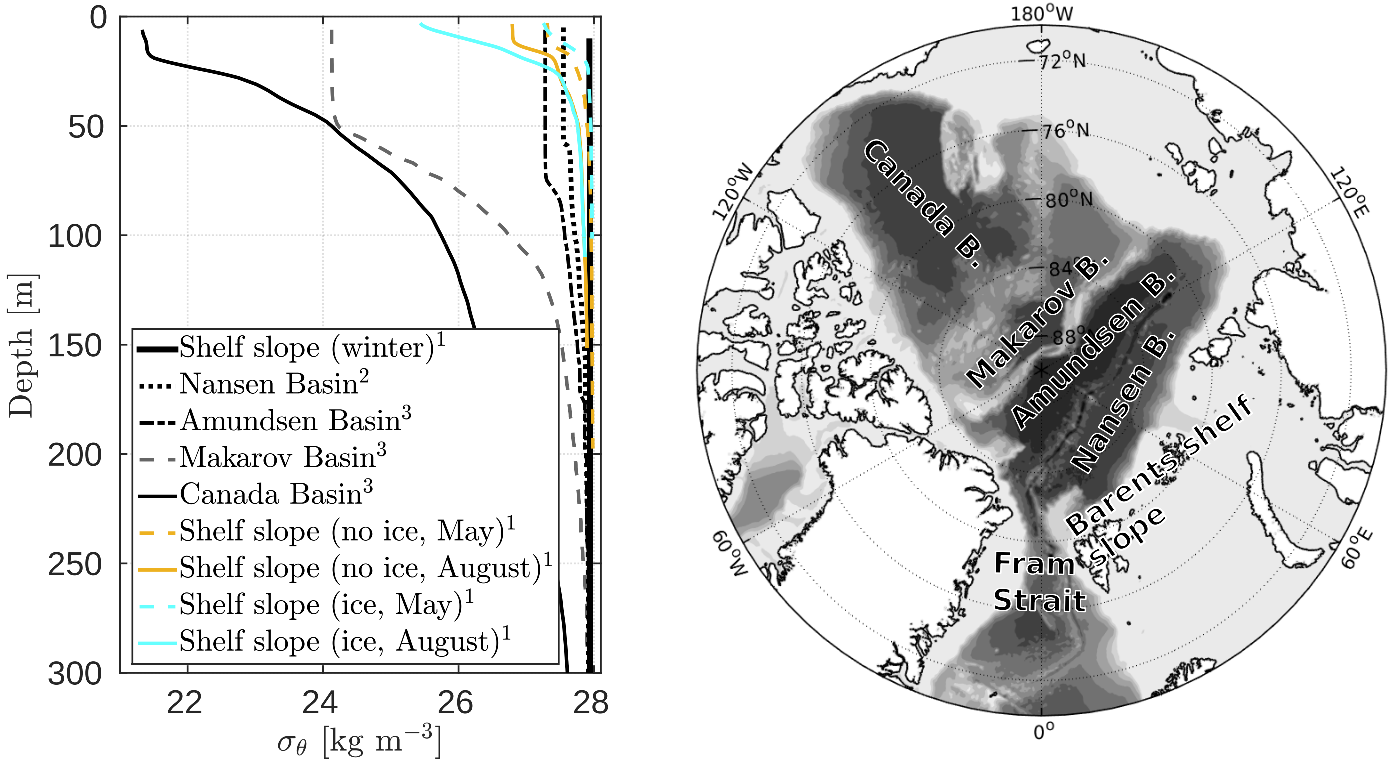

Figure 1.1: Representative profiles of potential density (σ_θ) across the Arctic Ocean in different seasons. All black and grey lines represent winter profiles; orange and cyan signify the seasonal evolution in the shelf break area. [1] Fram Strait area (Carbonbridge), [2] N-ICE2015 (`https://data.npolar.no/dataset/92262a9c-e6a4-59b5-9929-81c0429d7de6`), [3] `https://arcticdata.io/catalog/#view/doi:10.18739/A2HK6Z`

2

METHODS

2.1 THE WHAT AND HOW OF TURBULENT NITRATE FLUXES

To my knowledge, the direct measurement of turbulent nitrate fluxes has so far not been attempted because sampling frequency and instrument accuracy of currently available sensors are not sufficient to measure small-scale turbulent fluctuations in nitrate concentrations. A convenient method for ship-based campaigns is the combination of vertical profiles of velocity microstructure and nitrate concentrations ($\mathcal{N}$). This method relies heavily on parameterizing the vertical eddy diffusivity K_ρ (the proportionality constant between flux and mean-field gradient of a quantity, units of $\mathrm{m^2\ s^{-1}}$) from the dissipation of turbulent kinetic energy ϵ ($\mathrm{W\ kg^{-1} \equiv m^2\ s^{-3}}$) and mean-field stratification, using an empiric formula (see Section 2.3). Then, combining K_ρ with the vertical gradient of nitrate concentration ($\mu\mathrm{M\ m^{-1}}$), the vertical turbulent nitrate flux is

$$\mathrm{F}_{\mathcal{N}} = K_\rho \frac{\partial \mathcal{N}}{\partial z} \tag{2.1}$$

in units of mmol N $\mathrm{m^{-2}}$ d. As mentioned previously, we can convert between carbon and nitrogen units by assuming a constant fixed ratio between the constituting elements of organic matter. Although the Redfield ratio (see Section 1.4) seems to depend on type of the organic matter and environmental conditions (e.g. STERNER et al., 2008; TAMELANDER et al., 2013; FRIGSTAD et al., 2014), such disputes concern relatively small corrections to the C:N ratios published in the literature, certainly smaller than the uncertainties in the estimation of turbulent fluxes. Giving the nitrate flux in units of g C $\mathrm{m^{-2}\ yr^{-1}}$ (1 g C $\mathrm{m^{-2}\ yr^{-1}} \approx 0.035$ mmol N $\mathrm{m^{-2}}$ d), our studies **I**, **II** and **IV** put the vertical nitrate flux into the context of other estimates of primary production.

2.2 FIELD WORK AND DATA SETS

Data for this thesis were collected during a total of five different campaigns associated with three different projects: Carbonbridge, N-ICE2015 and

TransSIZ (Table 2.1 and Fig. 2.1). All of them had a strong component focused on various aspects of the biogeochemical regime of physical-biological interactions in the Atlantic Arctic.

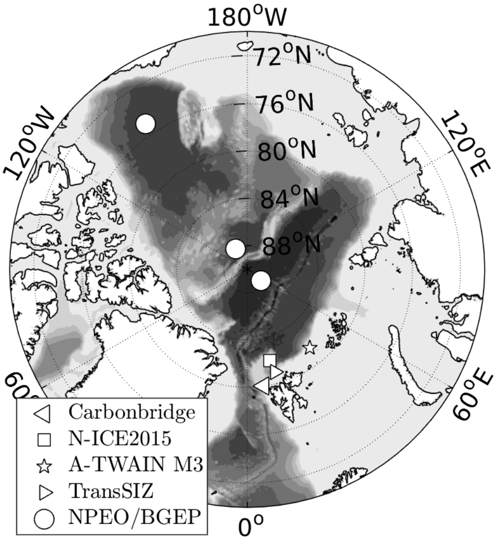

Figure 2.1: Overview map indicating areas where individual projects where conducted. Details about seasonal and regional coverage of campaigns other than NPEO/BGEP (North Pole Environmental Observatory, Beaufort Gyre Exploration Project) are presented in Table 2.1. The latter indicate only a reanalysis of existing data collected by projects the author is not affiliated with.

For the Carbonbridge project, data were collected on three different cruises in January, May and August 2014, covering the Marginal Ice Zone in Fram Strait and the shelf slope area north of Svalbard with a combination of cross-shelf slope transects and 24-hour process stations. The field measurements conducted for the N-ICE2015 project were distributed over successive ice camps in the period January till June 2015 in the pack ice north of Svalbard. From the TransSIZ campaign, only a single transect of NO_3^- concentration profiles was used to supplement the discussion of large-scale patterns in NO_3^- distribution (**IV**).

2.3 TURBULENT MICROSTRUCTURE

Microstructure shear, conductivity and temperature were measured using a loosely tethered microstructure profiler MSS-90L (IWS Wassermesstechnik, Germany) with two airfoil shear probes, falling freely at a constant rate between 0.55 and 0.85 m s^{-1}. Using the small-scale shear, one can infer

Table 2.1: Data sets collected for this thesis.

Campaign/Data set	Season[1]	Area[2]	Ice	Vessel
Carbonbridge (2014)				R/V Helmer Hanssen
January	Winter	Shelf, shelf slope	Open water	
May	Spring	Shelf, shelf slope	MIZ[3,4]	
August	Summer	Shelf, shelf slope	MIZ[3,4]	
N-ICE (2015)				R/V Lance
January – March	Winter	Basin	Pack ice	
April – mid-May	Winter	Plateau	Pack ice	
mid-May – June	Spring	Plateau & shelf slope	Pack ice&MIZ[3]	
TransSIZ	Winter, spring	Shelf, shelf slope, plateau	Pack ice	R/V Polarstern
A-TWAIN M3[5]	1 entire year	shelf slope (800 m isobath)		mooring

[1] Winter: No ice melt, spring: ice melt started within the last weeks, summer: ice melt started several months ago, severe nutrient depletion in the upper layers

[2] Nansen Basin, Yermak Plateau, shelf and shelf slope of the northern Barents Sea

[3] Marginal Ice Zone.

[4] also included open water stations

[5] selected mooring on the Barents sea shelf slope

the vertical eddy diffusivity, K_ρ, used in calculation of nutrient fluxes. The microstructure sampling was usually made in sets of at least three consecutive repeat profiles at any given station.

MSS data were processed following Fer (2006) for all data sets included in **I-IV**. Briefly, assuming local small-scale isotropy (Yamazaki and Osborn, 1990), dissipation of turbulent kinetic energy was estimated from the measured microscale shear as

$$\epsilon = 7.5\nu\langle(\partial_z u')^2\rangle, \tag{2.2}$$

where ν is the molecular viscosity of sea water and $\partial_z u'$ the turbulent shear. Combining turbulent microstructure with stratification, the eddy diffusivity of mass is estimated as

$$K_\rho = \Gamma\frac{\epsilon}{N^2} \tag{2.3}$$

following Osborn (1980), where $N^2 = -\frac{g}{\rho}\frac{\partial\rho}{\partial z}$ defines the buoyancy frequency N using gravitational acceleration g and water density ρ. The magnitude of the factor Γ and its dependence on other parameters is the subject of current research (e.g. Salehipour et al., 2016), but the work presented in this thesis employs the canonical value of 0.2 put forward by Osborn (1980), which represents the upper bound of an average over long spatial and temporal scales. Drawing on the Reynolds analogy for fully turbulent flows, it is then generally assumed that this eddy diffusivity is the same for all scalar tracers such as mass, heat, and dissolved salts like nitrate.

2.4 Sensor-based nitrate measurements

Vertical profile of nitrate concentrations ($\mathcal{N}$) were measured using the ISUS V3 (In-Situ Ultraviolet Spectrophotometer; Satlantic). The ISUS was used in various configurations based on campaign and setting. When deployed from one of the large vessels, it was mounted on the shipboard SBE911+ (Sea-Bird Electronics, USA) CTD (conductivity-temperature-depth) rosette system logging the analog output voltage of the unpumped ISUS. During the N-ICE2015 drift, the ISUS was deployed from a tent through a hole in the ice. Again, it was used in an unpumped configuration, mounted on a frame together with an SBE19+ system that was programmed to sample the analog output voltage of the ISUS. On the mooring array described in **II**, the ISUS was mounted 1 m below an SBE16plusV2 instrument (SeaCAT). The simultaneous acquisition of temperature and salinity data is crucial to all deployments in order to subtract seawater absorption from the absorption spectra following SAKAMOTO et al. (2009). A detailed account of ISUS and CTD data processing and quality screening is given in the Appendix of **IV**.

3

FINDINGS

3.1 PATTERNS ACROSS THE ARCTIC OCEAN

In the Atlantic sector, a striking pattern in the lateral distribution of nitrate is the contrast between the shelves and the deeper basins. While the central Arctic Ocean is perennially stratified and thus has a perennial nitracline (**I**, **IV**), the upper shelf slope and the Barents shelf themselves are seasonally stratified (**IV**), with no or very weak stratification during the winter (LOENG, 1991). In fact, replenishment and complete vertical homogenization of the surface nitrate pool in the Atlantic inflow already happens by early winter around November/December (**II**). This means that in the shelf slope area around Svalbard, the annual NCP is supported mostly by the vertical homogenization during fall and winter, likely aided by increased wind mixing in fall and thermal convection in the weakly temperature-stratified Atlantic Water (**II**).

Across the central Arctic Ocean, there are large-scale patterns in hydrography and turbulent mixing. Going from the Yermak Plateau via the Nansen, Amundsen and Makarov to the Canada Basin, stratification strengthens and dissipation decreases. Accordingly, also $F_{\mathcal{N}}$ decreases from the eastern ($F_{\mathcal{N}}$ equivalent to as much as 7.0 g C m^{-2} yr^{-1} close to the Yermak Plateau) to the western ($\approx$ 0.5 g C m^{-2} yr^{-1}, an order of magnitude less than what LEWIS et al. (1986) inferred for the oligotrophic North Atlantic) regions of the central Arctic Ocean. We calculated the Redfield-equivalent of the area-weighted average turbulent vertical nitrate supply to be in the range 1–2 g C m^{-2} yr^{-1} (**I**). Factoring in a range of other processes like horizontal advection, winter convection, and nitrogen fixation, we estimate the overall new production in the central Arctic Ocean that is exported across the nitracline to be in the range 1.5–3.0 g C m^{-2} yr^{-1}. The magnitude of these export fluxes is still extremely small relative to other areas of the world ocean (e.g. HONJO et al., 2008). Our estimates suggest that $F_{\mathcal{N}}$ is more important than previous comparisons of vertical (diffusive) with the lateral (advective) fluxes had suggested for the central Arctic Ocean

(ANDERSON et al., 2003). More importantly, our methodology makes it possible to not only estimate the present-day $F_{\mathcal{N}}$, but also the maximum fluxes that a given stratification and mixing scenario could support, all other factors permitting. These maximum fluxes correspond to a scenario where enhanced light input, seasonal (summertime) mixing and the export efficiency act to make all nitrate in the Polar Mixed Layer accessible to export production. This provides a quantitative handle on the issue of nutrient vs. light limitation. Using our formalism, we concluded that the Amundsen and Canadian Basins are nutrient-limited, and only close to the Atlantic inflow around the Yermak Plateau and the shelf break is light currently a limiting factor for new production.

3.2 SEASONAL STRATIFICATION AND UPPER-OCEAN MIXING

Summertime upper-ocean hydrography in the seasonal ice zone is dominated by the formation of freshwater layers deriving from sea ice melt (**III**). In general, directly wind driven dissipation is restricted to the uppermost parts of such meltwater layers, below which dissipation scales with buoyancy frequency in a manner consistent with the dissipation of narrow-band internal waves, possibly near-inertial. Thus, effectively, the nitracline is decoupled from the enhanced mixing of the surface layer throughout later parts of the melt season. Based on hydrographic considerations, we expect these mechanisms to extend to other areas of the Arctic that are only seasonally stratified.

Across the data sets considered in this thesis, it was found that upper ocean nitrate drawdown was strongly linked to the onset of stratification (**IV**, Fig. 5). This was demonstrated clearly as we encountered a pre-bloom situation in the core of the inflowing Atlantic Water in Fram Strait in May, while freshwater-induced stratification further west was directly coupled to waters where nitrate had been consumed. Nitrate fluxes through the summertime nitracline in the Atlantic sector were found to depend primarily on the presence of ice cover, where fluxes under sea ice were measured to be half as large as in open water (**IV**). However, the reason is not reduced dissipation in ice covered conditions due to suppression of surface waves, Langmuir circulation etc, but rather that stratification is enhanced under sea ice due to continued input of meltwater (**III**). Although stratification in the Marginal Ice Zone in late summer is generally stronger than in spring when melt has just started, this difference is hardly noticeable in the nitrate fluxes. The reason is that as the season progresses, the nitracline migrates downward to below the pycnocline (**IV**), which itself remains shallow due to continued ice melt (**III**).

3.3 CONCEPTUAL FRAMEWORK

Because the turbulent nitrate flux depends on the magnitude of the gradient in NO_3^- concentrations, the seasonality of the nutrient concentrations is also reflected in the seasonality of the turbulent nutrient fluxes. However, due to the vertical structure in both mixing and nitrate gradients, one has to pay attention to the vertical level at which fluxes are computed in order to interpret them correctly.

The deep nitraclines of the central Arctic Ocean are removed from the direct influence of (potentially ice mediated) wind forcing, and thus the associated nitrate fluxes act with a similar magnitude year-round (Fig. 3.1 C, bottom). This maintains the interannually steady concentration of nitrate in the Polar Mixed Layer. A slight seasonality in fluxes could potentially stem from seasonally varying input of near-inertial energy due to changing ice concentrations (RAINVILLE and WOODGATE, 2009), or deep winter mixing reaching the perennial pycnocline (POLYAKOV et al., 2013).

Embedded in the upper layers are seasonal processes: The depth-integrated drawdown of nitrate is concentrated around the spring bloom (Fig. 3.1 C, top). The drawdown that happens during the summer is in theory constrained by the vertical flux through the nitracline (Fig. 3.1 C, second from top). First with fall and winter mixing, $F_{\mathcal{N}}$ becomes large enough to replenish the surface layer's nitrate pool. At the lowermost extent of the seasonal nitracline, fluxes only become noticeable in fall, and stand for the complete homogenization of the upper ocean (Fig. 3.1 C, third from top). What all four curves in Fig. 3.1 C have in common is that their annual integrals are equal to each other and to the end-of-season nitrate drawdown (e.g. CODISPOTI et al., 2013).

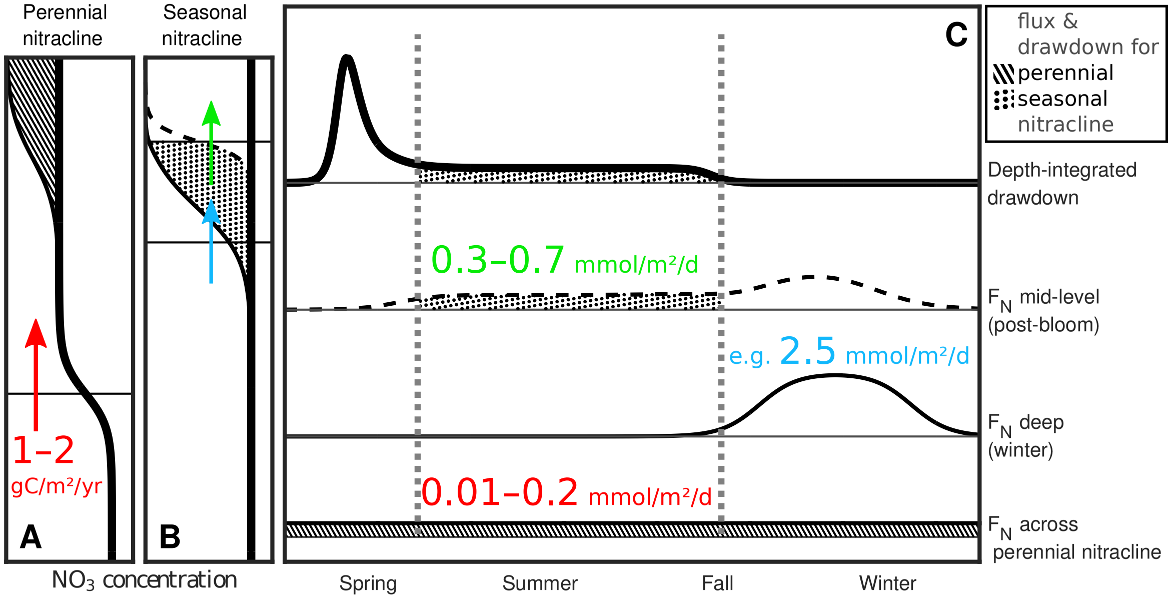

Figure 3.1: Conceptual framework for nitrate fluxes. A,B: Schematic vertical profiles of nitrate concentration. A: Scenario with perennial stratification, thick and thin lines represent winter and summer concentrations, respectively. Number is the Redfield-equivalent nitrate flux averaged across the deep Arctic Ocean (**I**). B: Scenario of seasonal nitrate drawdown. Thick, dashed and thin lines are winter, post-bloom and end-of-summer profiles, respectively. C: Annual cycles of upward nitrate fluxes evaluated at various depths. From top to bottom: Depth-integrated nitrate drawdown (≡consumption), $F_{\mathcal{N}}$ through the seasonal nitracline (green), $F_{\mathcal{N}}$ at the base of the seasonal nitracline (blue), and $F_{\mathcal{N}}$ through the perennial nitracline (red). Numbers indicate observed ranges of the individual fluxes estimated in papers **I**, **II** and **IV**. The shaded regions have equal areas for each of the different shadings.

4

PERSPECTIVES

4.1 VERTICAL NITRATE FLUXES AS A FRAMEWORK FOR STUDYING PRIMARY PRODUCTION

Traditionally, primary production is thought of as a composite process whose magnitude is set by a range of environmental parameters like nutrient loading, temperature, photosynthetically available radiation, and community structure, among other things (see e.g. VALIELA, 2015). This necessitates detailed and time-intensive measurements of e.g. nutrient uptake and primary production rates, all of which can vary greatly in time and space (e.g. MACKAS et al., 1985; ABBOTT, 1993). However, general circulation-biogeochemical coupled models fundamentally disagree about the future of Arctic marine primary production, largely due to different representations of vertical mixing processes (VANCOPPENOLLE et al., 2013). Constraining the vertical fluxes of nutrients and organic matter offers the chance to disentangle the imbalance between vertical supply of nutrients and primary production that leads to the large discrepancies in upper ocean nutrient inventories frequently observed in coupled biogeochemical models (POPOVA et al., 2012).

Instead of considering the host of biological processes that occur as a part of primary production in a food web, in this thesis I attempt to constrain the processes in the euphotic zone by the nutrient input through upward fluxes. These have to match the output at least approximately if a steady state is to be maintained. Since turbulent mixing is largely determined by physical processes, it is easier to estimate and more accessible to quantitative prediction at larger scales. This gives direct access to seasonal and annual integrals of nutrient fluxes and thus key terms of budgets in the nutrient cycle. The approach taken is therefore explicitly bottom-up. Neglecting top-down effects such as zooplankton grazing or viral mortality is only possible due to the focus on new production which enforces a strict nutrient budget perspective on all involved processes.

Hydrographic conditions vary widely across the Arctic Ocean, both in the annual mean and the seasonal cycle. Vertical homogenization in winter, wherever occurring, means that NCP has access to the entire nutrient reservoir in the water column, and thus even though summertime meltwater induced stratification might be strong and limit nutrient fluxes, annual integrals of $F_{\mathcal{N}}$ are large. It is not the case that the vertical turbulent nutrient supply to the photic zone in the Arctic Ocean is low because of strong stratification as such, as is commonly claimed in the literature. As we showed, $F_{\mathcal{N}}$ in the central Arctic is low primarily because of little mixing, not because of strong stratification (relative to other regions[1]). This is a crucial distinction as stratification and mixing are two distinct, albeit overlapping issues. However, the strong stratification is presumably at least co-responsible for creating such a quiescent environment (e.g. LINCOLN et al., 2016).

Low nitrate concentrations were associated with low uptakes rates (**IV**), estimated by bottle incubations using the N-15 isotope. The incubation results agree qualitatively with the expectation that strong stratification reduces nutrient supply. However, the uptake of nitrate (into the pool of particulate organic nitrogen) was more than one order of magnitude smaller than the nitrate flux supplied. We put forward several possible explanations in paper **IV**, but the one I in hindsight consider most plausible is that after the spring bloom, most (on the order of 90%) of the new production contributed to the build-up of the large pool of dissolved organic nitrogen that was observed in August (Lena Seuthe, pers. comm. 2016). Such a large shunt of nitrogen into the microbial loop would indicate that most new production that occurs during the summer months would not be exported, but instead respired later. This might however not have huge implications for the annually integrated export since $F_{\mathcal{N}}$ was small compared to the annual nitrate drawdown.

In this context it is worth stressing that the seasonal NCP (the maximum of which can be estimated e.g. from the end-of-season nutrient drawdown, see e.g. CODISPOTI et al., 2013) is not necessarily the same as the export

---

[1] In fact, many regions of the world ocean exhibit similar, if not lower, ratios between nitrate and density gradients across the nitracline, see e.g. σ_θ-$\mathcal{N}$ plots by OMAND and MAHADEVAN (2015); cf. the methodology employed in **I**.

production (EP). The discrepancy is then accounted for by (e.g., dissolved) organic matter that is not exported, but instead remineralized in the upper ocean during the following winter. Ideally, this wintertime respiration should be included in estimates of annual NCP, but observations are few and far between (e.g., TREMBLAY et al. (2008) speculated that the $\mathcal{N}$ increase they observed during winter was due to nitrification).

Similarly, NPP is usually larger than NCP due to reliance on regenerated nutrients throughout the summer. Importantly, in the framework of Arctic carbon cycling, the instrumental definition of new production (NP) as equal to NCP would often preclude a meaningful discussion of the associated export. It is therefore more precise to define NP=EP, and acknowledge that the NCP based on nutrient profiles measured in late summer is only an upper bound for EP. A linear extrapolation from trends or patterns in EP to NPP or even NCP is not advisable as community respiration is governed by many additional factors. Both the NPP:EP and NPP:NCP ratios are subject to the complicated interplay between nutrient loading, turbulence intensity, temperature, salinity, mortality, grazing, and heterotrophic respiration, that sets the community structure of marine ecosystems.

4.2 THE FUTURE OF ARCTIC MARINE PRIMARY PRODUCTION

The work presented in this thesis demonstrates a clear need to distinguish between annual NCP on one side and (summertime) daily NCP and NPP on the other side. As the open-water period lengthens, it has been observed that NPP increases (ARRIGO and VAN DIJKEN, 2015), but the implications for EP are not immediately clear. Similarly, enhanced daily NCP during the summer might not necessarily be a significant fraction of annual NCP (**IV**). Predictions of Arctic marine primary production therefore have to be carefully defined both with respect to their temporal scope and the involved nutrient pools.

This thesis also indicates that the potential for increased new production is very limited. The recent Arctic-wide increases in primary production noted above are therefore likely attributable to enhanced recycling of nutrients. The fall blooms recently observed by ARDYNA et al. (2014), however, might well be due to entrainment of new nutrients as stratification deepens when the ice cover is gone (**III**).

While climate related changes in the strength of stratification alone have the potential to drive marked changes in regional $\mathsf{F}_{\mathcal{N}}$ (**I**), a major uncertainty is the future of the internal wave field in the Arctic Ocean. Recent findings suggest that the absence of sea ice enables near-inertial energy input (RAINVILLE and WOODGATE, 2009; DOSSER and RAINVILLE, 2016), but other observations suggest that most of this energy is dissipated in the strongly stratified surface (LINCOLN et al., 2016). The hydrographical contrasts across the Arctic Ocean and seasonal stratification likely also affect the input and redistribution of near-inertial energy. In the relatively weakly stratified Eurasian Basin, the near-inertial energy might penetrate deeper, but uncertainties arise from the unknown future of the shallow meltwater layers that cover much of the seasonal ice zone in summer.

4.3 OUTLOOK

The vast and shallow Arctic shelves are a large uncertainty in the projections of future Arctic marine ecosystems and nutrient cycling. This is partially because they are relatively unexplored, but not the least due to their complicated biogeochemistry dominated by extreme amounts of riverine freshwater and terrestrial carbon (e.g. SEMILETOV et al., 2012). An interesting question is whether vertical nitrate fluxes can provide a suitable framework for assessing new production also on the shallow shelves. One condition would be crucial: That the consumption of nitrate is restricted to an “upper” layer situated above a “lower” nutrient-rich pool throughout summer, i.e. that both mixing depth and euphotic zone are restricted to a distinct surface layer. This is not a given since the shallow topography could potentially make the entire water column available to mixing and light input.

As we demonstrated in paper **III**, it is primarily the sea ice melt that sets the structure of meltwater layers. These in turn affect both wind driven mixing and potentially deeper mixing due to downward radiation of near-inertial energy, and thus nutrient supply to the photic zone. Strong upper-ocean stratification sets the strength of the coupling between a variety of surface-dependent processes and the winter mixed layer on a seasonal basis, which itself is coupled to the ocean underneath via a perennial pycnocline on interannual time scales. However, future sea ice melt rates (in units of sea ice volume per area per time) have received relatively little attention as opposed to trends in sea ice extent and concentration. As the seasonal ice zone expands, I anticipate that melt rates and surface freshwater layers become increasingly important in predicting future Arctic Ocean climate.

THANKS

… go first and foremost to my supervisors Arild, Marit, Ilker and Odd Erik. Arild and Marit, you struck a wonderful balance between giving me the liberty to pursue my interests and reining me in when I was threatening to wander off. Thank you, Ilker, for a pleasant and productive (if rainy) stay in Bergen in 2015, and for pushing me just a tiny bit further whenever I was starting to be satisfied with some result. Arild, thanks for the trust you put in me when you let me take your precious instruments to just about anywhere — I'll claim it was luck I managed to bring back home as much as I did, and blame the rest on fate. I also wish to thank my other two co-authors Jean-Éric Tremblay and John D. Guthrie for joining me in my efforts. Philipp Assmy has on many occasions helped me with my dabblings in biology, both as an external evaluator and through inspiring discussions.

Vladimir Ivanov, Igor Polyakov and Andrey Pnyushkov showed me great hospitality during my stay at the International Arctic Research Center at the University of Alaska Fairbanks. Thanks also to Mikael Sejr for giving me the opportunity to join the MarineBasis program in Daneborg — it did not end up being part of my thesis, but the experience taught me a lot.

Many other people have contributed to this thesis in one way or another: My fellow Carbonbridge PhD students Maria and Marina — your long-time companionship has made all the cruises, workshops and conferences so much more enjoyable! My office mates Ingrid and Coralie — thanks for bearing with my stupid questions about biology and other things. The HavCryo section at NPI has been a stimulating scientific home ever since I first moved to Tromsø and started doing polar oceanography. Many of the participants on all the cruises I've been on have made the countless weeks and months at sea and in the ice much more bearable. Thanks go also to the crews and skippers of R/Vs Helmer Hanssen, Lance and Polarstern as well as the technicians — your patience with all my special requests is greatly appreciated. Marius, your enthusiasm for fixing stuff is wonderful.

Last but not least, thanks to all the friends, here and in the rest of the world, who have made Tromsø such a nice place to live in, travel from and return to. My family down south — thanks for all the support, and apologies for living such a long way from home.

My position was financed through the Norwegian Research Council project "Carbonbridge: Bridging marine productivity regimes: How Atlantic advection affects productivity, carbon cycling and export in a melting Arctic Ocean".

BIBLIOGRAPHY

Abbott, M. R. (1993), *Patch Dynamics*, chap. Phytoplankton Patchiness: Ecological Implications and Observation Methods, pp. 37–49, Springer.

Anderson, L. G., E. P. Jones, and J. H. Swift (2003), Export production in the central Arctic Ocean evaluated from phosphate deficits, *Journal of Geophysical Research*, *108*(C6), doi:10.1029/2001jc001057.

Ardyna, M., M. Babin, M. Gosselin, E. Devred, L. Rainville, and J.-E. Tremblay (2014), Recent Arctic Ocean sea ice loss triggers novel fall phytoplankton blooms, *Geophysical Research Letters*, *41*(17), 62076212, doi:10.1002/2014gl061047.

Arrigo, K. R., and G. L. van Dijken (2015), Continued increases in Arctic Ocean primary production, *Progress in Oceanography*, *136*, 60–70, doi:10.1016/j.pocean.2015.05.002, Synthesis of Arctic Research (SOAR).

Behrenfeld, M. J., and E. S. Boss (2014), Resurrecting the ecological underpinnings of ocean plankton blooms, *Annu. Rev. Marine. Sci.*, *6*(1), 167194, doi:10.1146/annurev-marine-052913-021325.

Bourgault, D., C. Hamel, F. Cyr, J.-E. Tremblay, P. S. Galbraith, D. Dumont, and Y. Gratton (2011), Turbulent nitrate fluxes in the Amundsen Gulf during ice-covered conditions, *Geophysical Research Letters*, *38*(15), doi:10.1029/2011GL047936.

Christian, J. R., M. R. Lewis, and D. M. Karl (1997), Vertical fluxes of carbon, nitrogen, and phosphorus in the North Pacific Subtropical Gyre near Hawaii, *Journal of Geophysical Research: Oceans*, *102*(C7), 15,667–15,677, doi:10.1029/97JC00369.

Codispoti, L., V. Kelly, A. Thessen, P. Matrai, S. Suttles, V. Hill, M. Steele, and B. Light (2013), Synthesis of primary production in the Arctic Ocean: III. Nitrate and phosphate based estimates of net community production, *Progress in Oceanography*, *110*, 126–150, doi:10.1016/j.pocean.2012.11.006.

Dickson, R., B. Rudels, S. Dye, M. Karcher, J. Meincke, and I. Yashayaev (2007), Current estimates of freshwater flux through Arctic and subarctic seas, *Progress in Oceanography*, *73*(3–4), 210–230, doi:10.1016/j.pocean.2006.12.003.

Dosser, H. V., and L. Rainville (2016), Dynamics of the changing near-inertial internal wave field in the Arctic Ocean, *Journal of Physical Oceanography*, *46*(2), 395415, doi:10.1175/jpo-d-15-0056.1.

Dugdale, R. C., and J. J. Goering (1967), Uptake of new and regenerated forms of nitrogen in primary productivity, *Limnology and Oceanography*, *12*(2), 196–206, doi:10.4319/lo.1967.12.2.0196.

Eppley, R., and B. Peterson (1979), The flux of particulate organic matter to the deep ocean and its relation to planktonic new production, *Nature*, *282*, 677–680.

Fer, I. (2006), Scaling turbulent dissipation in an Arctic fjord, *Deep Sea Research Part II: Topical Studies in Oceanography*, *53*, 77 – 95, doi:10.1016/j.dsr2.2006.01.003, IAPSO/SCOR Conference on Ocean Mixing.

Frigstad, H., T. Andersen, R. G. Bellerby, A. Silyakova, and D. O. Hessen (2014), Variation in the seston C:N ratio of the Arctic Ocean and pan-Arctic shelves, *Journal of Marine Systems*, *129*, 214–223, doi:10.1016/j.jmarsys.2013.06.004.

Honjo, S., S. J. Manganini, R. A. Krishfield, and R. Francois (2008), Particulate organic carbon fluxes to the ocean interior and factors controlling the biological pump: A synthesis of global sediment trap programs since 1983, *Progress in Oceanography*, *76*(3), 217285, doi:10.1016/j.pocean.2007.11.003.

Huisman, J., P. van Oostveen, and F. J. Weissing (1999), Critical depth and critical turbulence: Two different mechanisms for the development of phytoplankton blooms, *Limnology and Oceanography*, *44*(7), 1781–1787, doi:10.4319/lo.1999.44.7.1781.

Johnson, K. S., and L. J. Coletti (2002), In situ ultraviolet spectrophotometry for high resolution and long-term monitoring of nitrate, bromide and bisulfide in the ocean, *Deep Sea Research Part I: Oceanographic Research Papers*, *49*(7), 1291–1305, doi:10.1016/s0967-0637(02)00020-1.

Lewis, M. R., D. Hebert, W. G. Harrison, T. Platt, and N. S. Oakey (1986), Vertical nitrate fluxes in the oligotrophic ocean, *Science*, *234*(4778), 870873, doi:10.1126/science.234.4778.870.

Li, W. K. W., F. A. McLaughlin, C. Lovejoy, and E. C. Carmack (2009), Smallest algae thrive as the Arctic Ocean freshens, *Science*, *326*(5952), 539539, doi:10.1126/science.1179798.

Lincoln, B. J., T. P. Rippeth, Y.-D. Lenn, M. L. Timmermans, W. J. Williams, and S. Bacon (2016), Wind-driven mixing at intermediate depths in an ice-free Arctic Ocean, *Geophysical Research Letters*, *43*(18), 9749–9756, doi:10.1002/2016GL070454, 2016GL070454.

Loeng, H. (1991), Features of the physical oceanographic conditions of the Barents Sea, *Polar Research*, *10*(1), 5–18, doi:10.1111/j.1751-8369.1991.tb00630.x.

Mackas, D. L., K. L. Denman, and M. R. Abbott (1985), Plankton patchiness: biology in the physical vernacular, *Bulletin of Marine Science*, *37*(2), 652–674.

Margalef, R. (1978), Life-forms of phytoplankton as survival alternatives in an unstable environment, *Oceanologica acta*, *1*(4), 493–509.

Omand, M. M., and A. Mahadevan (2015), The shape of the oceanic nitracline, *Biogeosciences*, *12*(11), 3273–3287, doi:10.5194/bg-12-3273-2015.

Osborn, T. R. (1980), Estimates of the local rate of vertical diffusion from dissipation measurements, *J. Phys. Oceanogr.*, *10*(1), 83–89, doi:10.1175/1520-0485(1980)010⟨0083:EOTLRO⟩2.0.CO;2.

Perrette, M., A. Yool, G. D. Quartly, and E. E. Popova (2011), Near-ubiquity of ice-edge blooms in the Arctic, *Biogeosciences*, *8*(2), 515–524, doi:10.5194/bg-8-515-2011.

Peter, K. H., and U. Sommer (2013), Phytoplankton cell size reduction in response to warming mediated by nutrient limitation, *PLoS ONE*, *8*(9), e71,528, doi:10.1371/journal.pone.0071528.

Polyakov, I. V., A. V. Pnyushkov, R. Rember, L. Padman, E. C. Carmack, and J. M. Jackson (2013), Winter convection transports Atlantic water heat to the surface layer in the eastern Arctic Ocean, *Journal of Physical Oceanography*, *43*(10), 2142–2155, doi:10.1175/jpo-d-12-0169.1.

Popova, E. E., A. Yool, A. C. Coward, F. Dupont, C. Deal, S. Elliott, E. Hunke, M. Jin, M. Steele, and J. Zhang (2012), What controls primary production in the Arctic Ocean? Results from an intercomparison of five general circulation models with biogeochemistry, *Journal of Geophysical Research*, *117*, doi:10.1029/2011jc007112.

Rainville, L., and R. A. Woodgate (2009), Observations of internal wave generation in the seasonally ice-free Arctic, *Geophysical Research Letters*, *36*(23), doi:10.1029/2009GL041291, l23604.

Redfield, A. C., B. H. Ketchum, and F. A. Richards (1963), The influence of organisms on the composition of sea-water, in *The Sea*, edited by M. Hill, pp. 26–77, Academic Press.

Rudels, B., E. P. Jones, U. Schauer, and P. Eriksson (2004), Atlantic sources of the arctic ocean surface and halocline waters, *Polar Research*, *23*(2), 181–208, doi:10.1111/j.1751-8369.2004.tb00007.x.

Rudels, B., M. Korhonen, U. Schauer, S. Pisarev, B. Rabe, and A. Wisotzki (2015), Circulation and transformation of Atlantic water in the Eurasian Basin and the contribution of the Fram Strait inflow branch to the Arctic Ocean heat budget, *Progress in Oceanography*, *132*, 128–152, doi:10.1016/j.pocean.2014.04.003.

Sakamoto, C. M., K. S. Johnson, and L. J. Coletti (2009), Improved algorithm for the computation of nitrate concentrations in seawater using an in situ ultraviolet spectrophotometer, *Limnology and Oceanography: Methods*, *7*, 132–143.

Salehipour, H., W. R. Peltier, C. B. Whalen, and J. A. MacKinnon (2016), A new characterization of the turbulent diapycnal diffusivities of mass and momentum in the ocean, *Geophysical Research Letters*, *43*(7), 3370–3379, doi:10.1002/2016gl068184.

Semiletov, I. P., N. E. Shakhova, V. I. Sergienko, I. I. Pipko, and O. V. Dudarev (2012), On carbon transport and fate in the East Siberian Arctic land–shelf–atmosphere system, *Environmental Research Letters*, *7*(1), 015,201.

Slagstad, D., P. F. J. Wassmann, and I. Ellingsen (2015), Physical constrains and productivity in the future arctic ocean, *Frontiers in Marine Science*, *2*, doi:10.3389/fmars.2015.00085.

Sommer, U., K. H. Peter, S. Genitsaris, and M. Moustaka-Gouni (2016), Do marine phytoplankton follow Bergmanns rule sensu lato?, *Biological Reviews*, doi:10.1111/brv.12266.

Sterner, R. W., T. Andersen, J. J. Elser, D. O. Hessen, J. M. Hood, E. McCauley, and J. Urabe (2008), Scale-dependent carbon:nitrogen:phosphorus seston stoichiometry in marine and freshwaters, *Limnology and Oceanography*, *53*(3), 1169–1180, doi:10.4319/lo.2008.53.3.1169.

Sverdrup, H. (1953), On conditions for the vernal blooming of phytoplankton, *ICES Journal of Marine Science*, *18*(3), 287–295.

Tamelander, T., M. Reigstad, K. Olli, D. Slagstad, and P. Wassmann (2013), New production regulates export stoichiometry in the ocean, *PLoS ONE*, *8*(1), e54,027, doi:10.1371/journal.pone.0054027.

Tremblay, J.-E., and J. Gagnon (2009), *Influence of Climate Change on the Changing Arctic and Sub-Arctic Conditions*, chap. The effects of irradiance and nutrient supply on the productivity of Arctic waters: A perspective on climate change, pp. 73–89, Springer.

Tremblay, J.-E., K. Simpson, J. Martin, L. Miller, Y. Gratton, D. Barber, and N. M. Price (2008), Vertical stability and the annual dynamics of nutrients and chlorophyll fluorescence in the coastal, southeast Beaufort Sea, *Journal of Geophysical Research*, *113*(C7), doi:10.1029/2007jc004547.

Tremblay, J.-E., L. G. Anderson, P. Matrai, P. Coupel, S. Bélanger, C. Michel, and M. Reigstad (2015), Global and regional drivers of nutrient supply, primary production and CO2 drawdown in the changing Arctic Ocean, *Progress in Oceanography*, *139*, 171–196, doi:10.1016/j.pocean.2015.08.009.

Valiela, I. (2015), *Marine ecological processes*, 3rd ed., Springer-Verlag New York.

Vancoppenolle, M., L. Bopp, G. Madec, J. Dunne, T. Ilyina, P. R. Halloran, and N. Steiner (2013), Future Arctic Ocean primary productivity from CMIP5 simulations: Uncertain outcome, but consistent mechanisms, *Global Biogeochemical Cycles*, *27*(3), 605–619, doi:10.1002/gbc.20055.

Woodgate, R. (2013), Arctic ocean circulation: Going around at the top of the world, *Nature Education Knowledge*, *4*(8), 8.

Yamazaki, H., and T. Osborn (1990), Dissipation estimates for stratified turbulence, *Journal of Geophysical Research: Oceans*, *95*(C6), 9739–9744, doi:10.1029/JC095iC06p09739.

I

Randelhoff, A. and J. D. Guthrie (2016), Regional patterns in current and future export production in the central Arctic Ocean quantified from nitrate fluxes, *Geophysical Research Letters*, *43*, 8600–8608, doi:10.1002/2016gl070252.

AGU PUBLICATIONS

Geophysical Research Letters

RESEARCH LETTER

10.1002/2016GL070252

Key Points:

- Vertical nitrate flux contributes significantly to current CAO export production
- Regional differences in turbulent mixing and stratification lead to varying responses of primary production to climate change across the CAO
- Future increases in Atlantic sector EP possibly offset by reduced nitrate fluxes in other CAO regions

Correspondence to:
A. Randelhoff,
achim@npolar.no

Citation:
Randelhoff, A., and J. D. Guthrie (2016), Regional patterns in current and future export production in the central Arctic Ocean quantified from nitrate fluxes, *Geophys. Res. Lett.*, *43*, 8600–8608, doi:10.1002/2016GL070252.

Received 30 JUN 2016
Accepted 3 AUG 2016
Accepted article online 5 AUG 2016
Published online 24 AUG 2016

Regional patterns in current and future export production in the central Arctic Ocean quantified from nitrate fluxes

Achim Randelhoff[1,2] and John D. Guthrie[3]

[1]Institute for Arctic and Marine Biology, University of Tromsø, Tromsø, Norway, [2]Norwegian Polar Institute, Tromsø, Norway, [3]Polar Science Center, Applied Physics Lab, University of Washington, Seattle, Washington, USA

Abstract Due to severe nutrient and light limitation, the central Arctic Ocean has been characterized as a region of low primary productivity, with high retention of carbon in the surface waters. Using an in-depth analysis of published and new measurements of turbulent microstructure and high-resolution profiles of nitrate concentration, we reassess the vertical supply of nitrate to the Polar Mixed Layer and the associated export of particulate organic matter across the nitracline. We estimate annual export production to be approximately 1.5–3 g C m^{-2}, but regional differences in both current and future potential of export production are large, with the eastern Arctic being least constrained by vertical nutrient supply and the western Arctic the most. Future changes in export production are assessed using a 1-D budget model; increases in the Atlantic sector are possibly compensated by decreases in the rest of the central Arctic Ocean such that the net change might be insignificant.

1. Introduction

The central Arctic Ocean (CAO) is strongly stratified in the surface, which limits nutrient supply to the photic zone and constrains Arctic Ocean primary production [e.g., *Tremblay et al.*, 2015]. Various halocline structures are present throughout the CAO, but a common feature is their perennial persistence as opposed to on the shelves, where relatively strong mixing can homogenize vertical stratification during the winter [e.g., *Aagaard and Carmack*, 1994; *Randelhoff et al.*, 2015]. The halocline separates the Polar Mixed Layer (PML), where primary production takes place, from Atlantic (AW) or Pacific Water (PW) at intermediate depths. Due to the dependence of primary production on sunlight, upper ocean nutrient concentrations vary strongly with season, and a part of its nitrogen pool is exported across the pycnocline as biogenic particulate organic nitrogen.

PW and AW are the main sources of nutrients in the Arctic Ocean [*Torres-Valdés et al.*, 2013], driving the replenishment of the PML nutrient inventory from below, thus ensuring a steady seasonal cycle of nutrient concentrations in the surface waters.

Previous findings indicate fairly low productivity in the deep basins of the Arctic Ocean, between 10 and several tens of g C m^{-2} yr^{-1} based on various methods like oxygen concentration [*Pomeroy*, 1997; *Zheng et al.*, 1997], incubations [*Cota et al.*, 1996; *Gosselin et al.*, 1997] and annual drawdown of nutrients [*Codispoti et al.*, 2013]. The export flux has been estimated to be even lower at less than 1 g C m^{-2} yr^{-1} [*Anderson et al.*, 2003; *Cai et al.*, 2010; *Honjo et al.*, 2010], and *Olli et al.* [2007] attributed low export estimates to high grazing pressure of zooplankton expatriates advected from the shelves. Thus, the picture of CAO nutrient cycling that has emerged is one of low export efficiency driven by intense recycling of organic matter in the shallow photic zone, with very little potential for carbon sequestration [*Wassmann et al.*, 2004]. However, in studies of CAO productivity and nutrient cycling, the role of vertical mixing is usually treated only qualitatively, where the strong stratification is invoked to infer weak vertical fluxes without further differentiation.

Measuring the turbulent vertical flux of nitrate across the perennial nitracline of the Arctic Ocean takes advantage of two features: Its persistence ensures little seasonality in the flux magnitude compared to the seasonal nitracline that may appear in the summer months in the Eastern Arctic, and second, it is sufficiently removed from the ocean surface such that turbulent mixing intensities are not dictated by intermittent atmospheric, shear-driven mixing. To balance the budget, the upward vertical flux of nitrate (NO_3^-) is an estimate of the downward vertical flux of particulate organic nitrogen minus what is supplied by horizontal advection. Due to large residence times, the horizontal ventilation of the CAO surface waters contributes only a small amount

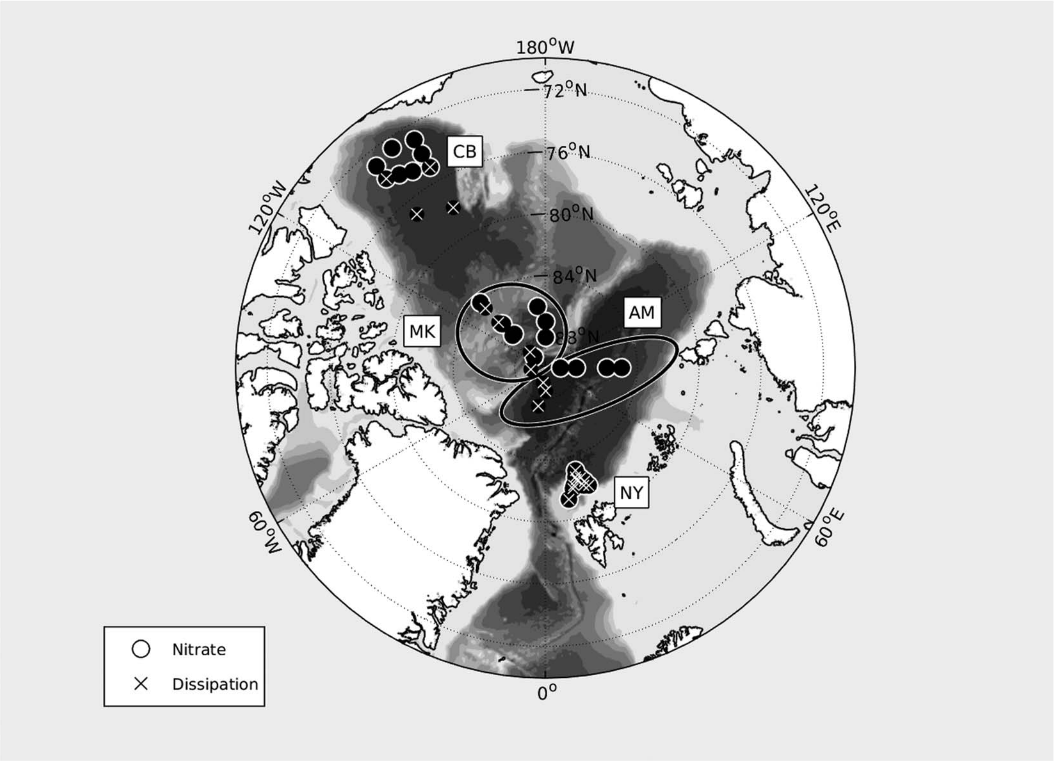

Figure 1. Map of sample locations, indicating the four regions: Nansen Basin/Yermak Plateau (NY), Amundsen Basin (AM), Makarov Basin (MK), and Canada Basin (CB).

of nutrients to the PML, amounting to approximately 0.5 g C m^{-2} yr^{-1} [*Anderson et al.*, 2003]. Therefore, the vertical supply of nitrate also places a bound on NO_3^--based production in the PML.

In this study, we set out to quantify regional patterns in the current export production that is supported by the vertical (and horizontal) resupply of nitrate and assess what future export production might be like given climate-related trends in the freshwater budget, sea ice cover, and turbulent mixing.

2. Methods

2.1. Data

This study combines new observations in the Nansen Basin/Yermak Plateau region with a reanalysis of similar, previously published data from other parts of the CAO.

Colocated continuous vertical profiles of (sensor-based) nitrate concentrations ($\mathcal{N}$) and turbulent microstructure were collected during the January–June 2015 N-ICE ice camp in the Nansen Basin and in the vicinity of the Yermak Plateau north of Svalbard (Figure 1; see *Granskog et al.* [2016] for details). All of the N-ICE profiles included in this study were located at water depths >1500 m.

Vertical profiles of conductivity, temperature, and depth (CTD) and nitrate concentration data in the Amundsen, Makarov, and Canada Basins obtained through the North Pole Environmental Observatory (NPEO) in 2007 and 2008 [*Alkire et al.*, 2010] have been downloaded from https://arcticdata.io/catalog/#view/doi:10.18739/A2HK6Z and https://arcticdata.io/catalog/#view/doi:10.18739/A2WS4P.

Microstructure profiles collected in the Amundsen Basin close to the North Pole (provided by Ilker Fer) were analyzed for dissipation in the nitracline. These microstructure measurements are published and described in more detail by *Fer* [2009], *Sirevaag and Fer* [2012], and *Guthrie et al.* [2013].

The Makarov Basin dissipation estimate is derived from a subset of eXpendable current profiler (XCP) and CTD profiles collected as part of NPEO in 2007. The Canada Basin dissipation estimate is derived from 3 years of current meter data from four moorings deployed as part of the Beaufort Gyre Exploration Project (BGEP).

We group the data into four geographical regions: NY (Nansen Basin/Yermak Plateau), AM (Amundsen Basin), MK (Makarov Basin), and CB (Canada Basin) (see Figure 1). The distinction drawn here between the hydrografies of the Makarov and Amundsen Basins might change on decadal timescales, depending on the atmospheric forcing of freshwater budgets and the Transpolar Drift [e.g., *Morison et al.*, 2012], but for the 2007/2008 NPEO data, the location of the Lomonosov Ridge is a natural separation between the two regimes.

2.2. Dissipation Estimates

Microstructure data, collected using a MSS90-L profiler (IWS Wassermesstechnik, Germany), were processed following *Fer* [2006]. Assuming local small-scale isotropy [*Yamazaki and Osborn*, 1990], dissipation of turbulent kinetic energy was estimated from the measured microscale shear as $\epsilon = 7.5\nu\langle(\partial_z u')^2\rangle$, where ν is the molecular viscosity of sea water and $\partial_z u'$ the turbulent shear. The processing is similar across all the microstructure data sets used in this study.

The dissipation estimates for the Makarov and Canada Basins are derived from a widely validated fine-scale parameterization based on 10 m shear variance relative to Garrett-Munk values [*Garrett and Munk*, 1975]. For full details of the parameterization, see *Kunze et al.* [2006]. The processing and analysis is described in more detail by *Guthrie et al.* [2013]. The calculation of the BGEP dissipation values is described fully by *Lique et al.* [2014]. *Guthrie et al.* [2013] showed excellent agreement between dissipation estimates derived from MSS microstructure observations and this finescale parameterization.

2.3. CTD and Nitrate Concentration Data

Processing of nitrate concentration profiles, measured using an ISUS sonde (Satlantic; V3 during N-ICE and V2 for the NPEO data), made use of the "temperature compensated, salinity subtracted" algorithm of *Sakamoto et al.* [2009], using a waveband of 217–240 nm. Although final nitrate concentrations measured by the ISUS can have uncertainties of up to 1 μM, this is mostly due to a depth-independent bias, such that vertical gradients are resolved accurately [*Randelhoff et al.*, 2016]. The bias was taken care of by calibrating output against bottle samples on all campaigns. Further details of the processing of ISUS data are described, e.g., by *Alkire et al.* [2010] and *Randelhoff et al.* [2016].

2.4. Nitrate Fluxes

In order to calculate the nitrate flux $F_\mathcal{N} = -K_\rho \frac{\partial \mathcal{N}}{\partial z}$ across the perennial nitracline, we need to combine profiles of turbulent mixing (vertical eddy diffusivity K_ρ) and nitrate concentrations ($\mathcal{N}$). This requires special care since both $K_\rho = 0.2\frac{\epsilon}{N^2}$ [*Osborn*, 1980], (ϵ being the dissipation) and $\mathcal{N}$ gradients depend on the vertical density stratification (buoyancy frequency $N^2 = -\frac{g}{\rho}\frac{\partial \rho}{\partial z}$), which can be different at different times and locations. The above definition of $F_\mathcal{N}$ is equivalent to

$$F_\mathcal{N} = 0.2\epsilon \frac{\rho}{g}\frac{\partial \mathcal{N}}{\partial \sigma_\theta}, \tag{1}$$

where we first inserted the K_ρ estimation formula and then the definition of N^2. This representation is more convenient for two reasons: First, we can ignore changes in isopycnal heights between profiles. Second, it more accurately reflects the gradients between the different water mass end-members. Otherwise, if we used K_ρ instead, we would have to adjust it for the actual buoyancy frequency in every nitrate profile.

Close to the inflow of Atlantic Water (Nansen Basin/Yermak Plateau), the $\frac{\partial \mathcal{N}}{\partial \sigma_\theta}$ slope is depth independent for each profile, while the additional end-members (PML, upper and lower halocline waters and AW) lead to variable slopes in the Canada and Makarov Basins (Figure 2a). The following criteria captured the regional patterns in nitracline distribution: For the Nansen/Yermak and Amundsen Basin, $\frac{\partial \mathcal{N}}{\partial \sigma_\theta}$ was calculated across the interval 50 to 90 m. For the Makarov Basin, $\frac{\partial \mathcal{N}}{\partial \sigma_\theta}$ was calculated over the interval from salinity $S=32$ down to either 80 m depth or $S=32.5$, whichever was deeper. For the Canada Basin, the slope was calculated over the σ_θ range from 25 to 26 kg m^{-3}. All individual regressions were checked visually.

To convert $F_\mathcal{N}$ to equivalent units of g C m^{-2} yr^{-1}, we employ a constant C:N Redfield ratio of 106:16. Any errors made by this assumption are linear and thus easily controlled.

2.5. A Simple 1-D Model for the Polar Mixed Layer Nitrate Budget

We can take advantage of the perennial nitrate gradient merely as a diagnostic tool to estimate year-round nitrate fluxes (and indirectly, export production), not attributing any role of the turbulent mixing in forcing or limiting upper ocean primary productivity. Concretely, if the productivity was increased or the vertical diffusivity decreased, the nitrate gradient would steepen in order to make $F_\mathcal{N}$ match the surface drawdown.

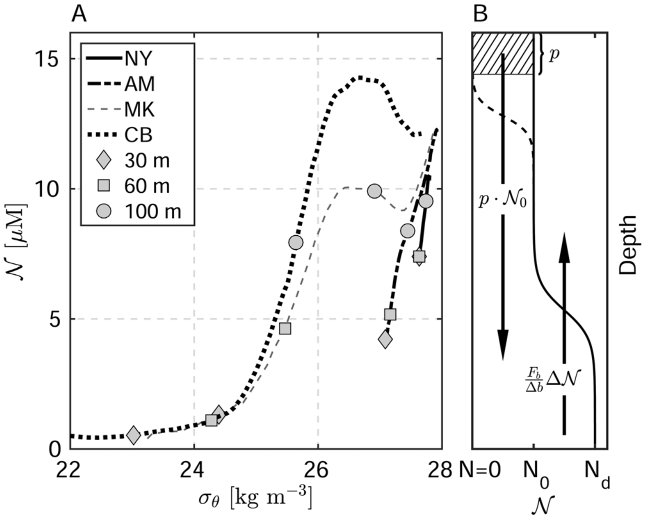

Figure 2. Vertical stratification of density and nitrate in the CAO. (a) $\mathcal{N}$-σ_θ profiles averaged by region (see Figure 1). Diamonds, squares, and circles indicate different depths. (b) Conceptual model of vertical $\mathcal{N}$ profiles with associated vertical nitrogen fluxes (see text). The seasonal nitracline (dashed line) is decoupled from the perennial nitracline. A layer of thickness p [year] (hatched area) corresponds to that fraction $p \cdot \mathcal{N}_0$ of the seasonal nitrate drawdown that is exported below the perennial nitracline, while the rest might be remineralized before reaching deep enough. Across the perennial nitracline, the vertical nitrate flux is $F_\mathcal{N} = \frac{F_b}{\Delta b}\Delta\mathcal{N} \equiv \frac{F_b}{\Delta b}(\mathcal{N}_d - \mathcal{N}_0)$.

However, since this also leads to a lower surface $\mathcal{N}$ and accordingly annual nitrate drawdown is decreased, the result is best described as the steady state of a system of coupled equations. In fact, the decomposition of $F_\mathcal{N}$ into the product of ϵ and $\frac{\partial\mathcal{N}}{\partial\sigma_\theta}$ provides a different perspective by condensing the vertical gradients into one quantity $\frac{\partial\mathcal{N}}{\partial\sigma_\theta}$ only related to $\mathcal{N}$ and σ_θ in the end-members that mix across the nitracline.

Assuming annual new production is proportional to the prebloom surface nitrate pool, export production (EP) can be described as EP $= p \cdot \mathcal{N}_0$ with the surface nitrate concentration $\mathcal{N}_0$ and a hypothetical "nitrate drawdown velocity scale" p. The parameter p is at most equal to but likely smaller than the depth of seasonal nitrate depletion (divided by [1 year]), which depends on photic zone depth, seasonal surface layer stratification, and possibly community structure; this is because we can expect that some of the consumed nitrogen is remineralized before reaching below the perennial nitracline (Figure 2b). The export production has to match the sum of the upward turbulent diffusive flux and other terms (like horizontal advection of nitrate and convective entrainment during winter); the sum of the latter is denoted by A in the following. Rewriting $\frac{\partial\mathcal{N}}{\partial\sigma_\theta}$ from equation (1) as a straight mixing line between the end-members above and below the nitracline (Figure 2a), the vertical flux becomes $F_\mathcal{N} = 0.2\epsilon\frac{\rho}{g}\frac{\mathcal{N}_d - \mathcal{N}_0}{\rho_d - \rho_0}$, where indices d and 0 refer to deep (below nitracline) and above nitracline end-members, respectively. Equating EP and $F_\mathcal{N} + A$ yields

$$\mathrm{EP} = p\frac{\frac{F_b}{\Delta b}\mathcal{N}_d + A}{p + \frac{F_b}{\Delta b}}, \tag{2}$$

where $F_b = 0.2\epsilon$ is the buoyancy flux and $\Delta b = g\frac{\rho_d - \rho_0}{\rho}$ the buoyancy difference between above and below nitracline. The ratio of the two yields a mass flux velocity scale representing the integrated effect of turbulent mixing and perennial stratification. The "drawdown velocity scale" p integrates mainly the effects of photic zone depth and seasonal stratification. Equation (2) shows that at large values of either $\frac{F_b}{\Delta b}$ or p, the other becomes limiting. For example, for high p, that is, when light is not limiting and seasonal mixing makes all nitrate in the PML accessible to primary producers, the maximum nitrate flux is

$$F_{\mathcal{N},\max} = \frac{F_b}{\Delta b}\mathcal{N}_d. \tag{3}$$

For each region, p and $\frac{F_b}{\Delta b}$ are estimated using average values of surface $\mathcal{N}_0$ and buoyancy difference Δb across the nitracline derived from each profile in that region (see Table 1, cf. also Figure 2). The parameter

Table 1. Mean Values of Key Parameters Grouped by Region (See Figure 1)[a]

Region	$F_{\mathcal{N}}$ (g C m^{-2} yr^{-1})	$\frac{\partial \mathcal{N}}{\partial \sigma_\theta}$ (mmol kg^{-1})	ϵ (W kg^{-1})	p (m yr^{-1})	$F_b/\Delta b$ (m yr^{-1})	$F_{\mathcal{N},\max}$ (g C m^{-2} yr^{-1})	$F_{\mathcal{N},\max(2100)}$ (g C m^{-2} yr^{-1})
NY	7.0	20 ± 5 [$n = 10$]	$6.0\ (3.5, 12) \cdot 10^{-9}$ [$n = 37$]	13	30	24	12
AM	1.8	14 ± 1 [$n = 6$]	$2.6\ (1.6, 4.2) \cdot 10^{-9}$ [$n \approx 600$]	7	4	3.2	1.6
MK	0.5	7 ± 0.3 [$n = 9$]	$1.5\ (0.9, 2.8) \cdot 10^{-9}$ [$n = 4$]	11	0.6	0.5	0.3
CB	0.4	10 ± 0.1 [$n = 8$]	$0.7\ (0.5, 1.0) \cdot 10^{-9}$[b]	21	0.5	0.4	0.4

[a] NY: Nansen Basin/Yermak Plateau, AM: Amundsen Basin, MK: Makarov Basin, CB: Canada Basin. $F_{\mathcal{N}}$: Vertical diffusive nitrate flux through the nitracline converted to equivalent carbon units (see text; for a discussion regarding convective entrainment, see section 4.1); $F_{\mathcal{N},\max}$: maximum nitrate flux currently possible; $F_{\mathcal{N},\max(2100)}$: possible value for maximum nitrate flux by 2100 in an RCP8.5 scenario (see text); mean $\frac{\partial \mathcal{N}}{\partial \sigma_\theta}$ (evaluated across the nitracline of every individual profile, $\pm$ standard deviation between profiles); ϵ: mean nitracline dissipation rate (in parentheses: 95% confidence intervals); p: nitrate drawdown velocity scale; $F_b/\Delta b$: buoyancy flux divided by buoyancy difference across nitracline (see text). In square brackets: number of profiles (n).

[b] Four moorings over 3 years (see text).

p is calculated as $p \equiv \mathrm{EP}/\mathcal{N}_0$, where we estimate EP as the sum of $F_{\mathcal{N}}$ and horizontal advection (roughly 0.5 g C m^{-2} yr^{-1}, see *Anderson et al.* [2003]). $\frac{F_b}{\Delta b}$ is based on the buoyancy difference between just above the nitracline and the level where $\mathcal{N}_d = 10$ μM. However, note that the exact choice of $\mathcal{N}_d$ is not crucial as long as it is inside the range where $\frac{\partial \mathcal{N}}{\partial \sigma_\theta}$ is constant and we evaluate Δb relative to the same depth.

3. Results

The four different regions showed considerable differences, where σ_θ-$\mathcal{N}$ slopes, dissipation rates, and accordingly $F_{\mathcal{N}}$ were largest in the east (Nansen Basin/Yermak and Amundsen Basin) and smallest in the west (Makarov and Canada Basins) (see Figure 1, Table 1). Overall, $F_{\mathcal{N}}$ ranged between 0.4 and 7 g C m^{-2} yr^{-1}. The p values are located in a relatively narrow range between 7 and 21 m yr^{-1} for all profiles, while $\frac{F_b}{\Delta b}$ varies strongly between 0.5 and 30 m yr^{-1}.

The maximum $F_{\mathcal{N},\max}$ the mixing can support (following equation (3)) is equal to present-day $F_{\mathcal{N}}$ in the Canadian Basin, only slightly larger in the Amundsen Basin (3.2 g C m^{-2} yr^{-1}) and largest in the Yermak Plateau region of the Nansen Basin (24 g C m^{-2} yr^{-1}) (Table 1). Since Amundsen Basin p would have to increase by several tens of m yr^{-1} in order to achieve this increase, we can consider the Amundsen Basin to be practically nutrient-limited, but not as strictly as the Canada and Makarov Basins. Nansen Basin/Yermak Plateau region EP, however, is not limited by nutrients.

4. Discussion

4.1. Stratification and Mixing

As expected, turbulent mixing is much stronger in the relative vicinity of the Yermak Plateau than in the otherwise extremely quiescent CAO. In addition, the low PML salinities in the western Arctic lead to smaller σ_θ-$\mathcal{N}$ slopes than in the East and thus very small $F_{\mathcal{N}}$. However, it is not primarily the stratification, but the low mixing levels that suppress vertical fluxes of nitrate in the Canadian Arctic. Since upper ocean stratification also enhances the under-ice dissipation mechanism outlined by *Morison et al.* [1985], it could be responsible for removing energy from the internal wave field such that less small-scale mixing can penetrate into the nitracline [*Guthrie et al.*, 2013]. Since the double-diffusive staircases are located much deeper (starting from around 200 m [*Timmermans et al.*, 2008]) than the nitracline, double-diffusive convection is not a mode for vertical transport of nitrate.

The "true"$F_{\mathcal{N}}$ values are probably slightly higher than the estimates presented here for two reasons: First, the NPEO data used in this study were all sampled in early spring, just before the onset of melting or primary production. Vertical nitrate gradients are therefore at their weakest, reducing the flux somewhat. However, seeing that NO_3^- inventories in the Canada and Makarov Basins are extremely low to begin with, this effect is probably not significant, and might be more important in the eastern Arctic data. Second, also the Makarov and Amundsen Basin fine/microstructure data was sampled in early spring. *Dosser and Rainville* [2016] find that internal wave amplitudes are 16% higher during the summer when low ice concentrations facilitate input of near-inertial energy, which indicates somewhat but not much higher $F_{\mathcal{N}}$ values than we calculated for this study.

In addition, (haline) winter convection can entrain a certain portion of the nitracline into the Polar Mixed Layer. Because average buoyancy fluxes (estimated as 0.2ϵ) across the pycnocline can only balance at most a few percent of the seasonal sea ice meltwater input, we can use the seasonal accumulation of meltwater as an estimate for winter convection. The findings of *McPhee et al.* [1998] and *Timmermans et al.* [2011] thus indicate a convection-derived density surplus of approximately 20 kg m^{-2}. To estimate regional patterns and the orders of magnitude of nitrate entrainment by convection, we assume that about half of this buoyancy flux goes into erasing the seasonal stratification and the other half could potentially entrain nitrate from the upper nitracline. The entrainment flux can be estimated by distributing this density surplus, keeping the mixed layer unstratified, and integrating the additional nitrate down to the convection depth. The western Arctic is strongly salinity stratified even above the nitracline (Figure 2) such that this convection cannot penetrate very deep into the nitracline. Accordingly, we estimate an additional $F_{\mathcal{N},\text{convective}} = 0.01$ and 0.05 g C m^{-2} yr^{-1} for the Canada and Makarov Basins, respectively. However, the low-$\mathcal{N}$ surface layer is unstratified in our data from the Eastern Arctic, so our method yields considerably higher estimates of $F_{\mathcal{N},\text{convective}} = 1$ and 2 g C m^{-2} yr^{-1} for the Amundsen Basin and the Nansen Basin/Yermak Plateau data, respectively, but it must be stressed that these numbers are mostly indicative of regional trends and the absolute magnitudes are likely smaller since wind mixing rarely reaches deep enough that it could help with entraining heavier water into the deep mixed layers of the Eurasian Basin.

4.2. Arctic Ocean Productivity

Weighting the individual $F_{\mathcal{N}}$ estimates by the areas of the basins they cover (the Nansen/Yermak estimate is extended across the western Nansen Basin and along the shelf slope, covering $2 \cdot 10^{11}$ m^2), the average upward nitrate flux across all four regions is 1.5 ± 0.5 g C m^{-2} yr^{-1}, where the uncertainty stems from stipulating an uncertainty of approximately 10% in the area weights. In addition, the convective entrainment of nitrate (assuming it is represented by the numbers as detailed in the previous section) provides another 0.5 g C m^{-2} yr^{-1}. Horizontal advection supplies another 0.5 g C m^{-2} yr^{-1} [*Anderson et al.*, 2003]. In total, this accumulates to an export production somewhere between 1.5 and 3 g C m^{-2} yr^{-1}.

This is significantly higher than the 0.6–1.3 g C m^{-2} yr^{-1} value that *Anderson et al.* [2003] found using phosphate deficits and residence time of the end-members constituting the PML. Although they included some estimates of the diapycnal mixing, all of these represent very weak mixing ($K_\rho = 1–7 \cdot 10^{-6}$ m^2 s^{-1}) at the lower end of observed values. The present study indicates that their analysis somewhat underestimated the importance of the vertical supply of nutrients, although the difference in terms of absolute values of export production is very small.

Cai et al. [2010] estimated the particulate organic carbon flux at 100 m depth over the Central Arctic from Thorium-234 measurements in late summer to be what is equal to 0.9 g C m^{-2} yr^{-1}, consistent with our value when excluding the high flux in the area close to the Yermak Plateau. *Honjo et al.* [2010] measured daily fluxes of particulate organic carbon at 120 and 200 m depth over the deep Beaufort Gyre ranging between what is equal to 0.05 and 0.65 g C m^{-2} yr^{-1}, but the seasonal distribution is not well resolved. These values are smaller than what we infer for the Canada Basin, but comparable considering that the Beaufort Gyre has longer residence times than the rest of the Canada Basin and therefore receives less horizontal nutrient input [*Anderson et al.*, 2003].

Anderson et al. [2003] caution against the use of nitrate as a tracer for assessing export production due to uncertainties surrounding nitrification, denitrification, and nitrogen fixation. We assume that denitrification, requiring low levels of dissolved oxygen, is not an issue when the water has left the shallow shelves. Nitrification does not disturb the nitrogen budget as it simply counts toward regenerated production [e.g., *Tremblay et al.*, 2015]. Nitrogen fixation in the Arctic Ocean is still an open question. For the Canadian Arctic, *Blais et al.* [2012] identify the Mackenzie River as a source of diazotrophs and find nitrogen fixation rates of 0.14 μmol N m^{-3} d^{-1} for the southern Beaufort Sea, which (assuming a seasonal mixed layer depth of 25 m) could contribute at most 0.1 g C m^{-2} in annual production—potentially appreciable, but negligible in the context of all the other uncertainties surrounding our estimates.

Based on nutrient-drawdown-based estimates of net community production (NCP), *Codispoti et al.* [2013] infer that production in the Eurasian Basin is not nutrient limited but rather light limited. However, their winter data are biased toward the vicinity of the Yermak Plateau where nutrient concentrations are higher, which skews NCP estimates. Our findings indicate that NCP in the Amundsen Basin is still nutrient limited and that among our study regions, only Nansen Basin NCP in the vicinity of the Yermak Plateau is not limited by nutrients at all.

Note how the drawdown velocity of around 10 to 20 m yr^{-1} coincides with the scale of the vertical extent of the seasonal meltwater-induced upper ocean stratification in the Arctic summer [see also *McPhee et al.*, 1987; *Randelhoff et al.*, 2014]. This scale is also representative of the depth of nitrate depletion early in the season before the subsurface chlorophyll maximum has consumed a large part of the nutrients below the seasonal pycnocline [*Randelhoff et al.*, 2016]. Although it therefore is an attractive idea to associate blooms with high export efficiencies, the link between primary production during phytoplankton blooms and the associated export of particulate matter remains elusive.

4.3. Future Evolution of Arctic Primary Production

By way of the 1-D mixed-layer $\mathcal{N}$ budget presented above, the implications of the predicted acceleration of the hydrological cycle, accompanying increase of freshwater storage in the surface mixed layer and trends in seasonal ice melt become easier to interpret.

Increasing summer ice melt rates will strengthen seasonal stratification and entail smaller upward nitrate fluxes through the seasonal pycnocline, but if the melt rates are high enough to melt most of the ice before the end of summer, seasonal stratification will weaken again as a result of the reduced freshwater input at the surface, leading to more nitrate assimilation [*Randelhoff et al.*, 2016]. In addition, a less dense ice cover will also permit more input of wind energy, driving nitracline dissipation. An increase in photic zone depth might lead to an increase in p. Because of uncertainties as to how much of the consumed nitrogen is actually exported under changed nutrient loading, the fate of p is unclear, but if anything, it will likely increase.

The (nutrient-poor) freshwater runoff feeding into the Arctic Ocean is predicted to increase significantly [*Bintanja and Selten*, 2014; *Haine et al.*, 2015], strengthening stratification at the base of the PML [*Nummelin et al.*, 2015]. Vertical mixing is a complicated issue with many faces. Even neglecting the speculative changes in nitracline dissipation, it is illustrative to consider the possible impacts of changing stratification alone since its response is relatively robust as the freshwater input to the Arctic increases. To this end, we extracted 21st century projections of CAO stratification from the RCP8.5 run of the Norwegian Earth System model [*Bentsen et al.*, 2013; *Iversen et al.*, 2013]. Comparing the 2005–2015 and the 2090–2100 mean density fields and grouping them into our four subregions, we find that below-PML stratification (expressed as N^2, i.e., $\sim \Delta b$) approximately doubles by the end of the century in all four subregions except for the Canada Basin where it remains unchanged. Changing $F_b/\Delta b$ accordingly and calculating the updated maximum vertical nitrate flux $F_{\mathcal{N},\text{max}(2100)}$, we find that by 2100, there is the distinct potential that the enhanced stratification alone reduces export production in most areas of the CAO (Table 1). While these numbers are only indicative of the relative trends, they suggest that possible increases of export production close to the Atlantic inflow (“NY” region) are offset by decreases in the other regions; even though the CAO-average $F_{\mathcal{N},\text{max}(2100)}$ is slightly higher than the current estimate, the difference is not significant (1.7 g C m^2 yr^{-1} versus 1.4 g C m^2 yr^{-1} before rounding within uncertainty).

5. Summary and Perspectives

In this study, we have formalized and quantified current export production in the CAO. By and large, our study confirms the common argument that CAO export production is mostly constrained by nutrient availability, and our study indicates that it will be even more so in a future, even more stratified CAO. We suggest that CAO export production is between 1.5 and 3 g C m^{-2} yr^{-1}, which is slightly more than previously assumed but still very small.

More importantly, there exist horizontal gradients along a transect crossing the deep basins of the Arctic Ocean from west to east. In the west, the strong haline stratification and low levels of mixing conspire to constrain nutrient availability. In the east, the near-surface inflow of saltier Atlantic Water leads to weak vertical stratification, which together with elevated turbulent mixing close to the Yermak Plateau and the shelf region alleviates nutrient limitation, and instead makes the seasonal stratification and light availability a limiting factor. The problem of predicting future CAO export production has thus been framed in terms of an “upward flux velocity scale" $\frac{F_b}{\Delta b}$ and a "nutrient drawdown velocity scale" p. Although climate-related changes in the density field alone are sufficient to drive markedly regional changes in nutrient supply to the photic zone, more work is needed to (a) predict the relative magnitude of changes in F_b and Δb, and (b) understand how p is related to seasonal stratification, photic zone depth, and export efficiency as a function of community structure.

Acknowledgments
A.R.'s work was supported through the project CARBON BRIDGE: Bridging marine productivity regimes: How Atlantic advective inflow affects productivity, carbon cycling, and export in a melting Arctic Ocean, a Polar Programme (project 226415) funded by the Norwegian Research Council. J.G. was funded through National Science Foundation projects ARC-0909408 and ARC-0856330. N-ICE data collection was supported by the Norwegian Polar Institute's Centre for Ice, Climate and Ecosystems (ICE) through the N-ICE project, with additional support from the Ministry of Climate and Environment, and Ministry of Foreign Affairs of Norway. We thank the captains and crews of R/V *Lance* and all the scientists involved in the N-ICE field campaign for their support. The Makarov and Amundsen Basin ISUS and the Makarov Basin XCP data were collected through the North Pole Environmental Observatory in 2007 and 2008. The Canada Basin ISUS and MMP mooring data were collected through the Beaufort Gyre Exploration Program. Both projects were funded by the National Science Foundation. Ilker Fer provided the Amundsen Basin dissipation profiles. Aleksi Nummelin assisted with extracting the NorESM model results. We thank Arild Sundfjord for helpful comments on an earlier version of this paper. Two anonymous reviewers helped greatly to clarify the presentation of the material. N-ICE data are available through the Norwegian Polar Data Centre at https://data.npolar.no/dataset/96eb41f9-c620-5fe4-a7a3-96b0e55fd3d5 (ISUS) and https://data.npolar.no/dataset/774bf6ab-b27e-51ab-bf8c-eb866cf61be2 (MSS).

References

Aagaard, K., and E. C. Carmack (1994), The Arctic Ocean and climate: A perspective, in *The Polar Oceans and Their Role in Shaping the Global Environment*, edited by O. M. Johannessen, R. D. Muench, and J. E. Overland, pp. 5–20, AGU, Washington, D. C., doi:10.1029/GM085p0005

Alkire, M. B., K. K. Falkner, J. Morison, R. W. Collier, C. K. Guay, R. A. Desiderio, I. G. Rigor, and M. McPhee (2010), Sensor-based profiles of the NO parameter in the central Arctic and southern Canada Basin: New insights regarding the cold halocline, *Deep Sea Res., Part I*, *57*(11), 1432–1443, doi:10.1016/j.dsr.2010.07.011.

Anderson, L. G., E. P. Jones, and J. H. Swift (2003), Export production in the central Arctic Ocean evaluated from phosphate deficits, *J. Geophys. Res.*, *108*(C6), 3199, doi:10.1029/2001JC001057.

Bentsen, M., et al. (2013), The Norwegian Earth system model, NorESM1-M—Part 1: Description and basic evaluation of the physical climate, *Geosci. Model Dev.*, *6*(3), 687–720, doi:10.5194/gmd-6-687-2013.

Bintanja, R., and F. M. Selten (2014), Future increases in Arctic precipitation linked to local evaporation and sea-ice retreat, *Nature*, *509*(7501), 479–482.

Blais, M., J.-E. Tremblay, A. D. Jungblut, J. Gagnon, J. Martin, M. Thaler, and C. Lovejoy (2012), Nitrogen fixation and identification of potential diazotrophs in the Canadian Arctic, *Global Biogeochem. Cycles*, *26*, GB3022, doi:10.1029/2011GB004096.

Cai, P., M. Rutgers van der Loeff, I. Stimac, E.-M. Nöthig, K. Lepore, and S. B. Moran (2010), Low export flux of particulate organic carbon in the central Arctic Ocean as revealed by ^{234}Th:^{238}U disequilibrium, *J. Geophys. Res.*, *115*, C10037, doi:10.1029/2009JC005595.

Codispoti, L., V. Kelly, A. Thessen, P. Matrai, S. Suttles, V. Hill, M. Steele, and B. Light (2013), Synthesis of primary production in the Arctic Ocean: III. Nitrate and phosphate based estimates of net community production, *Prog. Oceanogr.*, *110*, 126–150, doi:10.1016/j.pocean.2012.11.006.

Cota, G., L. Pomeroy, W. Harrison, E. Jones, F. Peters, W. Sheldon Jr., and T. Weingartner (1996), Nutrients, primary production and microbial heterotrophy in the southeastern Chukchi Sea: Arctic summer nutrient depletion and heterotrophy, *Mar. Ecol. Prog. Ser.*, *135*(1), 247–258.

Dosser, H. V., and L. Rainville (2016), Dynamics of the changing near-inertial internal wave field in the Arctic Ocean, *J. Phys. Oceanogr.*, *46*(2), 395–415, doi:10.1175/jpo-d-15-0056.1.

Fer, I. (2006), Scaling turbulent dissipation in an Arctic fjord, *Deep Sea Res., Part II.*, *53*, 77–95, doi:10.1016/j.dsr2.2006.01.003, IAPSO/SCOR Conference on Ocean Mixing.

Fer, I. (2009), Weak vertical diffusion allows maintenance of Cold Halocline in the Central Arctic, *Atmos. Oceanic Sci. Lett.*, *2*(3), 148–152, doi:10.1080/16742834.2009.11446789.

Garrett, C., and W. Munk (1975), Space-time scales of internal waves: A progress report, *J. Geophys. Res.*, *80*(3), 291–297, doi:10.1029/JC080i003p00291.

Gosselin, M., M. Levasseur, P. A. Wheeler, R. A. Horner, and B. C. Booth (1997), New measurements of phytoplankton and ice algal production in the Arctic Ocean, *Deep Sea Res., Part II*, *44*(8), 1623–1644, doi:10.1016/S0967-0645(97)00054-4.

Granskog, M., P. Assmy, S. Gerland, G. Spreen, H. Steen, and L. Smedsrud (2016), Arctic research on thin ice: Consequences of Arctic sea ice loss, *Eos Trans. AGU*, *97*, 22–26, doi:10.1029/2016eo044097.

Guthrie, J. D., J. H. Morison, and I. Fer (2013), Revisiting internal waves and mixing in the Arctic Ocean, *J. Geophys. Res. Oceans*, *118*, 3966–3977, doi:10.1002/jgrc.20294.

Haine, T. W., et al. (2015), Arctic freshwater export: Status, mechanisms, and prospects, *Global Planet. Change*, *125*, 13–35, doi:10.1016/j.gloplacha.2014.11.013.

Honjo, S., R. A. Krishfield, T. I. Eglinton, S. J. Manganini, J. N. Kemp, K. Doherty, J. Hwang, T. K. McKee, and T. Takizawa (2010), Biological pump processes in the cryopelagic and hemipelagic Arctic Ocean: Canada Basin and Chukchi Rise, *Prog. Oceanogr.*, *85*(34), 137–170, doi:10.1016/j.pocean.2010.02.009.

Iversen, T., et al. (2013), The Norwegian Earth system model, NorESM1-M—Part 2: Climate response and scenario projections, *Geosci. Model Dev.*, *6*(2), 389–415, doi:10.5194/gmd-6-389-2013.

Kunze, E., E. Firing, J. M. Hummon, T. K. Chereskin, and A. M. Thurnherr (2006), Global Abyssal mixing inferred from lowered ADCP Shear and CTD strain profiles, *J. Phys. Oceanogr.*, *36*(8), 1553–1576, doi:10.1175/JPO2926.1.

Lique, C., J. D. Guthrie, M. Steele, A. Proshutinsky, J. H. Morison, and R. Krishfield (2014), Diffusive vertical heat flux in the Canada Basin of the Arctic Ocean inferred from moored instruments, *J. Geophys. Res. Oceans*, *119*, 496–508, doi:10.1002/2013JC009346.

McPhee, M. G., G. A. Maykut, and J. H. Morison (1987), Dynamics and thermodynamics of the ice/upper ocean system in the marginal ice zone of the Greenland Sea, *J. Geophys. Res.*, *92*(C7), 7017–7031, doi:10.1029/JC092iC07p07017.

McPhee, M. G., T. P. Stanton, J. H. Morison, and D. G. Martinson (1998), Freshening of the upper ocean in the Arctic: Is perennial sea ice disappearing?, *Geophys. Res. Lett.*, *25*(10), 1729–1732, doi:10.1029/98GL00933.

Morison, J., R. Kwok, C. Peralta-Ferriz, M. Alkire, I. Rigor, R. Andersen, and M. Steele (2012), Changing Arctic Ocean freshwater pathways, *Nature*, *481*(7379), 66–70, doi:10.1038/nature10705.

Morison, J. H., C. E. Long, and M. D. Levine (1985), Internal wave dissipation under sea ice, *J. Geophys. Res.*, *90*(C6), 11,959–11,966.

Nummelin, A., M. Ilicak, C. Li, and L. H. Smedsrud (2015), Consequences of future increased Arctic runoff on Arctic Ocean stratification, circulation, and sea ice cover, *J. Geophys. Res. Oceans*, *121*, 617–637, doi:10.1002/2015jc011156.

Olli, K., et al. (2007), The fate of production in the central Arctic Ocean—Top-down regulation by zooplankton expatriates?, *Prog. Oceanogr.*, *72*(1), 84–113, doi:10.1016/j.pocean.2006.08.002.

Osborn, T. R. (1980), Estimates of the local rate of vertical diffusion from dissipation measurements, *J. Phys. Oceanogr.*, *10*(1), 83–89, doi:10.1175/1520-0485(1980)010<0083:EOTLRO>2.0.CO;2.

Pomeroy, L. R. (1997), Primary production in the Arctic Ocean estimated from dissolved oxygen, *J. Mar. Syst.*, *10*(14), 1–8, doi:10.1016/S0924-7963(96)00059-0.

Randelhoff, A., A. Sundfjord, and A. H. H. Renner (2014), Effects of a shallow pycnocline and surface meltwater on sea ice-ocean drag and turbulent heat flux, *J. Phys. Oceanogr.*, *44*(8), 2176–2190, doi:10.1175/jpo-d-13-0231.1.

Randelhoff, A., A. Sundfjord, and M. Reigstad (2015), Seasonal variability and fluxes of nitrate in the surface waters over the Arctic shelf slope, *Geophys. Res. Lett.*, *42*, 3442–3449, doi:10.1002/2015GL063655.

Randelhoff, A., I. Fer, A. Sundfjord, J.-E. Tremblay, and M. Reigstad (2016), Vertical fluxes of nitrate in the seasonal nitracline of the Atlantic sector of the Arctic Ocean, *J. Geophys. Res. Oceans*, *121*, doi:10.1002/2016JC011779, in press.

Sakamoto, C. M., K. S. Johnson, and L. J. Coletti (2009), Improved algorithm for the computation of nitrate concentrations in seawater using an in situ ultraviolet spectrophotometer, *Limnol. Oceanogr. Methods*, *7*, 132–143.

Sirevaag, A., and I. Fer (2012), Vertical heat transfer in the Arctic Ocean: The role of double-diffusive mixing, *J. Geophys. Res.*, *117*, C07010, doi:10.1029/2012JC007910.

Timmermans, M.-L., J. Toole, R. Krishfield, and P. Winsor (2008), Ice-tethered profiler observations of the double-diffusive staircase in the Canada basin thermocline, *J. Geophys. Res.*, *113*, C00A02, doi:10.1029/2008JC004829.

Timmermans, M.-L., A. Proshutinsky, R. A. Krishfield, D. K. Perovich, J. A. Richter-Menge, T. P. Stanton, and J. M. Toole (2011), Surface freshening in the Arctic Ocean's Eurasian Basin: An apparent consequence of recent change in the wind-driven circulation, *J. Geophys. Res.*, *116*, C00D03, doi:10.1029/2011JC006975.

Torres-Valdés, S., T. Tsubouchi, S. Bacon, A. C. Naveira-Garabato, R. Sanders, F. A. McLaughlin, B. Petrie, G. Kattner, K. Azetsu-Scott, and T. E. Whitledge (2013), Export of nutrients from the Arctic Ocean, *J. Geophys. Res. Oceans*, *118*, 1625–1644, doi:10.1002/jgrc.20063.

Tremblay, J.-E., L. G. Anderson, P. Matrai, P. Coupel, S. Bélanger, C. Michel, and M. Reigstad (2015), Global and regional drivers of nutrient supply, primary production and CO_2 drawdown in the changing Arctic Ocean, *Prog. Oceanogr.*, *139*, 171–196, doi:10.1016/j.pocean.2015.08.009.

Ulfsbo, A., N. Cassar, M. Korhonen, S. van Heuven, M. Hoppema, G. Kattner, and L. G. Anderson (2014), Late summer net community production in the central Arctic Ocean using multiple approaches, *Global Biogeochem. Cycles*, *28*, 1129–1148, doi:10.1002/2014GB004833.

Wassmann, P., et al. (2004), Particulate organic carbon flux to the Arctic Ocean sea floor, in *The Organic Carbon Cycle in the Arctic Ocean*, edited by R. Stein and R. W. Macdonald, pp. 101–138, Springer, Berlin, doi:10.1007/978-3-642-18912-8.

Yamazaki, H., and T. Osborn (1990), Dissipation estimates for stratified turbulence, *J. Geophys. Res.*, *95*(C6), 9739–9744, doi:10.1029/JC095iC06p09739.

Zheng, Y., P. Schlosser, J. H. Swift, and E. Jones (1997), Oxygen utilization rates in the Nansen Basin, Arctic Ocean: Implications for new production, *Deep Sea Res., Part I*, *44*(12), 1923–1943, doi:10.1016/S0967-0637(97)00046-0.

II

Randelhoff, A., A. Sundfjord, and M. Reigstad (2015), Seasonal variability and fluxes of nitrate in the surface waters over the Arctic shelf slope, *Geophysical Research Letters*, *42*, 3442–3449, doi:10.1002/2015gl063655.

AGU PUBLICATIONS

Geophysical Research Letters

RESEARCH LETTER

10.1002/2015GL063655

Seasonal variability and fluxes of nitrate in the surface waters over the Arctic shelf slope

Achim Randelhoff[1,2], **Arild Sundfjord**[2], **and Marit Reigstad**[1]

[1] Institute for Arctic and Marine Biology, University of Tromsø, Tromsø, Norway, [2] Norwegian Polar Institute, Tromsø, Norway

Key Points:

- First year-round moored observations of nitrate in the Eastern Arctic Ocean
- Vertical nitrate fluxes are supported by weakened stratification in fall
- Nitrate near depletion indicates nutrient limitation of annual new production

Correspondence to:
A. Randelhoff,
achim@npolar.no

Citation:
Randelhoff, A., A. Sundfjord, and M. Reigstad (2015), Seasonal variability and fluxes of nitrate in the surface waters over the Arctic shelf slope, *Geophys. Res. Lett.*, *42*, doi:10.1002/2015GL063655.

Received 6 MAR 2015
Accepted 7 APR 2015
Accepted article online 14 APR 2015

Abstract Understanding the present state and possible future scenarios of Arctic Ocean primary productivity has been hampered by the scarcity of year-round nutrient measurements. Here the first yearlong moored time series of near-surface nitrate concentrations in the Eastern Arctic, together with hydrography, currents, and chlorophyll *a* fluorescence, is reported from the shelf slope northeast of Svalbard. Variability was dominated by the inflow of Atlantic Water (AW). Nitrate was near depleted during July–September and reached a maximum concentration of 10 μM in March. Vertical nitrate gradients were eroded by mid-December, demonstrating the importance of the AW in breaking down upper ocean stratification during fall. Upward nitrate fluxes through the nitracline in the AW inflow region during fall were 2.5 ± 0.5 mmol m^{-2} d^{-1}. The spring bloom triggered extensive nitrate drawdown from June, from which an annual new production of 31 g C m^{-2} was estimated.

1. Introduction

The Arctic Ocean (AO) primary production (PP) is subject to two major constraints: Light limitation resulting both from the thick, perennial ice cover and the total absence of sunlight during the polar night and nutrient limitation by nitrate depletion due to the strong stratification in large parts of the deep basins and the Western Arctic [*Codispoti et al.*, 2013]. With the currently retreating ice cover [e.g., *Comiso*, 2012], primary production could be expected to increase as more light becomes available [*Arrigo et al.*, 2008; *Arrigo and van Dijken*, 2011]. However, the associated changes in stratification and thus upward mixing of nutrients are not well understood, such that the reliability of large-scale modeling of future AO PP largely depends on current constraints of nitrate concentrations in the ice-covered areas [*Vancoppenolle et al.*, 2013].

Since river runoff draining into the AO contains little nutrients [*Codispoti et al.*, 2013], the inflows of Atlantic Water (AW) via Fram Strait and the Barents Sea and of Pacific Water via Bering Strait are the dominant sources of nutrients for the AO [*Torres-Valdés et al.*, 2013; *Codispoti et al.*, 2013]. Because of its high salinity and successive cooling, the AW that enters the AO sinks down to intermediate depths, from where it provides nutrients to the surface waters through turbulent diapycnal mixing.

Without light limitation, the spring bloom rapidly depletes the nitrate pool in the euphotic zone, and nitrate concentrations ($\mathcal{N}$) remain low throughout summer by a combination of continued nitrate consumption and suppression of vertical mixing caused by the developing stratification [e.g., *Carmack et al.*, 2006]. In this respect, two quantities are of interest, dominated by the physical setting rather than the biological fluxes: The vertical flux of nitrate that supplies the productive surface layer during summer and the replenishment of the nitrate pool during fall and winter, which in turn determines the prebloom state for the next season. However, few observations of vertical nutrient fluxes exist in the AO [*Bourgault et al.*, 2011]. During fall, primary production ceases, stratification weakens, and surface nutrient concentrations start to increase again, and more so on the shelf [e.g., *Aagaard and Carmack*, 1994] than in the central AO. The upper part of the continental slope is an interesting region at the boundary between the deep basin and the shelf seas, with possibly elevated mixing from strong boundary current shear and possible upwelling during ice-free conditions [*Carmack and Chapman*, 2003].

Data on nutrient concentrations in the AO are sparse not only due to ice restricting access to the region but also the need for time-consuming wet chemistry to analyze water samples, which limits temporal and spatial coverage. In situ ultraviolet spectrophotometry is a tool for real-time, in situ measurements of nitrate [*Johnson and Coletti*, 2002] which allows for continuous and autonomous long-term deployments [e.g., *Johnson et al.*, 2006]. This facilitates monitoring of $\mathcal{N}$ even in remote areas, but to our knowledge, this is the first such data set reported from the Eastern AO.

Starting in 2012, a project monitoring the AW boundary current north of Svalbard has been collecting data from a line of instrumented moorings and annual cruises. Using data from this program (A-TWAIN: Long-term variability and trends in the Atlantic Water inflow region), the present study aims to give insight into the seasonal nitrate cycle in the surface waters and the interaction between the AW inflow and the local Arctic water masses by analysis of mooring data from the upper slope north of Svalbard.

2. Methods

2.1. Data

We present a yearlong data record from a mooring deployed between September 2012 and September 2013 at 81°30′N, 30°51′E, on the shelf slope north of Svalbard over a water depth of approximately 800 m, supplemented by data from hydrographical stations made during the mooring turnaround cruises.

Two SBE16plus V2 (SeaCAT) units were moored at approximately 20 and 40 m depth, sampling temperature T, salinity S (in the following, given on the practical salinity scale), chlorophyll *a* fluorescence (chl *a*), and pressure P 4 times per hour. SBE16plus data were processed using precruise calibration coefficients provided by Seabird. A Satlantic In Situ Ultraviolet Spectrophotometer V3 nitrate sonde (ISUS) was moored approximately 1 m below the upper SeaCAT, sampling absorption between 170 and 400 nm in a 1 cm cuvette with a sampling "burst" of 13 light and 2 dark frames every 2 h.

An up-looking RD Instruments Sentinel 300 kHz acoustic Doppler current profiler (ADCP) was mounted at approximately 90 m depth. In September 2012 and 2013, conductivity-temperature-depth (CTD) casts were taken at the mooring location, along with water samples across the water column to determine nutrient and chl *a* concentrations.

2.2. ISUS Processing and Nitrate Bottle Samples

ISUS data processing followed *Sakamoto et al.* [2009], using their temperature compensated, salinity subtracted algorithm and a wave band of 217–240 nm. In situ temperature and salinity were taken as measured by the SeaCAT mounted 1 m above the ISUS. Low detector intensities close to the dark currents during parts of June, July, and August (presumably due to very turbid waters) rendered the spectral fitting method useless, thus preventing calculation of nitrate values for those periods. In addition, the ISUS did not sample during a 3 week period in March 2013 for unknown reasons. A data point was discarded if its standard deviation (based on 13 samples for each burst) exceeded 0.2 μM, which was coincident with low detector intensities. That part of the nitrate data which was not discarded had an average standard deviation of 0.12 μM, and the minimum detectable concentration difference is therefore approximately 0.5 μM (three standard deviations [*Johnson and Coletti*, 2002]).

The nitrate bottle samples were processed using a Flow Solution IV analyzer by O.I. Analytical, USA. The analyzer was calibrated using reference seawater from Ocean Scientific International Ltd., UK, and the detection limit is 0.02 μM.

Comparing bottle samples taken during the turnover cruises with ISUS values is difficult due to large vertical $\mathcal{N}$ gradients during September, and some temporal variation around the time points in question. From 15 profiling deployments of the same instrument in January 2014 (unpublished data), we infer a mean additive correction of 2 μM, the ISUS being biased high. This is consistent with bottle samples taken during the turnover cruises, but we acknowledge an overall uncertainty of approximately 1 μM in $\mathcal{N}$. Note that this introduces a large relative uncertainty at small $\mathcal{N}$, and one has to be careful about interpreting values $\mathcal{N} < 1$ μM.

Note that the bottle sample analysis yields values for the sum of nitrate and nitrite concentrations, but levels of nitrite in the AO are generally much lower than that of nitrate [e.g., *Codispoti et al.*, 2005]. We therefore refer to both nitrate concentrations measured by the ISUS and nitrate plus nitrite concentrations measured in bottle samples as nitrate concentration ($\mathcal{N}$).

2.3. Chlorophyll *a*

Analysis of chl *a* samples from the vertical profiles followed standard procedures based on *Holm-Hansen and Riemann* [1978] as described by *Reigstad et al.* [2008]. The samples were frozen on board after filtration, until analysis <4 weeks after sampling. No calibration of the chl *a* fluorescence sensors mounted on

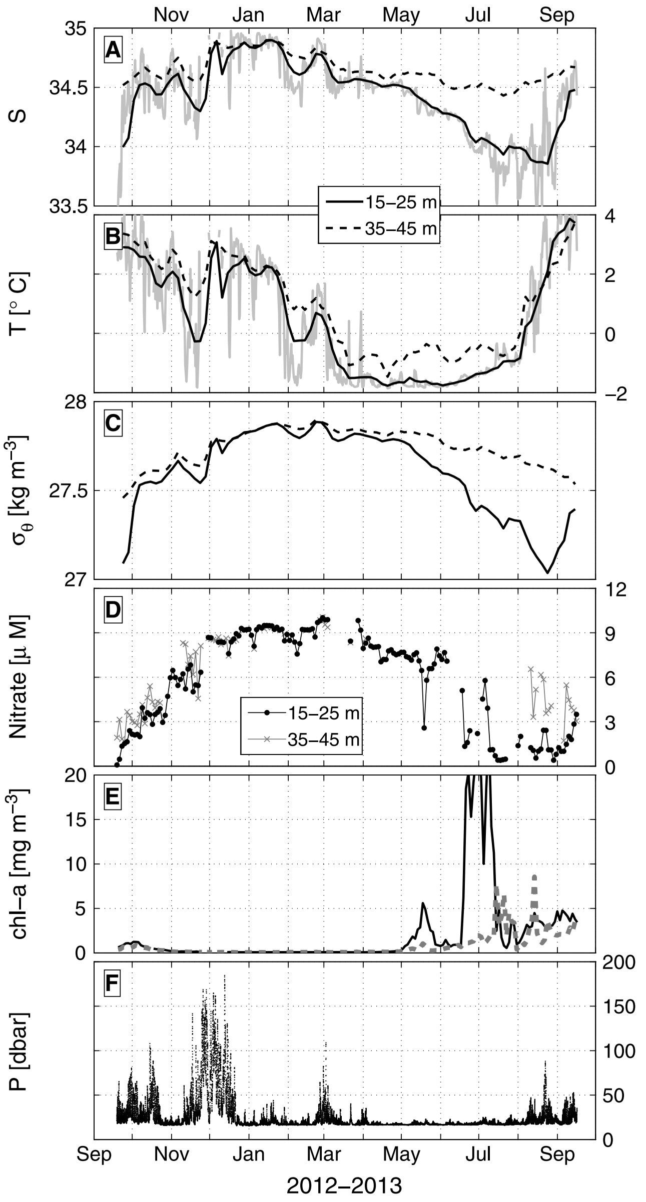

Figure 1. ISUS and SeaCAT data time series. To account for vertical motion of the mooring, only data from the indicated depth intervals are plotted (excluding Figure 1f). (a, b) Salinity and temperature between 15 and 25 (grey: 12 h mean, black solid: running 15 day mean) and 35 and 45 m (broken, running 15 day mean). (c) σ_θ (running 15 day mean) between 15 and 25 (solid) and 35 and 45 m (broken line). (d) Nitrate, 15–25 m (black, dots) and 35–45 m (grey, crosses). (e) Chl *a* fluorescence at 15–25 (solid black) and 35–45 m (broken, grey). (f) Pressure at the upper SeaCAT, mounted 1 m above ISUS.

the moored SeaCATs was done. The values plotted in Figure 1e therefore have to be regarded as qualitative values.

2.4. Vertical Profiles

The moored instruments underwent considerable dive-and-rise cycles during the deployment period, most notably in November and December 2012, as measured by the SeaCATs' pressure sensors (Figure 1f). These dives and climbs frequently happened in the course of less than 24 h, enabling us to infer approximate vertical profiles of the upper ~150–200 m. The overall coverage is patchy, but good enough during fall 2012 to infer monthly averages. Potential density (σ_θ) and $\mathcal{N}$ data were sorted into 18 depth bins of 10 m depth between 15 and 195 m and further averaged in 30 day intervals to account for the large variability on time scales of days to weeks. Although some density profiles show negative gradients (Figure 3e), this is rather an artifact of temporal variability, resolved differently at different depths, than actual unstable stratification. Overall results were not sensitive to the exact averaging method, and the profiles could not be improved consistently by more elaborate methods.

2.5. Ice and Wind Conditions

Advanced Microwave Scanning Radiometer 2 (AMSR-2) data (September 2012 to October 2013) were downloaded from http://www.iup.uni-bremen.de:8084/amsr2data/asi_daygrid_swath/n3125/ on 8 April 2014. Ice concentrations were gridded on a stereographic projection centered at the mooring location and averaged inside a radius of 20 km around the mooring location. Wind velocity from the nearest grid point (81.75°N, 30.75°E) was taken from the ERA-Interim global reanalysis [*Dee et al.*, 2011], downloaded from http://apps.ecmwf.int/datasets/data/interim_full_daily/ on 28 August 2014.

3. Results

3.1. Seasonal Cycle

T, *S*, and $\mathcal{N}$ exhibited a clear cycle through the 1 year data record (Figure 1). While *S* had a clear seasonal maximum roughly in December–January and a minimum in July–August 2013 (Figure 1), the temperature minimum was spread over April–July 2013, and there was no isolated maximum but rather two peaks, one in

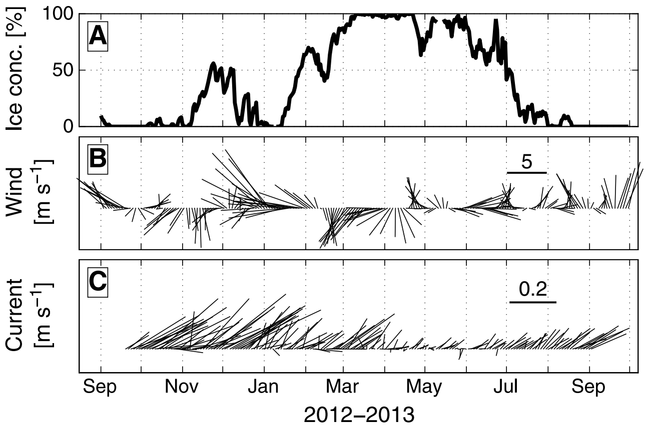

Figure 2. (a) Average ice concentration in a radius of 20 km around the mooring location (from AMSR-2). The radius was chosen arbitrarily, and the mean concentration is not sensitive to its exact value. (b) Ten meter wind (15 day running mean) at 81.75°N, 30.75°E from ERA-Interim. (C) The 15–25 m averaged current (2 day mean) from upward looking ADCP, with north up and east right.

September and one in December 2012, separated by a ~3°C cooling and warming in between. Variation in T and S on timescales of days to weeks was much larger in winter than in summer. Nitrate was at its maximum winter concentration between January and March (Figure 1) with a maximum of 10 μM in March, and it was near depleted in the summer months July and August, with the largest drawdown starting in June.

Although wind direction varied considerably, water currents at 15–25 m followed the shelf slope eastward at maximum speeds of roughly 0.4 m s^{-1}, and with little influence of the wind stress on the overall flow direction (Figure 2).

3.2. Hydrographical Profiles

At the hydrographical stations during the cruises both in 2012 and 2013, the September mixed layer was about 25 m deep, with temperatures of about 2.4°C (Figure 3). The bottle sample profile from September 2012 (Figure 3) showed a nutrient-depleted surface layer of about 20 m depth, overlying a nitracline extending to roughly 100–150 m. Mixed-layer nitrate concentrations were higher (about 2 μM) in 2013, but the nitracline started at 30–50 m in both 2012 and 2013. Chl *a* fluorescence was very low in September both in 2012 and 2013, indicating that most primary production had ceased by then.

3.3. Vertical Structure and Nitrate Fluxes

From vertical profiles of nitrate (Figure 3), we infer an initially strong gradient which was eroded throughout fall. Sometime in mid-December, values reached $\mathcal{N} \approx 9$ μM and the nitrate gradient vanished where the pycnocline was located in the previous summer (25–45 m), but the nitrate concentration itself continued to rise throughout winter to approximately 10 μM. The pattern for σ_θ profiles was similar, with vanishing stratification in December. From the nitrate profiles during fall, we can calculate nitrate fluxes as follows. The conservation equation for $\mathcal{N}$ is

$$\partial_t \mathcal{N} + U\partial_x \mathcal{N} = \partial_z F_{\mathcal{N}} + Q_{\mathcal{N}} \,, \tag{1}$$

where $F_{\mathcal{N}}$ is the vertical turbulent nitrate flux, $Q_{\mathcal{N}}$ is a source term, and U is the mean horizontal (advection) velocity. Assuming no source or sink,

$$\Sigma F_{\mathcal{N}}(h) \equiv F_{\mathcal{N}}(h) - \int_0^h \mathrm{d}z U\partial_x \mathcal{N} \simeq \int_0^h \mathrm{d}z\, \partial_t \mathcal{N} \,, \tag{2}$$

where $\Sigma F_{\mathcal{N}}$ represents the total nitrate flux into the water column between depth h and the surface. In September 2012, the well-mixed layer was approximately 25 m deep (Figure 3), and the difference in σ_θ between 20 and 40 m is small from October 2012 through May 2013 (Figure 1). Therefore, we assume constant $\mathcal{N}$ from the 15–25 m depth bin and up throughout the period of September–January. Profiles of $\partial_t \mathcal{N}$ are then approximated from the profiles "Sep/Oct" through "Dec/Jan" (Figure 3) to give three independent estimates of $\Sigma F_{\mathcal{N}}$ throughout fall, the mean of which is 2.5 ± 0.5 mmol m^{-2} d^{-1} (1 standard deviation) at $h = 35$ m, which was in the uppermost part of the nitracline in September 2012. The result is not strongly sensitive to h.

4. Discussion

4.1. Hydrography

The measurements show a highly variable environment, with frequent shifts between more Atlantic (warmer, saltier) and more Arctic-influenced (colder, fresher) water masses, dominating variability on time scales shorter than a few months (Figure 4). This variability was strongest in winter, possibly associated with frequent

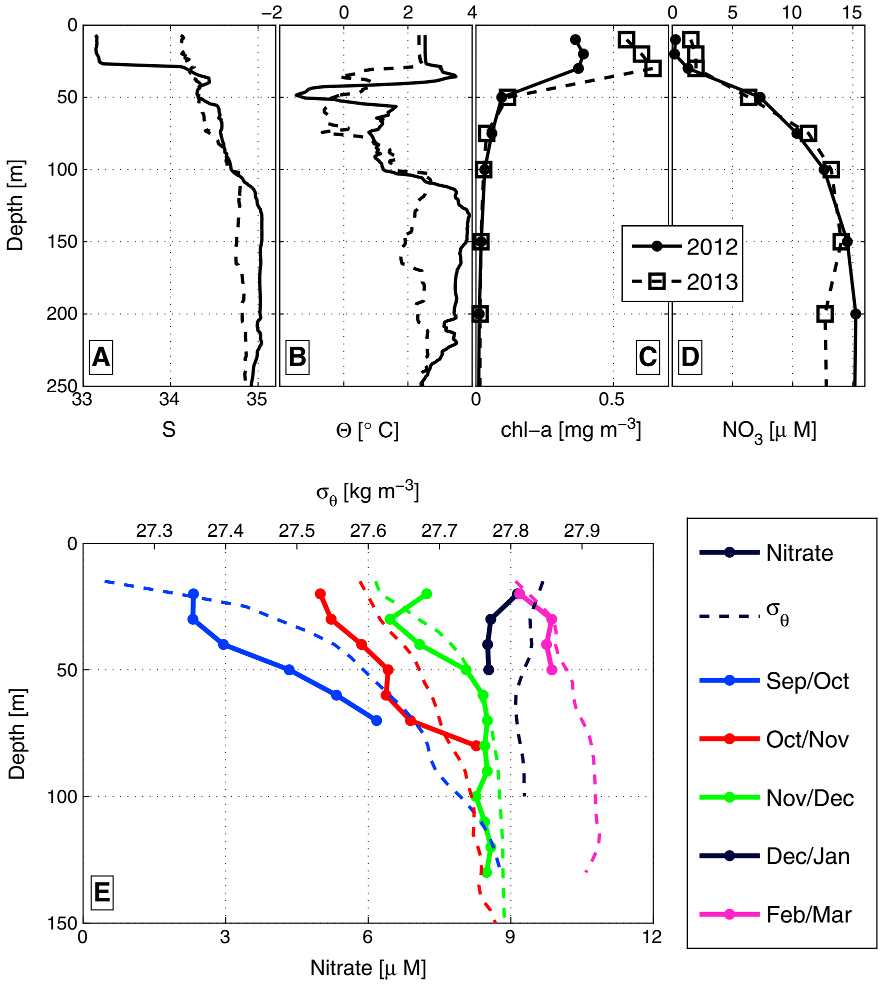

Figure 3. CTD profiles of (a) salinity, (b) potential temperature, (c) chl *a* fluorescence (from bottle samples), and (d) nitrate (from bottle samples) at the mooring location on 17 September 2012 (solid) and 16 September 2013 (dashed). (e) Vertical profiles of $\mathcal{N}$ and potential density (σ_θ), inferred from dives of the mooring.

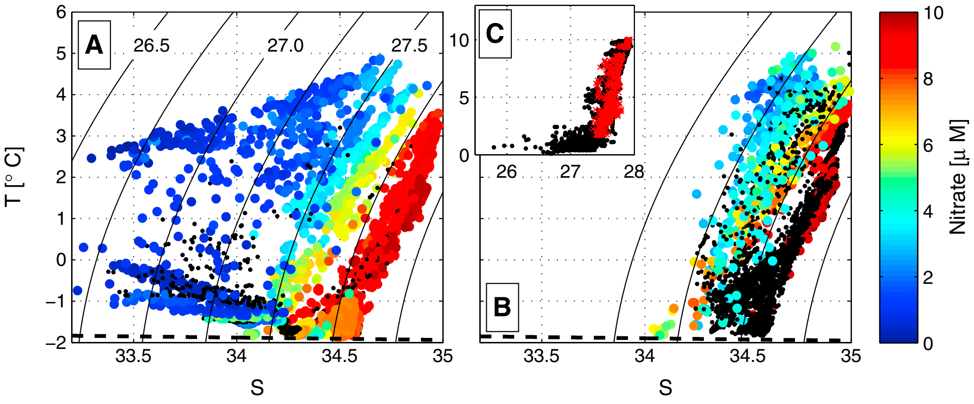

Figure 4. *T-S* plots at (a) 15–25 m and (b) 35–45 m. Nitrate concentration ($\mathcal{N}$) is color coded where available, otherwise black. The dashed line shows the seawater freezing point; isolines are σ_θ (labels in kg m^{-3}). (c) $\mathcal{N}$ (μM) (on the *y* axis) versus σ_θ (kg m^{-3}) (on the *x* axis) for 15–25 m (black dots) and 35–45 m (red crosses).

advection events of sea ice and Arctic water masses which mixed with the AW inflow. Summer was characterized by colder and fresher water, and less variability. This is reflected in the current measurements, which show much larger velocities in the October–March period than in April–July.

In the same area, *Ivanov et al.* [2009] found a significant seasonal signal in the *T-S* properties of the AW at depths ranging between 70 and 215 m, with a clear distinction between warmer/saltier and colder/fresher water types, present during winter and summer, respectively. To assess the influence of the AW variability on surface measurements, we compare density ratios $R = \alpha\Delta T/\beta\Delta S$, where α and β are the thermal expansion and haline contraction coefficients evaluated at the annual-mean T and S and the respective depths and ΔT, ΔS are the seasonal amplitudes of temperature and salinity. *Ivanov et al.* [2009] found $R = 4.2$–15.5 at depths of 70–215 m, versus far lower cooling versus freshening ratios (0.34 and 0.81 at 15–25 and 35–45 m, respectively) in our study. This indicates that the surface water variability was dominated by the freeze/melt cycle of the ice cover instead of the AW cooling/warming cycle. Even so, the weakening of the stratification through fall 2012 (Figure 3) was aided by the inflow of high-salinity near-surface AW that helped to break down salinity stratification when freshwater input from sea ice melt ceased after summer.

4.2. Nitrate Variability

The seasonal nitrate variability reflected the overall cycle of a bloom in summer, depletion or near depletion following the bloom, and replenishment during the following fall and winter. The brief low-$\mathcal{N}$-high-chl *a* event in mid-May was likely due to advection of a small patch that had been productive earlier and may or may not have been productive when it passed the mooring. The abrupt nitrate drawdown starting in June was presumably caused by the onset of primary production (Figure 1e). This is consistent with the retreat of the ice cover (Figure 2a), which allowed sunlight to enter the upper ocean and trigger the bloom, possibly in combination with strengthening stratification due to enhanced ice melt. However, nitrate drawdown was not monotonous. Instead, $\mathcal{N}$ was highly variable during the productive season, indicating horizontal patchiness, as has previously been observed in the northern Barents Sea [*Falk-Petersen et al.*, 2000].

$\mathcal{N}$ was strongly related to σ_θ, where the $\mathcal{N} - \sigma_\theta$ slopes were about the same for the intervals between 15 and 25 and 35 and 45 m ($R^2 = 0.71$ and 0.68, respectively; see Figure 4c) at $\mathcal{N} > \sim 2$ μM, below which more freshening occurred than $\mathcal{N}$ reduction. It is not clear what made this relation so tight, even though it stresses the coupling of primary producers to stratification.

4.3. Nitrate Fluxes During Fall

The nitrate flux $\Sigma F_{\mathcal{N}}$ potentially comprises four contributions: Vertical flux $F_{\mathcal{N}}$, nitrate uptake by phytoplankton, nitrification, and horizontal advection. In the following, we argue that the last three are minor during fall and thus $F_{\mathcal{N}} \approx \Sigma F_{\mathcal{N}}$. Quantifying the vertical nitrate fluxes during fall gives insight into how vertical mixing is controlled by the physical conditions developed during summer and thus constrains the postbloom supply of allochthonous nitrate to the euphotic zone.

Chl *a* fluorescence was close to zero throughout the September 2012 to January 2013 period, so nitrate uptake vanishes. *Tremblay et al.* [2008] concluded that for their data set from the coastal Beaufort Sea, nitrification accounted for 1.4 nM d^{-1}, or 11%, of the observed $\mathcal{N}$ increase after the establishment of the fast ice cover. Assuming that this rate (realistically the magnitude, but the same even holds when considering the ratio) approximately applies to our study region, nitrification accounted at most for a small part of $\Sigma F_{\mathcal{N}}$.

As stated earlier, the current regime was clearly dominated by the inflow of Atlantic Water [see, e.g., *Schauer et al.*, 2004] through the whole measurement period. This is important to note during the following discussion of advective fluxes. Advection may be split into two parts: Along slope (with the AW) and cross slope. Since $\mathcal{N}$ can be expected to evolve differently on and off the shelf, there might be a horizontal cross-slope gradient. Overall, cross-slope transport events were only episodic, since upper ocean currents during the study period were mainly eastward and along shelf (that is, following the AW; see Figure 2) especially during fall, indicating that integrated over the whole fall-winter period, advection of AW would dominate over cross-slope transport. During fall, one might speculate that farther upstream, the AW inflow is less vertically stratified, enhancing $F_{\mathcal{N}}$ and setting up a horizontal downstream gradient, thus leading to a positive contribution from advection. However, since summertime surface AW is also depleted in nitrate, the vertical $\mathcal{N}$ gradient would be similar upstream of the mooring, such that $F_{\mathcal{N}} \approx \Sigma F_{\mathcal{N}}$ when integrated over the upstream region.

To see whether $\Sigma F_{\mathcal{N}}$ is a reasonable magnitude for a vertical turbulent flux, we can also compare the eddy diffusivities K estimated from nitrate fluxes and from a theoretical dissipation scaling (see Appendix A). The results are consistent with the arguments above and indicate that $\Sigma F_{\mathcal{N}}$ is an upper bound on $F_{\mathcal{N}}$.

Bourgault et al. [2011] reported $F_{\mathcal{N}} = 0.5$ mmol m^{-2} d^{-1} from fall and winter observations in the Amundsen Gulf, that is, with 90% ice cover and in a strongly stratified water column. They also compile several observations of turbulent nitrate fluxes in various parts of the world ocean, with fluxes varying greatly between about 0.01–10 mmol m^{-2} d^{-1}. *Sundfjord et al.* [2007] reported 0.1-2 mmol m^{-2} d^{-1} for the Barents Sea (May and July, 40–90% ice cover). In general, we can expect somewhat higher fluxes due to persistently high wind speeds during fall/winter (Figure 2b). We conclude that our estimate for $F_{\mathcal{N}}$ is reasonable but might contain some contribution from horizontal, advective fluxes.

4.4. Nitrate Drawdown by Primary Production

Following *Codispoti et al.* [2013], we estimated annual new production from nitrate drawdown during the productive period. *Tremblay et al.* [2008] corrected drawdown estimates for changes in salinity, implicitly assuming that any freshwater input was equally depleted in nitrate. For the present data, dilution plays only a small role since the salinity changes by approximately 2.5% between winter and summer. Maximum $\mathcal{N}$ during winter was 10 μM, which means that winter concentrations reach summer concentrations at 70 m. Integrating down to this depth is thus in line with *Codispoti et al.* [2013]. A Redfield C:N ratio [*Redfield et al.*, 1963] of 106:16 (although higher values have been proposed [e.g., *Sambrotto et al.*, 1993], we choose this value for consistency) yields a new production of 31 g C m^{-2}. This coincides with the value *Codispoti et al.* [2013] found for the Nordic Seas and is halfway between their estimates for the Barents Sea (47 g C m^{-2}) and the Eurasian Basin (13 g C m^{-2}), stressing the location of the mooring at the boundary between the shelf and the AO basin.

5. Summary and Perspectives

We present the first annual time series of $\mathcal{N}$ reported from the eastern AO. Based on 1 year of mooring data, we describe the seasonal nitrate cycle together with hydrography, currents, and chl *a* in the surface waters over the shelf slope north of Svalbard. $\mathcal{N}$ followed a seasonal cycle with a maximum in March and a minimum in July–August, linked to abrupt nitrate drawdown by primary producers starting in June, with the timing likely controlled by the presence of ice cover and developing stratification.

In fall and winter 2012, the upward nitrate flux through the nitracline in the AW inflow region was $F_{\mathcal{N}} \approx (2.5 \pm 0.5)$ mmol m^{-2} d^{-1}, constraining the postbloom nitrate supply to the mixed layer. Stratification probably acted as an inhibitor of vertical mixing, and only when stratification became small, mixing was sustained deep enough to erode the vertical $\mathcal{N}$ gradient.

The early date by which the surface nitrate pool was replenished in winter suggests that a lengthening of the productive season has the potential to increase annual new production in the AW inflow area. However, during almost two of the productive summer months, PP was likely not light limited, but nutrient limited, meaning that the potential for increased new production in a scenario with less ice is limited in this location.

The large temporal variability especially during the beginning of the productive season indicates spatial patchiness. This makes it necessary to account for large horizontal gradients in nutrient concentrations, light and ecosystem characteristics, even though the surface waters were clearly dominated by the steadily inflowing modified AW. Caution is thus required when interpreting the temporally isolated vertical profiles usually measured on ship-based campaigns.

Appendix A: Diffusivity Estimates From $F_{\mathcal{N}}$ and HWF Scaling

Estimating the gradient $\partial_z \mathcal{N}$ across 25–45 m from the vertical profiles during the same period Sep/Oct to Dec/Jan, $K = -\frac{F_{\mathcal{N}}}{\partial_z \mathcal{N}} = (5 \pm 1) \cdot 10^{-4}$ m^2 s^{-1} (1 standard deviation from three pairs of flux/gradient estimates). Measurements of eddy diffusivities are generally scattered over orders of magnitude, which makes it difficult to compare this value with observations. To estimate K from stratification and internal wave energy, we use the Henyey-Wright-Flattè (HWF) scaling for the dissipation of turbulent kinetic energy ϵ [*Henyey et al.*, 1986] following *Wijesekera et al.* [1993, equation (8c)]:

$$\epsilon = \frac{1.67}{\pi} \left(bN_0\right)^{-2} f \cosh^{-1} \left(\frac{N}{f}\right) j_*^2 E_{\mathrm{meas}}^2 \tag{A1}$$

with thermocline scale depth $b = 1300$ m, reference buoyancy frequency $N_0 = 3$ cph, and vertical mode scale number $j_* = 3$ and then applying $K = 0.2\epsilon/N^2$ [*Osborn*, 1980]. E_{meas} is estimated as $(\Phi_{uu}+\Phi_{vv})/2$, where $\Phi_{uu,vv}$ are power density spectra of 10 day records of horizontal velocity (u,v) at 35 m depth integrated between f (Coriolis frequency) and 1 cph, neglecting potential energy for simplicity since most of the energy is near inertial. Buoyancy frequency N^2 is estimated as finite difference between 20 and 40 m. Results depend on the exact depth used for horizontal velocities and the time window used to calculate successive spectra but are generally scattered between $K \approx (1-5)\cdot 10^{-4}$ m^2 s^{-1}, which means good agreement with the reasoning that $F_{\mathcal{N}}$ is equal to or smaller than $\Sigma F_{\mathcal{N}}$, especially considering the large uncertainties surrounding dissipation scaling in the ocean.

Acknowledgments
The data used in this study were collected through the project "Long-term variability and trends in the Atlantic Water inflow region" (A-TWAIN), funded by the Arctic Ocean program at the FRAM-High North Research Centre for Climate and the Environment and are accessible by contacting achim@npolar.no. A.R.'s work is supported by the project "CARBON BRIDGE: Bridging marine productivity regimes: How Atlantic advective inflow affects productivity, carbon cycling and export in a melting Arctic Ocean," a Polar Programme (project 226415) funded by the Norwegian Research Council. Vladimir Pavlov provided the processed ADCP data, and Sigrid Øygarden collected the bottle samples. Bottle sample processing was done by Svein Kristiansen (nitrate) and SØ (chl *a*). We thank Ilker Fer and two anonymous reviewers for helpful comments that improved the manuscript and the captain and crew of R/V *Lance* for support in the field.

The Editor thanks two anonymous reviewers for their assistance in evaluating this paper.

References

Aagaard, K., and E. C. Carmack (1994), The Arctic Ocean and climate: A perspective, in *The Polar Oceans and Their Role in Shaping the Global Environment*, edited by O. M. Johannessen, R. D. Muench, and J. E. Overland, pp. 5–20, AGU, Washington, D. C., doi:10.1029/GM085p0005.

Arrigo, K. R., and G. L. van Dijken (2011), Secular trends in Arctic Ocean net primary production, *J. Geophys. Res.*, *116*, C09011, doi:10.1029/2011JC007151.

Arrigo, K. R., G. van Dijken, and S. Pabi (2008), Impact of a shrinking Arctic ice cover on marine primary production, *Geophys. Res. Lett.*, *35*, L19603, doi:10.1029/2008GL035028.

Bourgault, D., C. Hamel, F. Cyr, J.-E. Tremblay, P. S. Galbraith, D. Dumont, and Y. Gratton (2011), Turbulent nitrate fluxes in the Amundsen Gulf during ice-covered conditions, *Geophys. Res. Lett.*, *38*, L15602, doi:10.1029/2011GL047936.

Carmack, E., and D. C. Chapman (2003), Wind-driven shelf/basin exchange on an Arctic shelf: The joint roles of ice cover extent and shelf-break bathymetry, *Geophys. Res. Lett.*, *30*(14), 1778, doi:10.1029/2003GL017526.

Carmack, E., D. Barber, J. Christensen, R. Macdonald, B. Rudels, and E. Sakshaug (2006), Climate variability and physical forcing of the food webs and the carbon budget on panarctic shelves, *Prog. Oceanogr.*, *71*(2–4), 145–181, doi:10.1016/j.pocean.2006.10.005.

Codispoti, L., C. Flagg, V. Kelly, and J. H. Swift (2005), Hydrographic conditions during the 2002 SBI process experiments, *Deep Sea Res., Part II*, *52*(24–26), 3199–3226, doi:10.1016/j.dsr2.2005.10.007.

Codispoti, L., V. Kelly, A. Thessen, P. Matrai, S. Suttles, V. Hill, M. Steele, and B. Light (2013), Synthesis of primary production in the Arctic Ocean: III. Nitrate and phosphate based estimates of net community production, *Prog. Oceanogr.*, *110*, 126–150, doi:10.1016/j.pocean.2012.11.006.

Comiso, J. C. (2012), Large decadal decline of the Arctic multiyear ice cover, *J. Clim.*, *25*(4), 1176–1193, doi:10.1175/JCLI-D-11-00113.1.

Dee, D. P., et al. (2011), The ERA-Interim reanalysis: Configuration and performance of the data assimilation system, *Q. J. R. Meteorol. Soc.*, *137*(656), 553–597, doi:10.1002/qj.828.

Falk-Petersen, S., H. Hop, W. Budgell, E. N. Hegseth, R. Korsnes, T. B. Løyning, J. B. Ørbæk, T. Kawamura, and K. Shirasawa (2000), Physical and ecological processes in the marginal ice zone of the northern Barents Sea during the summer melt period, *J. Mar. Syst.*, *27*, 131–159, doi:10.1016/S0924-7963(00)00064-6.

Henyey, F. S., J. Wright, and S. M. Flatté (1986), Energy and action flow through the internal wave field: An eikonal approach, *J. Geophys. Res.*, *91*(C7), 8487–8495, doi:10.1029/JC091iC07p08487.

Holm-Hansen, O., and B. Riemann (1978), Chlorophyll a determination: Improvements in methodology, *Oikos*, *30*(3), 438–447.

Ivanov, V. V., I. V. Polyakov, I. A. Dmitrenko, E. Hansen, I. A. Repina, S. A. Kirillov, C. Mauritzen, H. Simmons, and L. A. Timokhov (2009), Seasonal variability in Atlantic Water off Spitsbergen, *Deep Sea Res. Part I*, *56*(1), 1–14, doi:10.1016/j.dsr.2008.07.013.

Johnson, K. S., and L. J. Coletti (2002), In situ ultraviolet spectrophotometry for high resolution and long-term monitoring of nitrate, bromide and bisulfide in the ocean, *Deep Sea Res. Part I*, *49*(7), 1291–1305, doi:10.1016/s0967-0637(02)00020-1.

Johnson, K. S., L. J. Coletti, and F. P. Chavez (2006), Diel nitrate cycles observed with in situ sensors predict monthly and annual new production, *Deep Sea Res., Part I*, *53*(3), 561–573, doi:10.1016/j.dsr.2005.12.004.

Osborn, T. R. (1980), Estimates of the local rate of vertical diffusion from dissipation measurements, *J. Phys. Oceanogr.*, *10*(1), 83–89, doi:10.1175/1520-0485(1980)010<0083:EOTLRO>2.0.CO;2.

Redfield, A. C., B. H. Ketchum, and F. A. Richards (1963), The influence of organisms on the composition of sea-water, in *The Sea*, edited by M. N. Hill, pp. 26–77, Academic Press, New York.

Reigstad, M., C. Wexels Riser, P. Wassmann, and T. Ratkova (2008), Vertical export of particulate organic carbon: Attenuation, composition and loss rates in the northern Barents Sea, *Deep Sea Res. Part II*, *55*(20–21), 2308–2319, doi:10.1016/j.dsr2.2008.05.007.

Sakamoto, C. M., K. S. Johnson, and L. J. Coletti (2009), Improved algorithm for the computation of nitrate concentrations in seawater using an in situ ultraviolet spectrophotometer, *Limnol. Oceanogr. Methods*, *7*, 132–143.

Sambrotto, R., G. Savidge, C. Robinson, P. Boyd, T. Takahasahi, D. Karl, C. Langdon, D. Chipman, J. Marra, and L. Codispoti (1993), Net organic carbon production of marine plankton exceeds estimates based on nitrate limitation, *Nature*, *363*, 248–25.

Schauer, U., E. Fahrbach, S. Osterhus, and G. Rohardt (2004), Arctic warming through the Fram Strait: Oceanic heat transport from 3 years of measurements, *J. Geophys. Res.*, *109*, C06026, doi:10.1029/2003JC001823.

Sundfjord, A., I. Fer, Y. Kasajima, and H. Svendsen (2007), Observations of turbulent mixing and hydrography in the marginal ice zone of the Barents Sea, *J. Geophys. Res.*, *112*, C05008, doi:10.1029/2006JC003524.

Torres-Valdés, S., T. Tsubouchi, S. Bacon, A. C. Naveira-Garabato, R. Sanders, F. A. McLaughlin, B. Petrie, G. Kattner, K. Azetsu-Scott, and T. E. Whitledge (2013), Export of nutrients from the Arctic Ocean, *J. Geophys. Res. Oceans*, *118*, 1625–1644, doi:10.1002/jgrc.20063.

Tremblay, J.-E., K. Simpson, J. Martin, L. Miller, Y. Gratton, D. Barber, and N. M. Price (2008), Vertical stability and the annual dynamics of nutrients and chlorophyll fluorescence in the coastal, southeast Beaufort Sea, *J. Geophys. Res.*, *113*, C07S90, doi:10.1029/2007JC004547.

Vancoppenolle, M., L. Bopp, G. Madec, J. Dunne, T. Ilyina, P. R. Halloran, and N. Steiner (2013), Future Arctic Ocean primary productivity from CMIP5 simulations: Uncertain outcome, but consistent mechanisms, *Global Change Biol.*, *27*, 605–619, doi:10.1002/gbc.20055.

Wijesekera, H., L. Padman, T. Dillon, M. Levine, C. Paulson, and R. Pinkel (1993), The application of internal-wave dissipation models to a region of strong mixing, *J. Phys. Oceanogr.*, *23*(2), 269–286, doi:10.1175/1520-0485(1993)023<0269:taoiwd>2.0.co;2.

III

Randelhoff, A., I. Fer, and A. Sundfjord, Turbulent upper-ocean mixing affected by meltwater layers during Arctic summer, *revised manuscript submitted to Journal of Physical Oceanography*.

REVISED MANUSCRIPT IN REVIEW WITH JPO

Turbulent upper-ocean mixing affected by meltwater layers during Arctic summer

ACHIM RANDELHOFF*
Institute for Arctic and Marine Biology, UiT The Arctic University of Norway, Tromsø, Norway
Norwegian Polar Institute, Tromsø, Norway

ILKER FER
Geophysical Institute, University of Bergen, and Bjerknes Centre for Climate Research, Bergen, Norway

ARILD SUNDFJORD
Norwegian Polar Institute, Tromsø, Norway

ABSTRACT

Every summer, intense sea ice melt around the margins of the Arctic pack ice leads to a stratified surface layer, unlike the traditional surface mixed layers. The associated strengthening of near-surface stratification has important consequences for the redistribution of near-inertial energy, ice-ocean heat fluxes and vertical replenishment of nutrients required for biological growth. We describe the vertical structure of meltwater layers, and quantify their seasonal evolution and their effect on turbulent mixing in the oceanic boundary layer by analyzing more than 450 vertical profiles of velocity microstructure in the seasonal ice zone north of Svalbard. The vertical structure of the density profiles can be summarized by an "equivalent mixed layer depth" h_{BD}, which scales with the depth of the seasonal stratification. As the season progresses and melt rates increase, h_{BD} shoals following a robust pattern, implying stronger vertical stratification, weaker vertical eddy diffusivity, and reduced vertical extent of the mixing layer which is bounded by h_{BD}. Through most of the seasonal pycnocline, the vertical eddy diffusivity scales inversely with buoyancy frequency ($K_\rho \propto N^{-1}$). The presence of mobile sea ice alters the magnitude and vertical structure of turbulent mixing primarily through stronger and shallower stratification, and thus vertical eddy diffusivity is greatly reduced under sea ice. We use these results to develop a quantitative model of surface layer turbulent mixing during Arctic summer, and discuss the impacts of a changing sea ice cover.

1. Introduction

Stratification, currents, turbulence levels and vertical mixing in the upper Arctic Ocean are coupled to and affected by the presence of sea ice. The sea ice cover can act like a lid to prevent input of energy from the atmosphere (Levine et al. 1985; Morison et al. 1985), and enhance or reduce the near-surface mixing (Martin et al. 2014) by changing the air-ice drag. During summer, when broken-up floes drift relatively freely, sea ice melt increases stratification as this freshwater accumulates in the upper tens of meters of the water column (Proshutinsky et al. 2009; Peralta-Ferriz and Woodgate 2015). In these conditions, the "classic" definition of a surface mixed layer overlying a distinct pycnocline is not applicable. Instead, the upper water column down to several tens of meters is stratified, and becomes part of the seasonal pycnocline (McPhee et al. 1987; Randelhoff et al. 2014). We refer to this phenomenon as "meltwater layer" or "freshwater layer". The meltwater layer can include, but should not be confused with, the thin, isolated freshwater lenses caught between under-ice ridges. Spatial variability in ice conditions, melt rates and turbulent mixing can set up lateral density gradients over rather short distances (Timmermans and Winsor 2013). Horizontal stirring might therefore also play a role in the evolution of freshwater layers. In winter, brine rejection and intense vertical winter mixing can homogenize the upper ocean and lead to deep mixed layers before the onset of melt. This is particularly true in the weakly stratified Atlantic sector (Rudels 2016) which is where the data to be used in our study have been collected. While some remnant of previous meltwater stratification may be present in the Pacific sector, our data are characterized by starting from zero mixed layer stratification each spring.

Climate models predict both decreased summer sea ice extent in the Arctic, and increased summer melt rates (Stroeve et al. 2012), leading to stronger stratification. This might increase the heat retained in the ocean, and

---

Corresponding author address: Achim Randelhoff, Institute for Arctic and Marine Biology, UiT The Arctic University of Norway, Tromsø, Norway.
E-mail: achim@npolar.no

therefore shift the partitioning between solar heat directly contributing to ice melt, and heat penetrating the ice cover and warming the water column (e.g. Hudson et al. 2013; Granskog et al. 2015). Furthermore, the predicted acceleration of the hydrological cycle and decadal changes in wind-driven circulation leads to a changing freshwater content of the upper Arctic Ocean (e.g. Morison et al. 2012; Haine et al. 2015). A recurrent theme also in the discussion of the fate of Arctic Ocean ecosystems is "Arctic Freshening", which is hypothesized to affect primary production and ecosystem composition (e.g. Li et al. 2009). We thus differentiate between two modes of freshening: a climatic one due to changes in the hydrological cycle which freshens the Polar Mixed Layer, and a seasonal one due to sea ice melt which increases stratification in the turbulent ice-ocean boundary layer. It is the latter of these two modes that this study is concerned with.

Meltwater layers affect turbulent mixing in the upper ocean in multiple ways. The upper turbulent boundary layer can act as a sink for energy delivered from wind; the fraction of the energy that is not dissipated in the boundary layer is redistributed or radiated to deeper parts of the water column. Thus, meltwater layers may play an important role in altering the downward-propagating near-inertial energy (Morison et al. 1985). When mixed layer stratification is sufficiently shallow, it can interact with sea ice drift to generate additional ice-ocean drag mediated by internal waves (McPhee and Kantha 1989).

Turbulence levels in the water column are typically gauged by the dissipation rate, ε of turbulent kinetic energy, which can be directly measured by, for example, microstructure profilers. Quantification of the dissipation rate, either by observations or through its scaling and parameterization using external forcing parameters is crucial to describe the evolution of hydrography, currents, and turbulent fluxes of heat, salinity, nutrients and momentum in the water column. The sensitivity of the overall energy budget in the upper Arctic water column to stratification and the fresh water content is still unknown.

While the research community working in the polar regions certainly is aware of the significance of these meltwater layers, we have found that their vertical structure and effect on turbulent mixing have received little attention, possibly related to the scarcity of direct turbulence observations in this environment. In the present study, we present a detailed analysis of direct observations of hydrography and turbulent microstructure in the upper ocean during Arctic summer.

We aim to characterize the vertical distribution of meltwater in the IOBL and how this affects the turbulent mixing in the upper ocean by setting up a predictive framework. To this end, we formulate three objectives: (1) Develop a framework to describe the hydrography and vertical structure of freshwater layers by identifying key variables and how they relate to each other, (2) describe the temporal evolution of key variables on seasonal and subseasonal (e.g., weekly) time scales, and (3) quantify how these key variables relate to turbulent mixing. Each of these three objectives will be treated in their own sections. Concepts and salient explanations describing the vertical stratification and turbulence interactions exist. We aim to advance this knowledge by contributing toward a predictive understanding. Synthesizing Objectives 1 to 3, we develop a quantitative model of upper ocean mixing during the Arctic summer and how it might change in a future climate.

2. Data

a. Data sets

The field data used in this study were collected during four campaigns, all of them in the area around Fram Strait, the Yermak Plateau and the Nansen Basin (Fig. 1) in the Seasonal Ice Zone (SIZ) and the Marginal Ice Zone (MIZ). The SIZ is defined as the region between maximum and minimum sea ice extent in late spring and late summer, respectively. The MIZ is the transition region from pack ice to open water. Two cruises of the Carbonbridge project (May and August 2014) were conducted in the MIZ. Data were sampled on these cruises in a broken-up ice cover with small, rough ice floes (concentrations 25–90%) and open water, as is typical of the MIZ. The other two campaigns included longer stations drifting with ice floes in a near-100% ice cover. The N-ICE2015 drift stations lasted from January through June 2015 (Granskog et al. 2016), including a total of four different ice floes. For this study, the focus is on the N-ICE2015 profiles measured after 25 May 2015, when upper ocean turbulence was affected by sea ice meltwater, that is from Floe 3 (lasting until 6 June) and Floe 4 (6–18 June). For N-ICE2015, the ice concentration was only occasionally as low as 85% (towards the ends of Floe 3 and 4). The other ice drift camp included in this study is the one-week ICE-2012 drift station in late July 2012 (for a description of the ice-ocean interaction, see Randelhoff et al. (2014); see also Hudson et al. (2013)).

In all campaigns, we used the MSS-90L drop sonde (IWS Wassermesstechnik) with two airfoil shear probes to measure turbulent microstructure along with temperature and conductivity in the upper 100-300 meters. Note that while the conductivity sensors were regularly calibrated by the manufacturer, no calibration was performed using field data from bottle samples or other conductivity profiles. Profiles of salinity and accordingly density may therefore exhibit slight (depth-independent) offsets between individual campaigns. However, as will be shown later, these potential offsets have no bearing on the quantities derived from single density profiles as all are referenced to a fixed depth interval.

In total, we use 375 microstructure profiles sampled under ice-covered conditions that exhibit a discernible amount of meltwater as defined by the density difference between surface and a deeper level (the precise definition is given in Section. 3.a). These are contrasted with 82 microstructure profiles sampled in open water, similarly exhibiting surface accumulation of meltwater, and 80 profiles sampled during the N-ICE2015 campaign in January and February in the Nansen Basin, when a deep (>60 m) winter mixed layer prevailed. These open-water and winter profiles are only used where explicitly stated. In addition, in order to compare the summer and winter hydrographies also in the shelf slope area, we also include some CTD profiles from a Carbonbridge cruise in January 2014, but note that no microstructure sampling was conducted on that cruise.

During the N-ICE2015 and ICE-2012 drift stations, the vessel was moored to an ice floe and the MSS was generally deployed several 100 m from the ship. The Carbonbridge cruises were vessel-based with frequent 24-hr process stations which permitted sampling from ice floes 100-200 m from the ship. Note that open-water stations and some ice covered transect stations were only sampled from the vessel (all during Carbonbridge), which limited data resolution and quality, especially of turbulent microstructure, in the upper ∼10–15 m of the water column.

b. MSS data processing

MSS data were processed following Fer (2006). Assuming local small-scale isotropy (Yamazaki and Osborn 1990), dissipation of turbulent kinetic energy was estimated from the measured microscale shear as $\varepsilon = 7.5\nu\langle(\partial_z u')^2\rangle$, where ν is the molecular viscosity of sea water and $\partial_z u'$ the turbulent shear. In practice, the portion of the shear wavenumber spectrum unaffected by high-frequency noise is integrated, and the unresolved variance is accounted for by using an empirical spectrum. Eddy diffusivity of mass is estimated from a balance stroke between the shear production, buoyancy flux and the dissipation rate, and assuming a constant mixing efficiency factor corresponding to $\Gamma = 0.2$ (see Section 5 a), using $K_\rho = 0.2\frac{\varepsilon}{N^2}$ (Osborn 1980). The buoyancy frequency, N, is calculated as $N^2 = \frac{\partial b}{\partial z}$ with the buoyancy $b = -\frac{g}{\rho}\sigma_\theta$, where g is the gravitational acceleration and ρ the potential density of sea water. The Osborn model cannot be used in well-mixed layers where $N^2 \approx 0$; however, our data set is characterized by significant stratification (above the measurement noise level) in the entire sampled water column, including the surface layer.

c. Wind speed and wind work

Wind speed U_w is measured at 10 m from on-ice weather masts or at 24 m from the respective ship's weather mast, and adjusted to 10 m as described below. In order to (a) make our work applicable to different ice types or even open water and (b) give a sense of the energy transfers involved, we phrase the analysis in terms of the wind work as opposed to wind speed or ice-ocean interface stress.

Following Dewey and Moum (1990), wind work at 10 m is defined as the dot product of wind velocity and (directional) wind stress: $E_{10} = \mathbf{U_w} \cdot \tau \propto C_a \rho_a U_w^3$, where C_a is the 10-m air-ice drag coefficient and ρ_a is the density of air. The input of turbulent energy into the ocean through the surface is then defined as $E_0 = \rho {u_*}^3 = (C_a\rho_a/\rho)^{1/2}E_{10}$ (following Denman and Miyake 1973), about 0.15 % of E_{10}.

The value of C_a varies with type of ice cover, ice concentration and floe size (Anderson 1987; Guest and Davidson 1987). For N-ICE2015 and ICE-2012, which took place in a similar floe size distribution, we use a value of $\approx 2.1 \cdot 10^{-3}$ (determined from average 10-m wind speed and air-ice momentum flux during the summer period of N-ICE2015), and for Carbonbridge, which took place closer to the ice edge and with a larger fraction of smaller floes and open water, we use $C_a = 4 \cdot 10^{-3}$ based on the characterization of the 2.1–5.3$\cdot 10^{-3}$ range given by Anderson (1987) and Guest and Davidson (1987) for the MIZ.

We used the Law of the Wall to adjust wind speed observations at the respective vessel's wind sensors (approximately 24 m height) to 10 m following the formula $U_{10} = U_{24}\frac{\log(10\ \mathrm{m}/z_0)}{\log(24\ \mathrm{m}/z_0)}$, where the roughness length z_0 can be calculated from the 10-m drag coefficient as $z_0 = \exp(-0.4/\sqrt{C_a}) \cdot 10$ m.

d. Near-inertial energy in the upper ocean

Upper-ocean near-inertial energy was determined for the N-ICE2015 drift campaign using complex demodulation from GPS fixes of R/V Lance. Under-ice currents were analyzed in a similar fashion, and approximate agreement between the semidiurnal clockwise components were found, indicating that ice drift and upper ocean currents were tightly coupled. The amplitude of the clockwise semidiurnal component of ice drift velocity was therefore computed as a measure of the strength of near-inertial oscillations in the upper ocean.

e. Melt rates and surface buoyancy fluxes

For N-ICE2015, the overall surface buoyancy flux $\langle w'b'\rangle_0$ was estimated from ice mass balance buoys in the period until 06 June 2015 (Itkin et al. 2015) and from hotwire arrays after that when a new ice floe was occupied (see A. Rösel et al., Winter and spring development of sea-ice and snow thickness distributions north of Svalbard observed during N-ICE2015, in revision for Journal of Geophysical Research). For ICE2012, we used $\langle w'b'\rangle_0$

as calculated by Randelhoff et al. (2014) based on measurements of the turbulent ice-ocean flux, and validated by comparison with ice mass balance. For Carbonbridge, no such data are available. Stipulating an ice salinity of around 5, we converted the melt rate $\dot{h}$ [cm d^{-1}] into the surface buoyancy flux by $\langle w'b' \rangle_0 = \dot{h} \cdot 2.4 \cdot 10^{-8}\ \frac{\text{W d}}{\text{kg cm}}$, where the numerical factor is the product of ice-ocean salinity difference, ratio of ice and ocean densities, gravitational acceleration, haline contraction coefficient of seawater and the cm-m and day-second conversion factors.

3. Objective 1: A framework for the hydrography of meltwater layers in the oceanic turbulent boundary layer

In the following we present a framework to efficiently describe types of meltwater layers. This involves identification of key variables, their relations to each other and methods to reconstruct the full density profile from them. Campaign-averaged density profiles show the seasonal progression from May (Carbonbridge) through June (N-ICE2015), July (ICE-2012) and August (also Carbonbridge) (Fig. 2 A).

a. Vertical structure

The typical summer hydrographic conditions in the seasonal ice zone do not show a surface mixed layer overlying a well-defined pycnocline. Instead, the entire upper tens of meters of the water column become seasonally stratified. It is therefore crucial to distinguish between definitions that describe various portions of the upper ocean. The "surface mixed layer" is classically defined as that part of the upper ocean which is well-mixed with respect to physical tracers such as salinity or temperature. It is often delineated by a critical density, where the bottom of the mixed layer is defined as the shallowest depth at which density exceeds a critical density difference, relative to the surface density. Most of the profiles included in our study do not have such a surface mixed layer. Some of them might; but in order to find a framework that suits all of the profiles, we will define a "surface layer" instead (see below). In profiles comprising a well-mixed layer above a distinct pycnocline, the surface layer is equivalent to the surface mixed layer, but not in general. The surface layer is not to be confused with the "ice-ocean (turbulent) boundary layer", which is that part of the upper ocean where the turbulent flow is significantly affected by the shear driven mixing that the relative motion of ice floes and water generates.

We will employ an instrumental definition of the terms "surface layer", "pycnocline" and "deep" water column, where the three are delineated depending on their upper density relative to a deep reference density. The "upper density" $\sigma_{\theta 0}$ is defined as the average σ_θ over the interval 3–5 m. Based on the visual inspection of all collected density profiles, we stipulate that density stratification is well within background values by approximately 50 m depth (Fig. 2, Panels A and B). Accordingly, we define the "deep" density $\sigma_{\theta d}$ as the average over the interval 45–55 m. Their difference defines the "surface density deviation" $\Delta\sigma_\theta = \sigma_{\theta d} - \sigma_{\theta 0}$. A profile is categorized as "discernibly" affected by meltwater if $\Delta\sigma_\theta > 0.02$ kg m^{-3}. The choice of the reference depth 45–55 m is ad-hoc; however, our results are not particularly sensitive to this choice: A 10 m deeper reference depth results in an average increase of $\Delta\sigma_\theta$ by only 0.04 kg m^{-3}, and of the buoyancy deficit BD (defined below) by 2 kg m^{-2}. Our choice of reference depth is motivated by a level located in a region of weak stratification, well below the depth range that is immediately affected by seasonal accumulation of meltwater. The results will then be robust against the arbitrary choice of the reference depth.

Based on these notions, we define a scaled depth coordinate $r_\sigma(z) = (\sigma_\theta(z) - \sigma_{\theta 0})/\Delta\sigma_\theta$, which runs from 0 to 1 (values exceeding this interval are set to 0 or 1, respectively). The surface layer (SL) is defined as the depth range where $0 \le r_\sigma < 0.2$, the pycnocline (PC) as the depth range where $0.2 \le r_\sigma \le 0.8$, and the "deep" water column comprises $0.8 < r_\sigma$ and deeper. The upper and lower extents of the pycnocline (PC) thus correspond to the depths where the density crosses 20 and 80% of the density difference $\Delta\sigma_\theta$ between the upper and deep reference depths, respectively. In this study, the terms SL, PC and "deep" follow this definition, except where stated otherwise. It has previously been demonstrated that shear in the turbulent boundary layer is mostly located in the shallow seasonal pycnocline (e.g. Randelhoff et al. 2014), such that the interval r_σ=[0,1] meaningfully covers the depth range where the transition between the turbulent regimes (ice-ocean and underlying ocean) takes place. The choices $r_\sigma = 0.2,\ 0.8$ are ad hoc; however, $r_\sigma = 0.2$ as the boundary between SL and PC will be justified post-hoc (in our treatment of Objective 3) as the boundary between where dissipation is dominated by wind versus background stratification. The choice of $r_\sigma = 0.8$ can be changed within $\pm \sim 0.1$ without any significant effect on the analysis, but this distinction is not crucial for us. It is important, however, that the PC encompasses the depth range where we expect the transition between ice drift (shear) driven turbulence and predominantly internal-wave driven turbulence to happen. Our choice is motivated by Randelhoff et al. (2014)'s observations that ice-ocean shear was located in this depth range.

b. Interpreting density profiles using key variables

We define the "buoyancy deficit" BD as $\int_{0\text{ m}}^{50\text{ m}} \mathrm{d}z(\sigma_{\theta d} - \sigma_\theta(z))$. It combines the effect of surface freshening and warming, but due to low temperatures and accordingly weak thermal expansion, and large fractions of freshwater, it is almost proportional to the freshwater content $\int \mathrm{d}z(S_d - S(z))$, where S_d is the "deep" salinity defined analogously to $\sigma_{\theta d}$. An "equivalent mixed layer depth" is defined as $h_{\mathrm{BD}} = \mathrm{BD}/\Delta\sigma_\theta$. Whenever the SL is well-mixed and the pycnocline is sufficiently sharp, h_{BD} corresponds to the mixed-layer depth in the classical sense. When h_{BD} is larger, more of the freshwater is accumulated in the SL as opposed to the PC, relatively speaking. h_{BD} can therefore be thought of as the mixed-layer depth if the same BD were redistributed to achieve an unstratified SL, keeping $\Delta\sigma_\theta$ intact (Fig. 2 C). For the same BD, small h_{BD} means that the meltwater is accumulated in the PC and larger h_{BD} means that the meltwater is distributed more evenly with depth. It is also helpful to keep in mind that by definition, h_{BD} is at least 0 m and at most equal to the reference depth (in this case, 50 m).

c. *Observed parameter ranges*

Pooling all the summer profiles with a sufficient amount of meltwater accumulation in the upper tens of meters ($\Delta\sigma_\theta > 0.02$ kg m^{-3} as discussed above), we observed the following parameter ranges (given as median values, with 5% and 95% quantiles in brackets): BD=19 (7, 40) kg m^{-2}, h_{BD}=20 (14, 29) m, E_0=12 (0.4, 77)$\cdot 10^{-4}$ kg s^{-3} (corresponding to wind speeds of 5.6 (2.1, 11.4) m s^{-1}). BD and h_{BD} were not correlated on a survey basis, but a seasonality in $\Delta\sigma_\theta$ leads to a remarkable proportionality when grouped by campaign, i.e. by area and time (Fig. 3). This latter relation will be explored in more detail in Objective 2.

Surface buoyancy fluxes were in the range $4\cdot 10^{-9}$–$4\cdot 10^{-7}$ W kg^{-1}; fluxes larger than 10^{-7} W kg^{-1} were associated with rapidly disintegrating ice floes over the inflowing Atlantic water (melt rates O(10 cm d^{-1})), whereas more "typical" melt rates (O(1 cm d^{-1})) entailed $\langle w'b'\rangle$ below $3\cdot 10^{-8}$ W kg^{-1} (see also A. K. Peterson et al., Turbulent Heat and Momentum Fluxes in the Upper Ocean Under Arctic Sea Ice, in revision for Journal of Geophysical Research). Shallower h_{BD} was associated with larger $\langle w'b'\rangle_0$ or sampling later in the melt season (Fig. 3 C).

d. *A predictive model of the vertical density structure and stratification*

In a qualitative sense, the vertical density profiles are largely consistent with the general notion that larger amounts of freshwater (i.e., BD) and larger top to deep density differences (i.e., $\Delta\sigma_\theta$) mean stronger overall stratification, while smaller equivalent mixed layer depths (i.e., h_{BD}) mean that the freshwater is accumulated at shallower depths. However, we are interested in *quantitative* models of the vertical density structure as a function of these easily accessible parameters, ultimately in order to predict the structure of vertical mixing (see Objective 3). The method must be generally applicable to vertical stratification profiles, independent of the presence of a mixed layer. Therefore we have developed a framework that allows computation of the vertical structure from the bulk parameters BD and the "equivalent mixed layer depth" h_{BD}.

BD is an easily accessible parameter that is strongly related to the total amount of melt that has happened until the time of sampling. Instead of h_{BD}, one could use $\Delta\sigma_\theta$ as a predictive parameter, as only two of out of BD, h_{BD} and $\Delta\sigma_\theta$ are independent. We chose h_{BD} for the following reasons. h_{BD} was found to be well-correlated with depths where the scaled density coordinate r_σ has specific values (Fig. 4; slopes are close to 1:1). This supports the notion that h_{BD} aptly summarizes the vertical structure of the density profiles. We will also show later (see Objective 3) that h_{BD} not only determines the hydrographic structure, but it is also an indicator of the vertical extent of turbulent mixing, that is the depth from which wind-driven mixing can entrain deeper water into SL, the surface layer.

To determine the relationships between these selected key parameters and vertical profiles of density and turbulent mixing, we employ linear regression models (Fig. 5). For Objective 1, we focus on Panels A-F of Fig. 5, which treat the dependence of the vertical density structure (r_σ and σ_θ) and the vertical stability (N^2) on BD and h_{BD} (Panels G-N are deferred to the treatment of Objective 3). The regressions are performed separately for each depth bin, where depth is binned according to either vertical distance from surface z (B,E) or the density-scaled r_σ coordinate (C,F). The middle and right columns in Fig. 5 thus show how the vertical structure of the quantity in the left column changes as a function of the variable in question (see legends). The vertical coordinate is isobaric, the distance from surface, z, in the middle column, and based on the scaled depth r_σ in the right column. The use of z that extends to 75 m allows to resolve the SL-PC continuum as well as the structure below the deep reference of 50 m where r_σ=1.

For example, in panel C, we fit a linear model of the form $\sigma_\theta = a + b\cdot\mathrm{BD} + c\cdot h_{\mathrm{BD}}$ to all the (σ_θ, BD, h_{BD}) data points in each specific r_σ interval. We then refer e.g. to b as the "sensitivity of σ_θ to BD" and so forth. Panel C shows that in the surface bin, σ_θ is reduced by approximately -0.05 kg m^{-3} per BD increase of 1 kg m^{-2}, i.e. "the sensitivity of surface σ_θ to BD is -0.05 (kg m^{-3})/(kg m^{-2})".

Panels A and D show average profiles of r_σ and N, respectively, binned according to BD and h_{BD} associated with each profile. The remaining panels (B,C,E,F) show regression results, where BD and h_{BD} are the predictor variables and either σ_θ (B,C) or $\log_{10}N^2$ (E,F) is the response variable.

σ_θ, N^2 and r_σ all exhibit well-defined responses to h_{BD} and BD. Interestingly, the vertical structure of the density profiles (as given by r_σ and N^2) did not depend on the total amount of meltwater, i.e. BD (A, F). Increasing amounts of freshwater were accumulated mostly in the upper 30 m (B,E).

e. Summary for Objective 1

Density profiles of the upper water column comprising freshwater layers are characterized by h_{BD}, BD and $\Delta\sigma_\theta$, any two of which are independent and determine the third by the defining relationship $h_{\mathrm{BD}} \equiv \mathrm{BD}/\Delta\sigma_\theta$. Large accumulations of meltwater entail large BD, whereas high h_{BD} values indicate relatively deep pycnoclines and weakly stratified surface layers. Changes in the BD and h_{BD} values associated with a particular profile are tightly connected to changes in the density structure of that profile; the shape of the r_σ profile is largely determined by h_{BD}, revealing a certain amount of generality across all density profiles in our data set.

4. Objective 2: Seasonal evolution and asymptotic states of freshwater layers in the IOBL

In Fig. 3, two features emerged: The relatively narrow $\Delta\sigma_\theta$ range that was observed during each of the campaigns, and the narrowing range of observed h_{BD} values as the melt season progresses and BD increases.

In the following, we argue that neither of these features is a coincidence. However, while convergence to specific h_{BD} values can in fact be explained as the asymptote of a simple evolution equation, the apparent convergence to relatively narrow ranges of $\Delta\sigma_\theta$ requires more elaboration.

a. Seasonal evolution towards asymptotic h_{BD}

As will be shown below in our discussion of Objective 3, h_{BD} plays an important role in regulating the maximum vertical extent of wind-driven mixing. This warrants an attempt to understand its seasonal dynamics. From the definition of h_{BD}, we can derive a simple expression for its temporal evolution:

$$\partial_t h_{\mathrm{BD}} = \partial_t \left(\frac{\mathrm{BD}}{\Delta\sigma_\theta} \right) = \frac{1}{\Delta\sigma_\theta} \left(\partial_t \mathrm{BD} - h_{\mathrm{BD}} \partial_t \Delta\sigma_\theta \right). \quad (1)$$

Now the problem is reduced to specifying how BD and $\Delta\sigma_\theta$ evolve. The former is straightforward and follows from integrating the melt rate. The temporal evolution of $\Delta\sigma_\theta$ is governed by the divergence of the buoyancy flux through a small control volume of thickness z^* (e.g., 2 m such that it could cover the 3–5 m depth interval used to calculate the upper density $\sigma_{\theta 0}$ in this study) at the ice-ocean interface. The flux leaving this control volume upwards is simply the melt rate $\langle w'b' \rangle_0$. The flux entering the control volume at a distance z^* from the ice-ocean interface is denoted by $\langle w'b' \rangle_{z^*}$. The rate of change of $\Delta\sigma_\theta$ is then the result of a simple budget,

$$\partial_t \Delta\sigma_\theta = \frac{\rho_w}{g} \left(\langle w'b' \rangle_0 - \langle w'b' \rangle_{z^*} \right) / z^*. \quad (2)$$

Both $\partial_t \mathrm{BD} \propto \langle w'b' \rangle_0$ and $\partial_t \Delta\sigma_\theta$ are positive through the season, as BD and $\Delta\sigma_\theta$ both increase as the melt season progresses (Fig. 3). Under these conditions, the asymptote of the exponential evolution equation Eq. 1 is well-defined:

$$h_{\mathrm{BD}}^{\infty} = \frac{\partial_t \mathrm{BD}}{\partial_t \Delta\sigma_\theta} = z^* \frac{\langle w'b' \rangle_0}{\langle w'b' \rangle_0 - \langle w'b' \rangle_{z^*}}, \quad (3)$$

where the last equality follows from inserting Eq. (2). From Eq. 3, we can see that increasing $\langle w'b' \rangle_0$ means decreasing h_{BD}^{∞} as $\langle w'b' \rangle_{z^*}$ is not strongly dependent on the melt rate. The time scale for the exponential convergence is $\Delta\sigma_\theta / \partial_t \Delta\sigma_\theta$. Later in the melt season, this time scale can be several weeks (based on an increase from $\Delta\sigma_\theta \approx 1.2$ to 1.4 kg m^{-2} during the 1 week drift of ICE-2012). However, early in the season, when $\Delta\sigma_\theta$ is small, this convergence is fast (days), such that we can stipulate that the actual h_{BD} is close to h_{BD}^{∞} as long as no abrupt, big changes in melt rates or turbulent mixing have occurred. The shoaling and narrowing of the observed range of h_{BD} values is thus a consequence of Eq. (3), where increasing melt rates only allow for smaller ranges of h_{BD} values.

b. Ice-ocean interface buoyancy flux and the regional convergence of $\Delta\sigma_\theta$

Higher melt rates should entail both shallower stratification and larger accumulations of meltwater (i.e., $h_{\mathrm{BD}} \sim 1/\mathrm{BD}$). However, Fig. 3 A suggests that for each of the data "clouds" (each of which are, on a per-campaign-basis, geographically well-separated and hydrographically diverse; not shown), shallower stratification actually coincides with smaller amounts of freshwater (i.e., $h_{\mathrm{BD}} \sim \mathrm{BD}$). One might imagine that this is part of a feedback mechanism whereby higher melt rates introduce more meltwater and increase shallow stratification, thereby reducing the melt rate (see e.g. Randelhoff et al. 2014). However, this would likely lead to a convergence to common (regional) melt rates rather than a common $\Delta\sigma_\theta$ value (Fig. 3 B). Indeed, it seems to be a combination of the melt rate and the total duration of the melt that drove the evolution of $\Delta\sigma_\theta$ in our data set (Fig. 3 C). We propose instead that lateral mixing might explain the observed parameter behaviour ($h_{\mathrm{BD}} \sim \mathrm{BD}$).

Gravitational slumping of fronts (i.e. gravitational flattening of isopycnals), where the heavier water slides underneath the lighter water, has been observed in the Arctic Ocean both in winter under sea ice (Timmermans et al. 2012) and in meltwater induced fronts in the Chukchi Sea (Timmermans and Winsor 2013). For our data set, slumping alone cannot explain the apparent discrepancy between the $h_{\mathrm{BD}} \sim$ BD distribution observed in the field and the $h_{\mathrm{BD}} \sim 1/\mathrm{BD}$ distribution conjectured based on 1-dimensional boundary layer physics as detailed above. However, slumping combined with the observed, vertically rapidly attenuated diapycnal mixing could produce a vertical structure of lateral mixing sufficient for explaining the observations (Fig. 6). This mechanism would mix the stratified upper surface waters more strongly than waters at depths of few tens of meters, and thus the result would be two density profiles that have similar $\Delta\sigma_\theta$, but varying BD (lower panels in Fig. 6).

c. Summary for Objective 2

We found clear patterns in the temporal evolution of density profiles in h_{BD}-BD-$\Delta\sigma_\theta$ parameter space. Our results indicate that profiles from a certain region and time of the year exhibit very similar upper densities ($\sigma_{\theta 0}$), which hints at the importance of lateral mixing processes. As the melting season progresses, the surface layer becomes lighter and stratification (that is, the equivalent mixed layer depth h_{BD}) shoals and becomes less variable. Consistent with observations, h_{BD} is conjectured to converge to a constant value set by ice melt and ice-ocean interface turbulence.

5. Objective 3: Vertical mixing

The previous sections suggest that the evolution of sea ice meltwater layers is governed by robust patterns, many of which can be quantified. What is still missing in order to assess the role they play in shaping the current and future Arctic, is how these meltwater layers affect the vertical extent and intensity of turbulent mixing.

a. Mixing parameters

A mixing layer depth h_ε is defined as the depth to which active turbulence mixing induced by surface processes reaches (Brainerd and Gregg 1995), inducing buoyancy flux through entrainment. h_ε is distinct from, and can be shallower or deeper than the mixed layer depth (which we have not defined or used in this study). Dissipation rate profiles can be used to estimate h_ε. Here we define h_ε as the shallowest depth where the 5-m smoothed dissipation rate drops below $5{\cdot}10^{-9}$ W kg^{-1}. The dissipation threshold must be several orders of magnitude less than the energetic upper layer, and close to the deep background values (e.g., Fig. 5 I). The values of h_ε are not sensitive to the exact choice of the threshold, since the dissipation rate decays rapidly with depth from the turbulent surface layer.

Regarding the intensity of the turbulent mixing, several quantities are of interest. The rate of dissipation of turbulent kinetic energy is measured by vertical microstructure profilers recording small scale shear; it has units of W kg$^{-1} \equiv$ m^2 s^{-3}. As such, it describes turbulence in an energetic sense since its vertical integral over the mixing layer approximately balances the turbulent kinetic energy supplied through the surface layer and expended on the upward buoyancy flux. The vertical mixing of tracers, on the other hand, is described by the eddy diffusivity K_ρ, frequently parameterized as $K_\rho = \Gamma\frac{\varepsilon}{N^2}$ (Osborn 1980). While the magnitude of the coefficient Γ depends on multiple parameters, in this study we use the canonical value of 0.2 that has been found to be appropriate for long-term averages in stratified regions (Osborn 1980; Moum 1996). Also note that Sundfjord et al. (2007) provided support for this value for diffusively stable conditions in their data from the MIZ of the Barents Sea. Given an unchanged background E_0 and Γ, the relative changes in K_ρ are mostly governed by the dependency of ε on N^2, which is governed by BD and h_{BD} (see Objective 1), which in turn are governed by robust seasonal patterns (see Objective 2). With this in mind, we now turn our attention to the effect of meltwater layers on upper-ocean turbulent mixing.

b. Scaling of dissipation rate and diffusivity

Panels A and B of Fig. 7 show dissipation in the SL, the PC and "deep" layer as a function of in-situ buoyancy frequency and wind forcing. In the SL, ε was significantly elevated above deep ε, decreased with increasing N^2 and increased with increasing E_0. The observations are typical of earlier studies, and are intuitive. The decrease in ε with increasing N^2 still holds when looking at specific fixed-depth intervals (not shown). In the PC, dissipation levels were drastically reduced from SL values, but remained slightly higher than "deep" dissipation values. Increasing E_0 led to the steepest increase in ε in the SL, and was negligible below the PC.

Deep surface mixed layers and mixing depths in excess of 60 m were observed (Fig. 8 A) during neutral or slightly unstable stratification in the N-ICE2015 January data. For strong wind forcing, h_ε during shallow stratification was reduced by several tens of meters relative to the deep mixed layers. Across both meltwater layers and deep mixed layers, h_ε increased with higher wind speeds as expected. The profiles with a meltwater layer, however, show no significant change in the dependency of h_ε on E_0 for changes in BD and h_{BD} (Fig. 8 A). Indeed, h_{BD} was limiting for h_ε only in cases of strong wind; during times of low E_0, h_ε was, on average, half the value of h_{BD} (Fig. 8 B).

We now extend the depth-binned linear regression analysis from Objective 1 (Section 3) to turbulence parameters, displayed in Fig 5, Panels G-N. Briefly, for each depth bin, we determined the regression slopes of the response variable ($\log_{10} N^2$, $\log_{10}\varepsilon$ or $\log_{10} K_\rho$) as a linear function of one or two predictor variables. In the following, "sensitivity" refers to this slope, but to avoid cluttering the description, log-transformations may be implied (e.g., sensitivity of ε will refer to that of $\log_{10}\varepsilon$). See the figure caption of Fig. 5 for the exact definitions of the regression equations.

Instantaneous wind work had the largest effect on ε (as scaled by the ranges of the predictor variables) in the surface and down to $r_\sigma \approx 0.3$, reaching zero at $r_\sigma \approx 1$, or $z \approx 35$ m (J,K). This is not to say that wind energy generally did not penetrate below this depth, but the instantaneous surface wind was not coherent with ε below that level anymore. Sensitivity of ε to N^2 was around zero, at most slightly negative, in the surface, reaching a constant $\varepsilon \propto \left(N^2\right)^{0.5}$ exponent from r_σ=0.3 and deeper (J,K).

BD and h_{BD} affected K_ρ down to r_σ=0.5 or about 30 m. K_ρ increased with increasing h_{BD} and slightly with decreasing BD (M,N). BD had its largest effect in the PC (N), where it increased stratification (F). Increasing h_{BD} was related to weakening surface layer stratification (F) which is connected to higher E_0 values (G). As a reality check of this sensitivity approach, we can also estimate $\frac{\partial \log_{10} K_\rho}{\partial \mathrm{BD}} \approx \left(\frac{\partial \log_{10}\varepsilon}{\partial \log_{10} N^2} - 1\right) \frac{\partial \log_{10} N^2}{\partial \mathrm{BD}}$ (and analogously for h_{BD}). The approximate equality stems from the fact that $\frac{\partial \log_{10}\varepsilon}{\partial \mathrm{BD}} \approx \frac{\partial \log_{10}\varepsilon}{\partial \log_{10} N^2} \cdot \frac{\partial \log_{10} N^2}{\partial \mathrm{BD}}$, neglecting implicit dependencies other than that on the dominant factor N^2. $\frac{\partial \log_{10}\varepsilon}{\partial \log_{10} N^2}$ is then taken from Panel J and $\frac{\partial \log_{10} N^2}{\partial \mathrm{BD}}$ etc. from Panel E. The patterns and magnitudes in the resulting sensitivity estimates are remarkably similar (Fig. 5 M) when considering that the above approximation neglects the wind speed, which likely leads to some residual (nonlinear) effects due to its correlation with upper-ocean stratification (Fig. 5 G).

c. Effects of presence or absence of ice cover

Sea ice can affect turbulent mixing in the ice-ocean turbulent boundary layer in two ways: (1) Directly altering air-sea interaction, by e.g. changing air-sea into air-ice drag, suppressing surface gravity waves, breaking of surface waves, inhibiting Langmuir circulation, etc., and (2) changing the under-ice stratification by acting as a strong buoyancy source (ice melt). Since the effects of (2) are easily quantifiable in the BD-h_{BD} framework, we seek to isolate issue (1) and compare vertical profiles of dissipation with and without ice cover.

Based on our previous discussion, we suspect the largest changes in the vertical structure of dissipation are linked to variations in h_{BD} and BD. However, h_{BD}, BD and E_0 all cover a similar range of values and do not seem to be related to systematic changes in the relative structure of ε(z) between open-water and ice covered conditions. Stations over the shelf frequently exhibited other mixing processes like tidal and frontal mixing, possibly in connection with the shallow topography, leading to interleaving and complicated vertical structures in dissipation profiles that we are confident do not reflect surface driven mixing (not shown). (Note, however, that these additional processes mostly affected the open-water stations since the ice-covered stations were mostly located off-shelf.) Thus considering only profiles at bottom depths of >500 m, this leaves us with 30 profiles under open-water and 170 profiles under ice covered conditions. Neither mean (maximum likelihood estimates using a lognormal estimator) nor median dissipation profiles show any significant deviation between the presence and absence of ice cover (95%-confidence intervals approximately ±20%; Fig. 9).

We conclude that the purely surface- (i.e. wind-) driven part of the ε(z) profile is probably not affected by the presence or absence of sea ice. Additional regional factors can likely change the vertical structure; however, these were not present in our data set away from the influence of shallow topography over the shelf. This means that sea ice alters vertical mixing first and foremost in the form of K_ρ via stronger and shallower stratification. Note however that most of our stations were conducted in the highly mobile ice of the Marginal Ice Zone; the interior ice pack might shield the ocean underneath better from wind energy input.

d. Near-inertial energy

Near-inertial energy input from wind stress can lead to turbulence in the upper ocean through several mechanisms including bulk shear spiking, modulation of near-inertial shear and strain to allow conditions favourable for turbulence production, and breaking of near-inertial internal waves.

Following a storm event in the Amundsen Basin in the central Arctic Ocean, Fer (2014) found that dissipation averaged in the pycnocline was near-inertially modulated, and decayed approximately at a rate implied by the reduction of near-inertial energy over time. In contrast, in the Canada Basin, where the surface layer stratification was substantially stronger than the Amundsen Basin, Lincoln et al. (2016) observed that despite unusually ice-free and stormy conditions, turbulence was not energetic below the stratified upper layer.

Diagnosis of input and fate of near-inertial energy requires detailed observation of upper ocean current time series. These are not available for most of our microstructure data, nor is the analysis of isolated high-energy events practical in a bulk statistics methodology as we employ in this study. We therefore refrain from general inferences about near-inertial mixing in the seasonal pycnocline, but in light of the still unclear role of near-inertial energy in mixing the upper ocean, a few remarks are worthwile.

In our data, near-inertial energy can be inferred from the amplitude of the clockwise semidiurnal component of the ice velocity $A_{SD,cw}$. In the data analyzed here, these amplitudes are rather small (ranging between 0.005 and 0.08 m s^{-1}) and near-inertial oscillations are seen to enhance dissipation rates in the surface layer ($r_\sigma \leq 0.2$), but not below (Fig. 7 C). The presence of inertial oscillations often coincided with stronger winds during N-ICE2015 (not shown), which can also account for the increase in SL dissipation levels. As most of the ice-ocean shear should be located in the PC, near-inertial shear spiking was probably not an important turbulence generation mechanism in the seasonal pycnocline of the Marginal Ice Zone as observed from late May onwards on the N-ICE campaign.

e. Summary for Objective 3

The vertical extent of the mixing layer is regulated by the accumulation of meltwater in the IOBL. The "equivalent mixed layer depth" h_{BD} is an approximate upper bound for the mixing layer depth h_ε, and the two are approximately equal for sufficiently strong wind ($E_0 > 10^{-3}$ kg s^{-3}). In addition, both h_{BD} and the "buoyancy deficit" BD are strongly affected by stratification, which influences the magnitude and vertical structure of ε and K_ρ.

The presence or absence of sea ice did not have a discernible impact on the intensity and vertical structure of surface-driven turbulent mixing. However, since sea ice is the source of a continuous meltwater flux, stratification under sea ice is generally stronger and h_{BD} values are smaller which leads to shallower mixing layers and decreased eddy diffusivities K_ρ. Within the limitations of our data set, we can further state that near-inertial shear (localized in time and space) was not found to generate enhanced mixing in the seasonal pycnocline.

6. Synthesis

a. A conceptual model of mixing in summertime meltwater layers

Before quantifying how the dissipation profiles react to changes in different key variables, we interpret the previous section's results and distil them into a qualitative model of how upper ocean stratification evolves after the onset of the melt season (Fig. 10). The positive buoyancy flux (increasing BD) from ice and snow melt simultaneously freshens the surface layer (increasing $\Delta\sigma_\theta$) and shoals the pycnocline (decreasing h_{BD}).

In the upper ten meters, mixing is dominated by wind-generated shear (Fig. 5 J). The fact that $\varepsilon \propto N$ both in the PC and below is consistent with dissipation of a single frequency or narrow-band internal wave, such as near-inertial internal waves. This scaling corresponds to Type 1 of Gargett and Holloway (1984) who suggest that waves of a single (or narrow band) frequency scale as $\varepsilon \propto N^{+1}$ (as opposed to a Garrett&Munk-like internal wave field which scales as $\varepsilon \propto N^{+1.5}$, their Type 2). In the SL, similar breaking of near-inertial waves at stronger stratification might be offset by enhanced penetration of wind work at weaker stratification, but evidence remains inconclusive due to many correlated variables. Note that internal wave spectra in the Arctic Ocean have been found to deviate from the Garret&Munk form (D'Asaro and Morison 1992; Fer et al. 2010). Vertical wavenumber spectra of horizontal velocity are a factor of 10–100 below the mid-latitude spectra at low wavenumbers, but are comparable in magnitude and slope at high wavenumbers where the spread is less. This indicates a tendency toward a common scaling at small scales where dissipation occurs.

The specifics of the recent E_0 and $\langle w'b' \rangle_0$ forcing then dominate h_{BD} (speculatively: on time scales of weeks) which determines the freshwater distribution, while the temporal seasonal integral of $\langle w'b' \rangle_0$ (which is proportional to the BD accumulated up until that point) does not influence the shape of the density profile. This explains that BD $\propto N^2$, and together with $\varepsilon \propto N$, means that as the melt season progresses, the upward turbulent flux of buoyancy through the PC ($\langle w'b' \rangle \approx 0.2\varepsilon$) increases steadily while $K_\rho \approx 0.2\varepsilon/N^2$ decreases.

b. Future summertime mixing in the upper-ocean

2007, 2011 and 2012 saw the lowest September minimum extent of Arctic sea ice since the beginning of satellite observations of the Arctic ice cover. As the Arctic sea ice cover shrinks and thins (Stroeve et al. 2012), the ice-albedo effect will drive higher melt rates. Thus the main parameter driving changes in the summertime IOBL will be the melt rate $\langle w'b' \rangle_0$ and, to a lesser extent, the seasonally integrated melt BD.

The sensitivity of K_ρ to varying BD and h_{BD} that we determined in Section 5 summarizes the status quo. Randomly selecting two profiles from our data set with different h_{BD} and BD values, their relative difference in K_ρ(z) would, on average, be determined by these sensitivities. However, if the average melt rate increased, we could expect that the temporal evolution of the density profiles changes, taking a different route in BD-h_{BD} parameter space altogether. In particular, with an increase in $\Delta\sigma_\theta$, we can expect h_{BD} to decrease and BD to increase relative to a lower melt rate after the same amount of time elapsed after the onset of melt (compare cases of weak and strong melt in Fig. 10 B).

However, there are no indications that a change in average melt rates would change the diversity of h_{BD} values encountered early in the season. Thus, along lines of constant $\Delta\sigma_\theta$, the bulk of the profiles in our dataset and under higher melt rates would overlap with each other and lead to little change early in the season. The main difference would be that higher values of $\Delta\sigma_\theta$ would be reached earlier. Late in the season, it will become noticeable that the asymptotic h_{BD}^{∞} decreases as melt rates increase, and that the overall BD is larger (see Fig. 10 B). Both of these factors contribute to decreasing K_ρ.

McPhee et al. (1998) noted a seasonally integrated freshwater addition of 0.8 m (BD $\approx$ 20 kg m^{-2}) during the AIDJEX campaign (1975) in the Beaufort Gyre. This figure is consistent with the roughly 0.6 m of freshwater equivalent of seasonal ice melt Timmermans et al. (2011) give for the years 2007-2010 in the Eurasian Basin. Taking the maximum BD $\approx$ 45 kg m^{-2} of our data set, our analysis would indicate a difference of $\frac{\partial \log_{10} K_\rho}{\partial \mathrm{BD}} \cdot \Delta\mathrm{BD} \approx -0.02 \cdot (45-20) = -0.5$, i.e., K_ρ at 20 m depth in the MIZ in late summer is possibly a factor of 3 lower than in the interior ice pack. Therefore, even though insolation often leads to higher water temperatures in the MIZ and therefore larger vertical heat fluxes, some, if not all, of the effect of this temperature increase might be offset by a corresponding decrease in K_ρ.

An additional complication is that when melt rates are high enough to melt all the ice before the end of the melting season, open-water processes might play a role late in the season. However, as we showed above, the main difference between the presence and absence of sea ice lies in fact primarily in that sea ice is a buoyancy source and supplies a positive $\langle w'b' \rangle_0$. The absence of such a buoyancy flux then likely leads to deepening h_{BD}, decreasing overall N^2 and thus increasing K_ρ. Quantifying these processes will require more dedicated measurements that resolve the late-season and open-water variability.

c. Implications for the Arctic marine ecosystem

Photosynthesis can only take place in the sunlit part of the water column, which in the Arctic Ocean means the uppermost tens of meters (e.g. Stein and MacDonald 2004). Just as spring stratification and the associated reduction in vertical eddy diffusivity likely play a role in timing of under-ice algal blooms (see the critical mixing hypothesis, e.g. Huisman et al. 1999), increased water column stability will limit the resupply of nutrients from below. The present study is therefore of immediate interest to understanding the upper-ocean ecosystem in polar waters.

Note that even though K_ρ decreases as the melt season progresses, this does not strictly imply a reduction in the vertical fluxes of tracers feeding into the meltwater layer. In the course of the season, the concentration gradients over which the fluxes are calculated might move to a level below the pycnocline where stratification is not as strong. Comparing Panels D and L (Fig. 5), one sees that K_ρ remains constant immediately below the seasonal pycnocline. For instance, as the season progresses, the nitracline moves downward, such that vertical nitrate fluxes are relatively invariant with respect to time within the productive season (Randelhoff et al. 2016).

If the ice cover vanishes from some region towards the end of melt season, deepening h_{BD} will allow the entrainment of nutrients into the surface layer. Thus the fall blooms in the Arctic Ocean recently observed by Ardyna et al. (2014) may well be linked to the receding ice cover through changes in hydrography, not necessarily through enhanced light input that results from the absence of sea ice.

d. Arctic-wide applicability and limitations

A few notes on the applicability of these results to other parts of the Arctic Ocean are in order. Two types of hydrographic scenarios occur commonly in the Arctic Ocean: (1) In the Boundary Current along the shelf slope, presence of saline Atlantic Water near the surface enables thermal convection. Also the Arctic shelf seas tend to be vertically homogeneous at the end of winter due to haline convection and relatively strong (e.g. tidal) mixing. Similarly, in most of the deep Eurasian Basin (“Atlantic” Arctic water masses), winter mixed layers are deep (mostly well below 50 m; see e.g. Rudels et al. (2004)). Thus the perennial pycnocline does not interfere with the development of a shallow seasonal pycnocline as detailed here. The remnant of the previous winter’s mixed layer then provides a convenient way to define the reference level (r_σ=1). (2) In the Pacific sector of the Arctic Ocean and in particular in the deep Canadian Basin, the upper ocean is strongly stratified, both throughout the year and far beyond the extent of the seasonal input of meltwater.

The rationale behind the approach taken for our data set was that most of the boundary layer shear is accumulated in the shallow and strong pycnocline (cf. Randelhoff et al. 2014), and that the reference level r_σ=1 therefore represents a natural scale of the limits to the vertical extent of wind-driven turbulent mixing. When the underlying perennial stratification is comparably strong, this vertical scale is not obvious from the density profile alone.

The study by Timmermans et al. (2011) provides a suitable set of test scenarios to explore the challenges for our formalism across scenarios (1) and (2), e.g. the distinction between “eastern” and “western” Arctic water masses, the latter strongly stratified below the seasonal meltwater accumulation, the former only weakly. Based on Ice-Tethered Profiler (ITP) data, Timmermans et al. (2011) found that owing to large-scale shifts in atmospheric circulation (cf. Arctic high), in 2009-2010, the western Eurasian Basin was populated by strongly stratified water masses from the western Arctic (our scenario (2)), whereas in 2007-2008, the stratification was more similar to what is commonly found in the eastern Eurasian Basin (our scenario (1)). This is shown by profiles sampled between 87.5 and 86 °N during summertime by ITPs 7 (2007) and 38 (2010) (Fig. 11 A). The vertical structure and the h_{BD}-BD parameter space for the ITP 7 data

(Fig. 11 B) is similar to what we have described in this study, consistent with the stipulations above, and shows the discussed evolution in h_{BD}-BD space as the season progresses. For the ITP 38 data, the mean hydrographic profile shows that melt rates have not lead to a significant accumulation of meltwater in the upper tens of meters. Therefore, no obvious reference depth can be inferred from the density profile. Arbitrarily choosing 50 m as a reference depth for ITP 38 purely for illustrative purposes, we find that the temporal evolution in h_{BD}-BD space now looks convoluted, and in fact is mostly dominated by lateral, non-seasonal changes in hydrography as ITP 38 drifted south towards Fram Strait (Fig. 11 C). This is not a shortcoming of our framework itself, but it does demonstrate that the seasonal meltwater cycle might not dominate the near-surface freshwater inventory in the interior ice pack. Our findings are thus mostly applicable in the seasonal ice zone where leads and the ice-albedo feedback can lead to high melt rates. Note however that this seasonal ice zone has been expanding in recent decades (Stroeve et al. 2012), which could lead to strengthening of seasonal stratification also in the central Arctic Ocean that has not been subject to large melt rates previously.

7. Summary and perspectives

While it is generally agreed that meltwater layers occurring during the Arctic summer affect air-ice-sea interaction in a number of important ways, a quantitative description has so far been lacking. We have shown that their vertical density structure can be described in terms of three parameters, $\Delta\sigma_\theta$ ("surface density deviation"), h_{BD} ("equivalent mixed layer depth") and BD ("buoyancy deficit"), two of which are independent. These parameters integrate the total amount of buoyancy deficit due to meltwater the upper ocean has received, and its vertical distribution. Turbulent dissipation and vertical eddy diffusivity are generally rapidly attenuated in the seasonal pycnocline and beyond, and their vertical profiles have well-defined responses to h_{BD} and BD. In general, stronger melt leads to higher BD, lower h_{BD}, stronger stratification N^2 in the pycnocline, larger dissipation (scaling as $\varepsilon \propto N$), and thus weaker diffusivity (scaling as $K_\rho \propto N^{-1}$) in the pycnocline. In Fig. 5, we have summarized the sensitivities of these key variables to basic hydrographic forcing. Finding the corresponding panel in the figure allows the reader to make their own inference for a given scenario of BD-h_{BD} values. For instance, we have inferred a sensitivity $\frac{\partial \log_{10} K_\rho}{\partial \mathrm{BD}} \approx -0.02 \frac{1}{\mathrm{kg\ m^{-2}}}$.

Seasonal stratification and the associated changes in vertical mixing are key to understanding their respective contributions to and implications for the current and future state of the Arctic Ocean. Our results imply that increasing melt rates will appreciably decrease diapycnal mixing between the surface layer and the water beneath melting Arctic sea ice in summer, even further than is the case already now. In the case of solar heating, higher melt rates thus have a restoring feedback, reducing the oceanic heat flux. It is an open question whether the heat accumulated in near-surface temperature maxima is mixed up during fall (i.e., delaying the onset of freezing altogether) or only after the onset of haline convection (i.e., slowing down ice growth in winter).

The transmission and dissipation of near-inertial energy through an ice-free surface ocean and into the deep basins of the Arctic Ocean deserves further attention as it regulates ocean climate and the heat flux from Atlantic and Pacific Waters to the sea ice. Future melt rates may therefore play a crucial role in modulating ice-ocean interaction far beyond the extent of the seasonal pycnocline.

Acknowledgments. AR's work was supported through the project CARBON BRIDGE: Bridging marine productivity regimes: How Atlantic advective inflow affects productivity, carbon cycling and export in a melting Arctic Ocean, a Polar Programme (project 226415) funded by the Norwegian Research Council. IF was partly supported by the Centre for Climate Dynamics at the Bjerknes Centre through grant BASIC: Boundary Layers in the Arctic Atmosphere, Seas and Ice Dynamics. ICE-2012 and N-ICE2015 data collection was supported by the Norwegian Polar Institute's Centre for Ice, Climate and Ecosystems (ICE) through the ICE Fluxes and N-ICE2015 projects, respectively. N-ICE2015 had additional support from the Ministry of Climate and Environment, and Ministry of Foreign Affairs of Norway. We thank the captains and crews of R/Vs Helmer Hanssen and Lance, and all the scientists involved in the field campaigns for their support. N-ICE2015 data is available from Norwegian Polar Data Centre (https://data.npolar.no/) under the keyword N-ICE2015. Lana Cohen provided wind and air-ice stress measurements for the N-ICE2015 campaign. Gunnar Spreen extracted and provided the sea ice concentration data for the N-ICE2015 campaign. The Ice-Tethered Profiler data were collected and made available by the Ice-Tethered Profiler Program (Toole et al. 2011; Krishfield et al. 2008) based at the Woods Hole Oceanographic Institution (http://www.whoi.edu/itp). Two anonymous reviewers have provided valuable criticism.

References

Anderson, R. J., 1987: Wind stress measurements over rough ice during the 1984 Marginal Ice Zone Experiment. *Journal of Geophysical Research: Oceans*, **92 (C7)**, 6933–6941, doi:10.1029/JC092iC07p06933, URL http://dx.doi.org/10.1029/JC092iC07p06933.

Ardyna, M., M. Babin, M. Gosselin, E. Devred, L. Rainville, and J.-E. Tremblay, 2014: Recent Arctic Ocean sea ice loss triggers novel fall phytoplankton blooms. *Geophysical Research Letters*, **41 (17)**, 62076212, doi:10.1002/2014gl061047, URL http://dx.doi.org/10.1002/2014GL061047.

Brainerd, K. E., and M. C. Gregg, 1995: Surface mixed and mixing layer depths. *Deep Sea Research Part I: Oceanographic Research Papers*, **42 (9)**, 1521 – 1543, doi:http://dx.doi.org/10.1016/0967-0637(95)00068-H, URL http://www.sciencedirect.com/science/article/pii/096706379500068H.

D'Asaro, E. A., and J. H. Morison, 1992: Internal waves and mixing in the Arctic Ocean. *Deep Sea Research Part A. Oceanographic Research Papers*, **39 (2, Part 1)**, S459 – S484, doi:10.1016/S0198-0149(06)80016-6, URL http://www.sciencedirect.com/science/article/pii/S0198014906800166.

Denman, K. L., and M. Miyake, 1973: Upper layer modification at ocean station papa: Observations and simulation. *Journal of Physical Oceanography*, **3 (2)**, 185–196, doi:10.1175/1520-0485(1973)003⟨0185:ULMAOS⟩2.0.CO;2.

Dewey, R. K., and J. N. Moum, 1990: Enhancement of fronts by vertical mixing. *Journal of Geophysical Research: Oceans (1978–2012)*, **95 (C6)**, 9433–9445.

Fer, I., 2006: Scaling turbulent dissipation in an Arctic fjord. *Deep Sea Research Part II: Topical Studies in Oceanography*, **53**, 77 – 95, doi:10.1016/j.dsr2.2006.01.003, IAPSO/SCOR Conference on Ocean Mixing.

Fer, I., 2014: Near-inertial mixing in the central Arctic Ocean. *Journal of Physical Oceanography*, **44 (8)**, 20312049, doi:10.1175/jpo-d-13-0133.1, URL http://dx.doi.org/10.1175/JPO-D-13-0133.1.

Fer, I., R. Skogseth, and F. Geyer, 2010: Internal waves and mixing in the Marginal Ice Zone near the Yermak Plateau. *Journal of Physical Oceanography*, **40 (7)**, 1613–1630, doi:10.1175/2010JPO4371.1, URL http://dx.doi.org/10.1175/2010JPO4371.1, http://dx.doi.org/10.1175/2010JPO4371.1.

Gargett, A. E., and G. Holloway, 1984: Dissipation and diffusion by internal wave breaking. *Journal of Marine Research*, **42 (1)**, 15–27, doi:10.1357/002224084788506158, URL http://dx.doi.org/10.1357/002224084788506158.

Granskog, M., P. Assmy, S. Gerland, G. Spreen, H. Steen, and L. Smedsrud, 2016: Arctic research on thin ice: Consequences of Arctic sea ice loss. *Eos*, **97**, doi:10.1029/2016eo044097, URL http://dx.doi.org/10.1029/2016EO044097.

Granskog, M. A., A. K. Pavlov, S. Sagan, P. Kowalczuk, A. Raczkowska, and C. A. Stedmon, 2015: Effect of sea-ice melt on inherent optical properties and vertical distribution of solar radiant heating in arctic surface waters. *Journal of Geophysical Research: Oceans*, **120 (10)**, 7028–7039, doi:10.1002/2015JC011087, URL http://dx.doi.org/10.1002/2015JC011087.

Guest, P. S., and K. L. Davidson, 1987: The effect of observed ice conditions on the drag coefficient in the summer East Greenland Sea Marginal Ice Zone. *Journal of Geophysical Research: Oceans*, **92 (C7)**, 6943–6954, doi:10.1029/JC092iC07p06943, URL http://dx.doi.org/10.1029/JC092iC07p06943.

Haine, T. W., and Coauthors, 2015: Arctic freshwater export: Status, mechanisms, and prospects. *Global and Planetary Change*, **125**, 13 – 35, doi:http://dx.doi.org/10.1016/j.gloplacha.2014.11.013, URL http://www.sciencedirect.com/science/article/pii/S0921818114003129.

Hudson, S. R., M. A. Granskog, A. Sundfjord, A. Randelhoff, A. H. H. Renner, and D. V. Divine, 2013: Energy budget of first-year Arctic sea ice in advanced stages of melt. *Geophysical Research Letters*, **40 (11)**, 2679–2683, doi:10.1002/grl.50517.

Huisman, J., P. van Oostveen, and F. J. Weissing, 1999: Critical depth and critical turbulence: Two different mechanisms for the development of phytoplankton blooms. *Limnology and Oceanography*, **44 (7)**, 1781–1787, doi:10.4319/lo.1999.44.7.1781, URL http://dx.doi.org/10.4319/lo.1999.44.7.1781.

Itkin, P., and Coauthors, 2015: N-ICE2015 buoy data. Norwegian Polar Institute, URL https://doi.org/10.21334/npolar.2015.6ed9a8ca, doi:10.21334/npolar.2015.6ed9a8ca.

Krishfield, R., J. Toole, A. Proshutinsky, and M.-L. Timmermans, 2008: Automated Ice-Tethered Profilers for seawater observations under pack ice in all seasons. *Journal of Atmospheric and Oceanic Technology*, **25 (11)**, 2091–2105, doi:10.1175/2008JTECHO587.1, URL http://dx.doi.org/10.1175/2008JTECHO587.1, http://dx.doi.org/10.1175/2008JTECHO587.1.

Levine, M. D., C. A. Paulson, and J. H. Morison, 1985: Internal waves in the Arctic Ocean: Comparison with lower-latitude observations. *Journal of Physical Oceanography*, **15**, 800–809.

Li, W. K. W., F. A. McLaughlin, C. Lovejoy, and E. C. Carmack, 2009: Smallest algae thrive as the Arctic Ocean freshens. *Science*, **326 (5952)**, 539539, doi:10.1126/science.1179798, URL http://dx.doi.org/10.1126/science.1179798.

Lincoln, B. J., T. P. Rippeth, Y.-D. Lenn, M. L. Timmermans, W. J. Williams, and S. Bacon, 2016: Wind-driven mixing at intermediate depths in an ice-free Arctic Ocean. *Geophysical Research Letters*, **43 (18)**, 9749–9756, doi:10.1002/2016GL070454, URL http://dx.doi.org/10.1002/2016GL070454, 2016GL070454.

Martin, T., M. Steele, and J. Zhang, 2014: Seasonality and long-term trend of Arctic Ocean surface stress in a model. *J. Geophys. Res. Oceans*, **119 (3)**, 1723–1738, doi:10.1002/2013jc009425, URL http://dx.doi.org/10.1002/2013JC009425.

McPhee, M. G., and L. H. Kantha, 1989: Generation of internal waves by sea ice. *Journal of Geophysical Research: Oceans*, **94 (C3)**, 3287–3302, doi:10.1029/JC094iC03p03287.

McPhee, M. G., G. A. Maykut, and J. H. Morison, 1987: Dynamics and thermodynamics of the ice/upper ocean system in the marginal ice zone of the Greenland Sea. *Journal of Geophysical Research: Oceans*, **92 (C7)**, 7017–7031, doi:10.1029/JC092iC07p07017.

McPhee, M. G., T. P. Stanton, J. H. Morison, and D. G. Martinson, 1998: Freshening of the upper ocean in the arctic: Is perennial sea ice disappearing? *Geophysical Research Letters*, **25 (10)**, 1729–1732, doi:10.1029/98GL00933.

Morison, J., R. Kwok, C. Peralta-Ferriz, M. Alkire, I. Rigor, R. Andersen, and M. Steele, 2012: Changing Arctic Ocean freshwater pathways. *Nature*, **481 (7379)**, 66–70, doi:10.1038/nature10705, URL http://dx.doi.org/10.1038/nature10705.

Morison, J. H., C. E. Long, and M. D. Levine, 1985: Internal wave dissipation under sea ice. *Journal of Geophysical Research*, **90 (C6)**, 11,959–11,966.

Moum, J. N., 1996: Energy-containing scales of turbulence in the ocean thermocline. *Journal of Geophysical Research*.

Osborn, T. R., 1980: Estimates of the local rate of vertical diffusion from dissipation measurements. *J. Phys. Oceanogr.*, **10 (1)**, 83–89, doi:10.1175/1520-0485(1980)010⟨0083:EOTLRO⟩2.0.CO;2.

Peralta-Ferriz, C., and R. A. Woodgate, 2015: Seasonal and interannual variability of pan-Arctic surface mixed layer properties from

1979 to 2012 from hydrographic data, and the dominance of stratification for multiyear mixed layer depth shoaling. *Progress in Oceanography*, **134**, 19 – 53, doi:http://dx.doi.org/10.1016/j.pocean.2014.12.005, URL http://www.sciencedirect.com/science/article/pii/S0079661114002158.

Proshutinsky, A., and Coauthors, 2009: Beaufort gyre freshwater reservoir: State and variability from observations. *Journal of Geophysical Research: Oceans*, **114 (C1)**, n/a–n/a, doi:10.1029/2008JC005104, URL http://dx.doi.org/10.1029/2008JC005104.

Randelhoff, A., I. Fer, A. Sundfjord, J.-E. Tremblay, and M. Reigstad, 2016: Vertical fluxes of nitrate in the seasonal nitracline of the Atlantic sector of the Arctic Ocean. *Journal of Geophysical Research: Oceans*, **121 (7)**, 5282–5295, doi:10.1002/2016JC011779, URL http://dx.doi.org/10.1002/2016JC011779.

Randelhoff, A., A. Sundfjord, and A. H. H. Renner, 2014: Effects of a shallow pycnocline and surface meltwater on sea ice-ocean drag and turbulent heat flux. *J. Phys. Oceanogr.*, **44 (8)**, 2176–2190, doi:10.1175/jpo-d-13-0231.1, URL http://dx.doi.org/10.1175/JPO-D-13-0231.1.

Rudels, B., 2016: Arctic Ocean stability: The effects of local cooling, oceanic heat transport, freshwater input, and sea ice melt with special emphasis on the Nansen Basin. *Journal of Geophysical Research: Oceans*, **121 (7)**, 44504473, doi:10.1002/2015jc011045, URL http://dx.doi.org/10.1002/2015JC011045.

Rudels, B., E. P. Jones, U. Schauer, and P. Eriksson, 2004: Atlantic sources of the arctic ocean surface and halocline waters. *Polar Research*, **23 (2)**, 181–208, doi:10.1111/j.1751-8369.2004.tb00007.x.

Spreen, G., L. Kaleschke, and G. Heygster, 2008: Sea ice remote sensing using AMsr-e 89-GHz channels. *Journal of Geophysical Research*, **113 (C2)**, doi:10.1029/2005jc003384, URL http://dx.doi.org/10.1029/2005JC003384.

Stein, R., and R. W. MacDonald, Eds., 2004: *The Organic Carbon Cycle in the Arctic Ocean*. Springer Science + Business Media, doi:10.1007/978-3-642-18912-8, URL http://dx.doi.org/10.1007/978-3-642-18912-8.

Stroeve, J. C., M. C. Serreze, M. M. Holland, J. E. Kay, J. Malanik, and A. P. Barrett, 2012: The Arctic's rapidly shrinking sea ice cover: a research synthesis. *Climatic Change*, **110 (3)**, 1005–1027, doi:10.1007/s10584-011-0101-1, URL http://dx.doi.org/10.1007/s10584-011-0101-1.

Sundfjord, A., I. Fer, Y. Kasajima, and H. Svendsen, 2007: Observations of turbulent mixing and hydrography in the marginal ice zone of the Barents Sea. *Journal of Geophysical Research: Oceans*, **112 (C5)**, doi:10.1029/2006JC003524.

Timmermans, M.-L., S. Cole, and J. Toole, 2012: Horizontal density structure and restratification of the Arctic Ocean surface layer. *Journal of Physical Oceanography*, **42 (4)**, 659–668, doi:10.1175/JPO-D-11-0125.1, URL http://dx.doi.org/10.1175/JPO-D-11-0125.1, http://dx.doi.org/10.1175/JPO-D-11-0125.1.

Timmermans, M.-L., A. Proshutinsky, R. A. Krishfield, D. K. Perovich, J. A. Richter-Menge, T. P. Stanton, and J. M. Toole, 2011: Surface freshening in the Arctic Oceans Eurasian Basin: An apparent consequence of recent change in the wind-driven circulation. *Journal of Geophysical Research*, **116**, doi:10.1029/2011jc006975, URL http://dx.doi.org/10.1029/2011JC006975.

Timmermans, M.-L., and P. Winsor, 2013: Scales of horizontal density structure in the Chukchi Sea surface layer. *Continental Shelf Research*, **52**, 39 – 45, doi:http://dx.doi.org/10.1016/j.csr.2012.10.015, URL http://www.sciencedirect.com/science/article/pii/S0278434312002919.

Toole, J., R. Krishfield, M.-L. Timmermans, and A. Proshutinsky, 2011: The Ice-Tethered Profiler: Argo of the Arctic. *Oceanography*, **24 (3)**, 126135, doi:10.5670/oceanog.2011.64, URL http://dx.doi.org/10.5670/oceanog.2011.64.

Yamazaki, H., and T. Osborn, 1990: Dissipation estimates for stratified turbulence. *Journal of Geophysical Research: Oceans*, **95 (C6)**, 9739–9744, doi:10.1029/JC095iC06p09739.

[FIG. 1 about here.]

[FIG. 2 about here.]

[FIG. 3 about here.]

[FIG. 4 about here.]

[FIG. 5 about here.]

[FIG. 6 about here.]

[FIG. 7 about here.]

[FIG. 8 about here.]

[FIG. 9 about here.]

[FIG. 10 about here.]

[FIG. 11 about here.]

LIST OF FIGURES

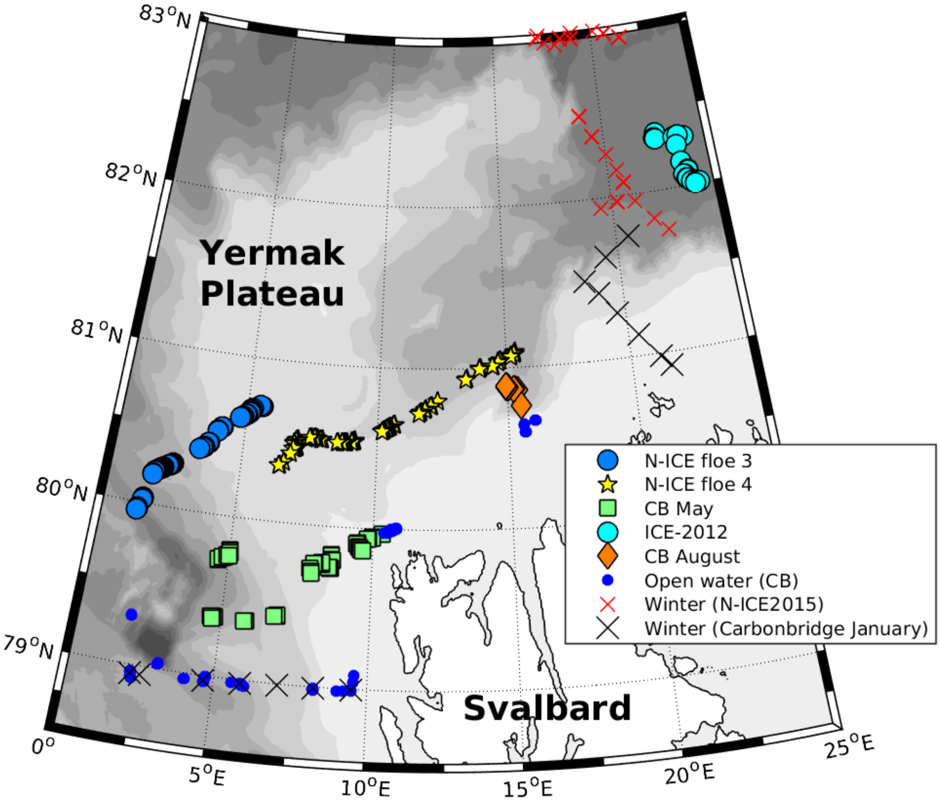

FIG. 1. Map of the study area. Profiles in “open water” (all from Carbonbridge, CB) and with a “deep mixed layer” (“winter (N-ICE2015)” - all ice covered; winter (Carbonbridge, January) - all open water) are marked separately; all other profiles were located under varying concentrations of sea ice (see Section 2 a). Contour shading shows depths at 500-m intervals.

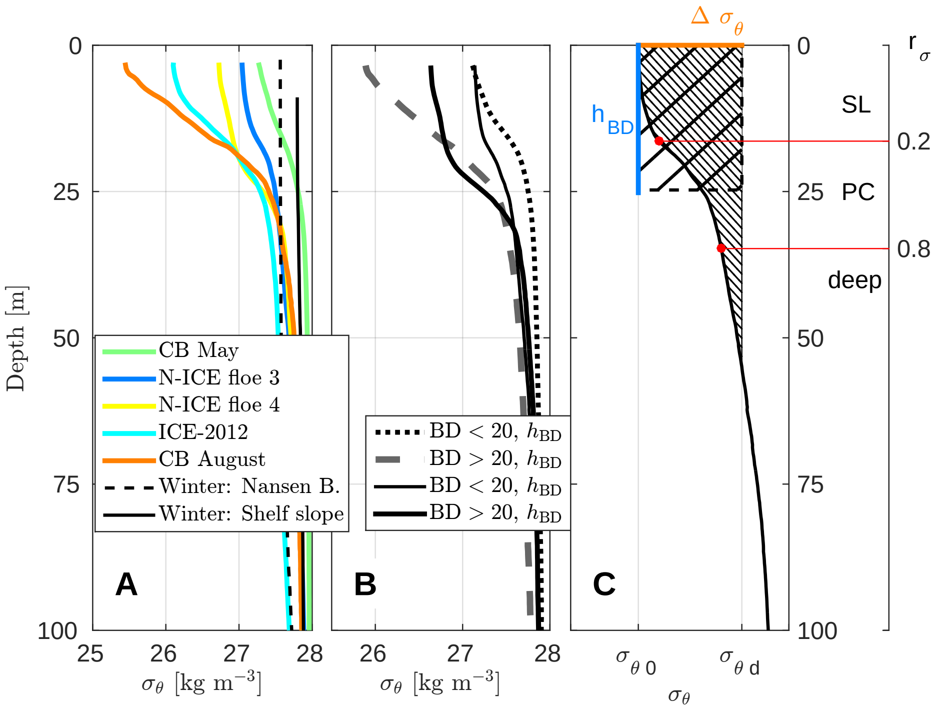

FIG. 2. Survey-average density profiles binned by campaign (A) or by their associated buoyancy deficit BD [m] and the equivalent mixed layer depth h_{BD} [kg m^{-2}] (B). Additionally in Panel A: Winter profiles from the Nansen Basin (N-ICE2015) and from the shelf slope (Carbonbridge, January cruise). C: Example profile illustrating the surface density deviation $\Delta\sigma_\theta$ (horizontal, orange bar), h_{BD} (vertical, blue bar) and BD (equal to each of the hatched areas). The axis on the far right gives the r_σ coordinate associated with panel C and the delineation into SL (surface layer), PC (pycnocline) and “deep” layer. Note the significant vertical stratification in SL.

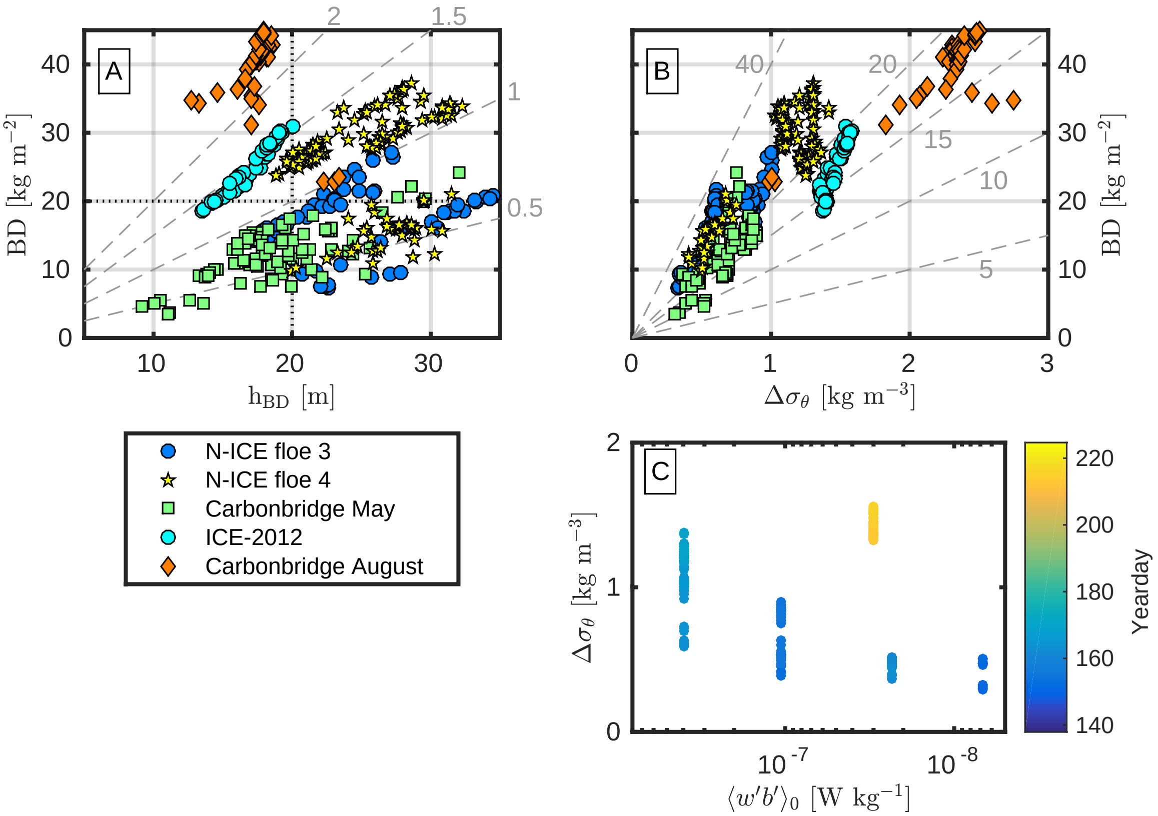

FIG. 3. Parameter range in terms of h_{BD}, $\Delta\sigma_\theta$, BD, and the melt rate. A, B: Dashed lines: Lines of constant $\Delta\sigma_\theta$ (A) as indicated by the numbers in the upper right corner [kg m^{-3}] or h_{BD} [m] (B). Dotted lines in Panel A mark the regimes used for grouping data in Figs. 5 and 8. C: Combined effect of rate and duration of ice melt, here expressed as surface buoyancy flux $\langle w'b' \rangle_0$, on $\Delta\sigma_\theta$.

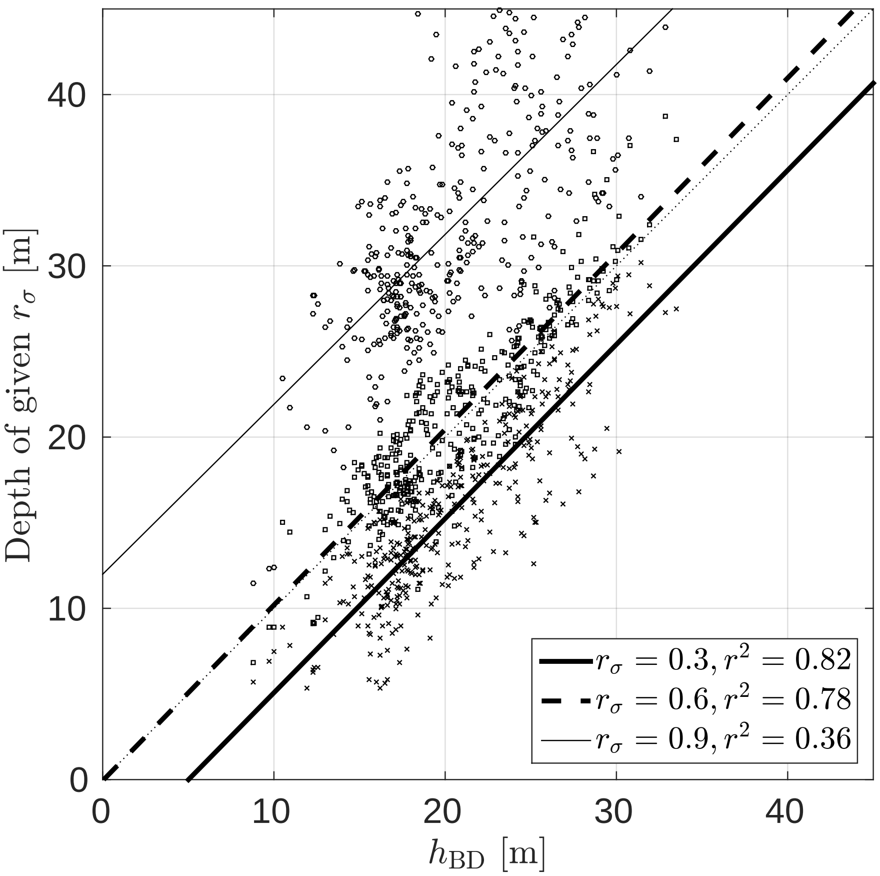

FIG. 4. Relation between h_{BD} and depths of constant r_σ at the levels $r_\sigma = 0.3$ (crosses), 0.6 (squares) and 0.9 (circles). The diagonal lines are linear regressions based on all samples in each category.

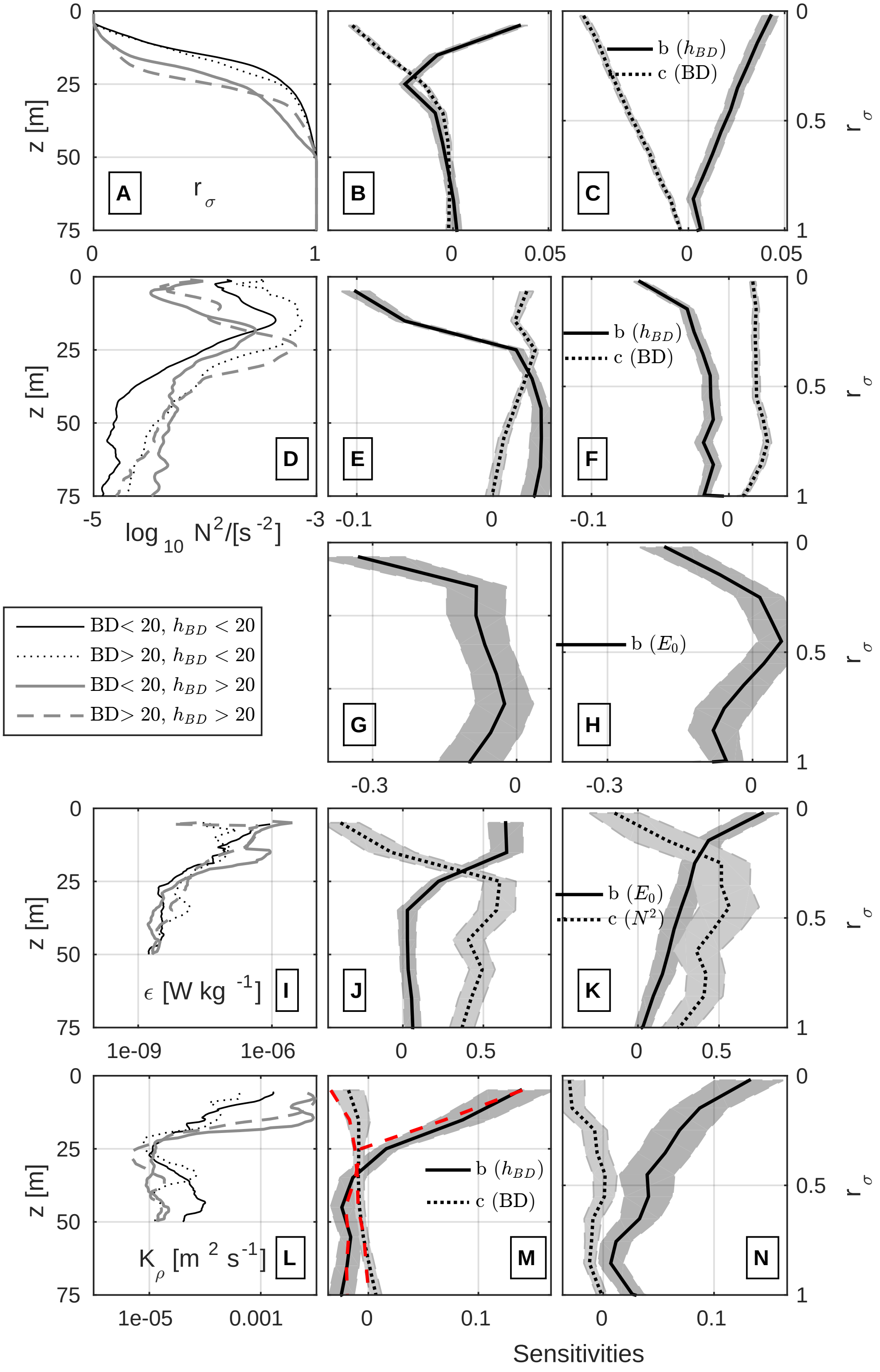

FIG. 5. Mean profiles of r_σ, N^2, ε, K_ρ, and the sensitivities of σ_θ, N^2, ε, K_ρ to various parameters (see legend), as quantified from a linear regression for each subset of observations in vertical bins (distance from surface, z, or scaled density r_σ). First column: Mean profiles. Second column: Profiles of sensitivities plotted against physical depth. Third column: Profiles of sensitivities plotted against r_σ. Differences between the second and third column are due to implicit dependencies of r_σ on N^2, σ_θ etc. (A, D, I, L): Mean profiles of r_σ, N^2, ε, K_ρ, respectively, binned according to their associated h_{BD} and BD values. (B, C): Sensitivity of σ_θ to h_{BD} and BD (b and c in $\sigma_\theta = a + b \cdot h_{\mathrm{BD}} + c \cdot \mathrm{BD}$). (E, F): Sensitivity of N^2 to h_{BD} and BD (b and c in $\log_{10} N^2 = a + b \cdot h_{\mathrm{BD}} + c \cdot \mathrm{BD}$). (G, H): Sensitivity of N^2 to E_0 (b in $\log_{10} N^2 = a + b \cdot \log_{10} E_0$). (J, K): Sensitivity of ε to E_0 and N^2 (b and c in $\log_{10} \varepsilon = a + b \cdot \log_{10} E_0 + c \cdot \log_{10} N^2$). (M, N): Sensitivity of K_ρ to h_{BD} and BD (b and c in $\log_{10} K_\rho = a + b \cdot h_{\mathrm{BD}} + c \cdot \mathrm{BD}$). Red lines in M indicate the sensitivities inferred using Panels J and E as described in Section 5. The shaded areas are 95% confidence intervals from the fit which is linear in every predictor variable mentioned in each panel.

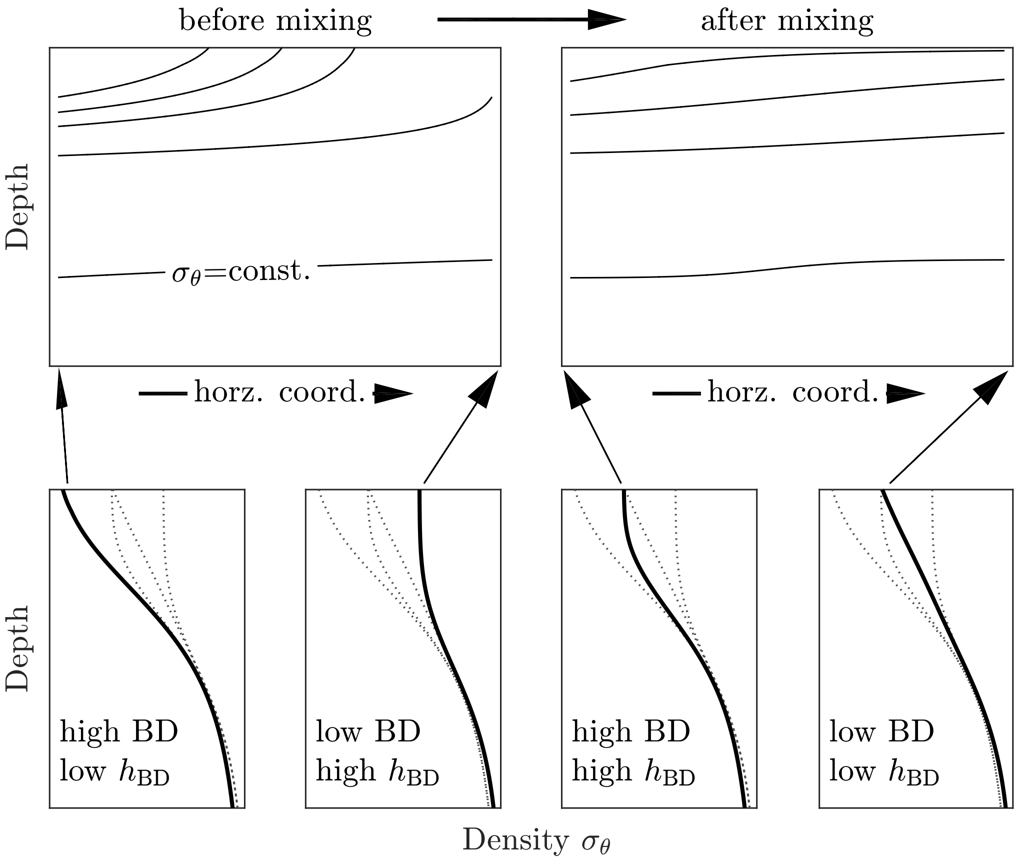

FIG. 6. Hypothetical mixing process that could explain the observed narrow $\Delta\sigma_\theta$ ranges while preserving a large range of BD values. If horizontal mixing in the very surface is much stronger than mixing at depths of a few tens of meters, this generates profiles with very similar $\Delta\sigma_\theta$, but a wide range of BD and accordingly h_{BD} values. Upper panels: Contours of constant σ_θ as function of depth and the cross-front horizontal coordinate before (left) and after (right) mixing has taken place. Lower panels: conceptual profiles at either side of the front, both before and after mixing, with the respective profile in bold and the other profiles dotted.

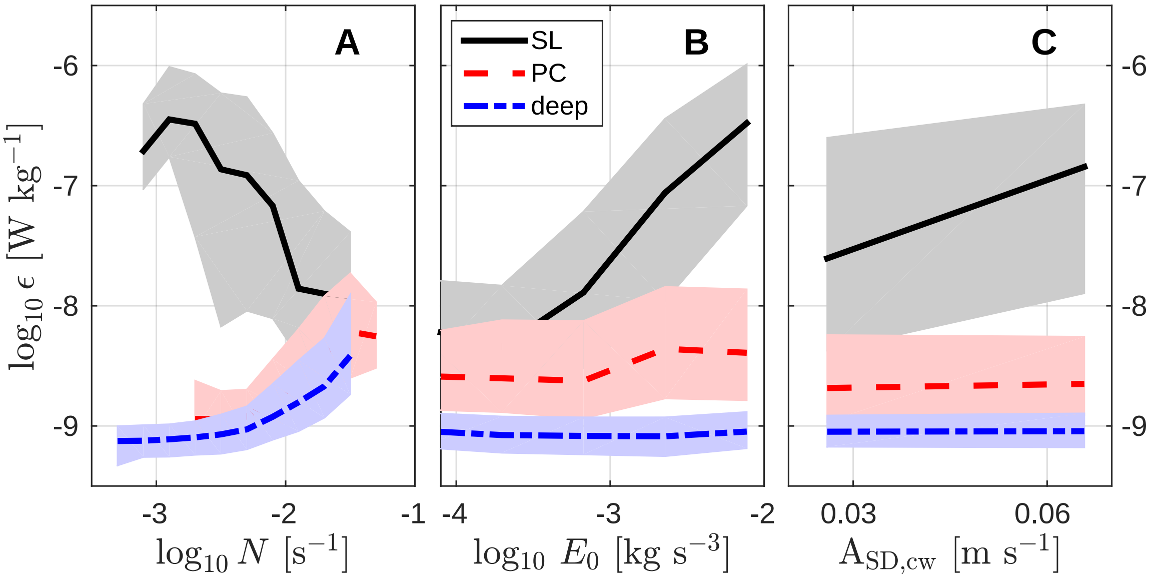

FIG. 7. Dissipation rates $\log_{10}(\varepsilon)$ as a function of (A) stratification N, (B) wind work E_0 and (C) amplitudes of near-inertial motions, grouped according to "surface layer" (SL), "pycnocline" (PC) and "deep" (below PC). Shading indicates the respective first and third quartiles.

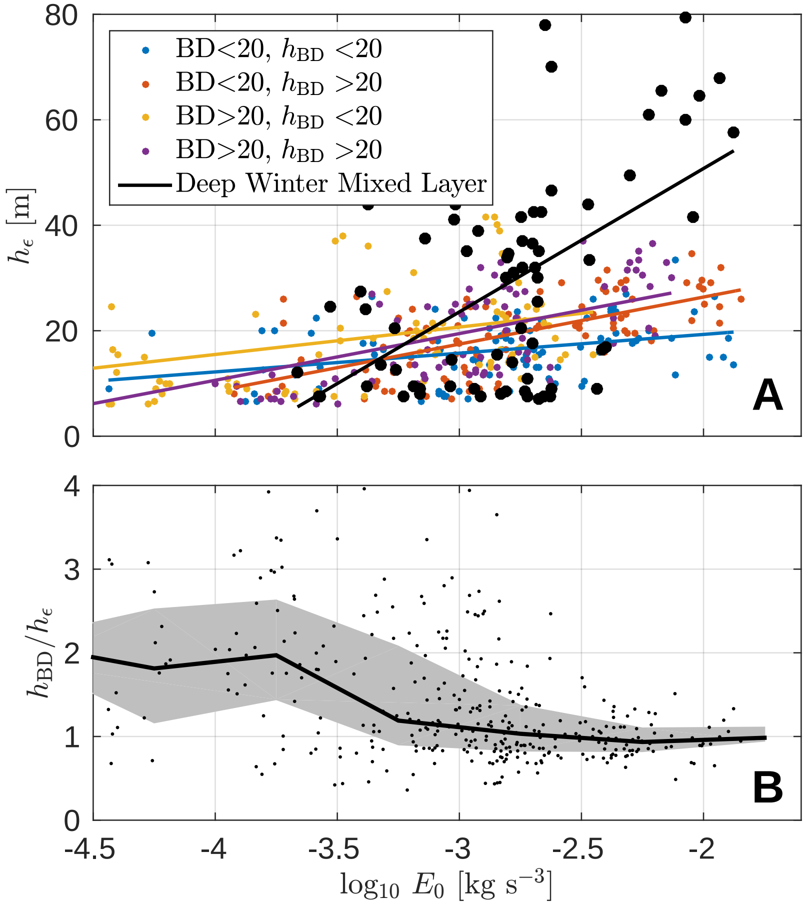

FIG. 8. A: Mixing layer depth h_ε as function of wind work E_0. Colored dots and regression lines refer to meltwater affected profiles, binned according to their associated h_{BD} and BD values. Black dots and regression line refer to deep wintertime mixed layers. B: Discrepancy between equivalent mixed layer depth h_{BD} and mixing layer depth h_ε as a function of wind work, E_0. Shaded area and thick line indicate quartiles and median, respectively.

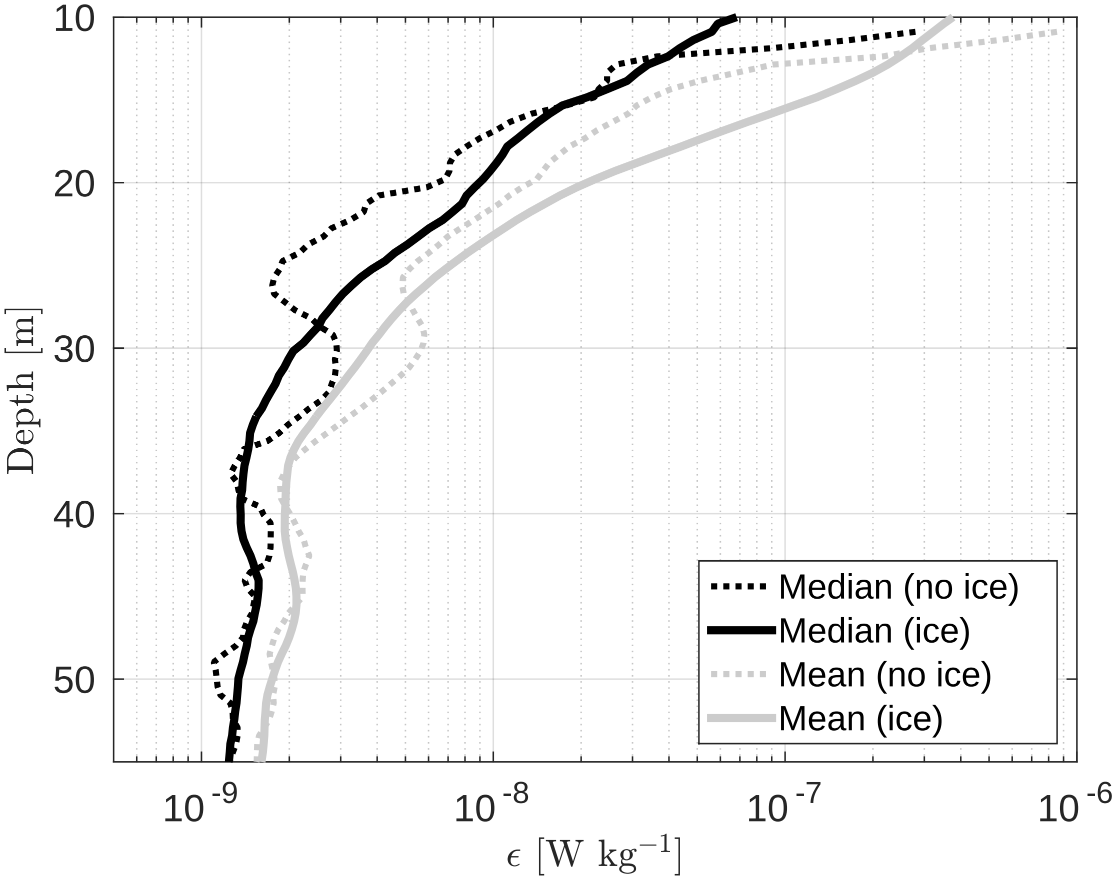

FIG. 9. Vertical profiles of median (black lines) and maximum likelihood estimates of mean (gray lines) dissipation rates at ice-covered (solid lines) and open-water (dotted lines) stations; see the text for details of the subsampling. Sample sizes: Open water (n=30), ice cover (n=170).

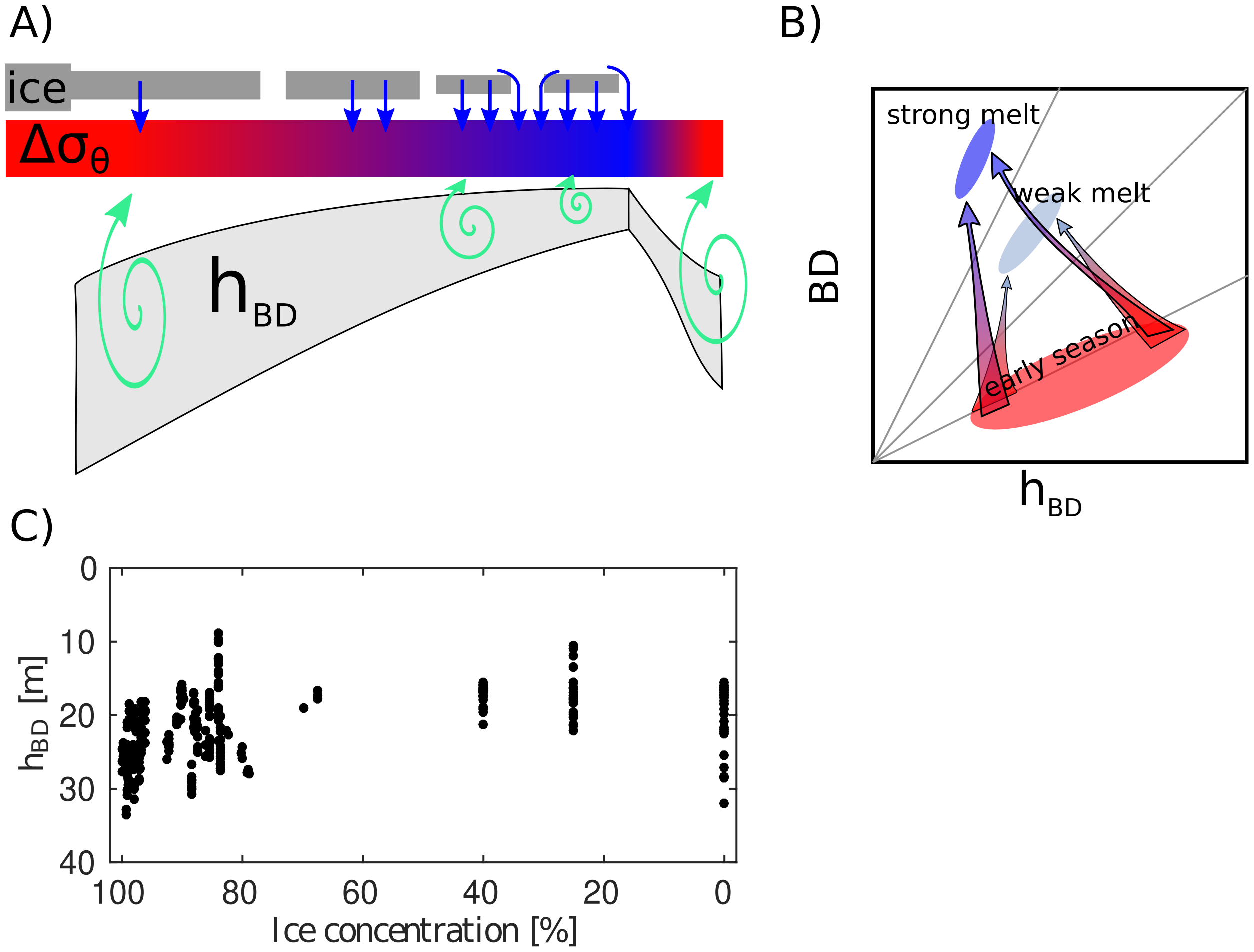

FIG. 10. Sketch of the conceptual model. A: Blue arrows: Meltwater input. The color gradient indicates small (red) to large (blue) surface buoyancy deviations $\Delta\sigma_\theta$. Light grey: Range of equivalent mixed layer depths h_{BD}, narrowing and shoaling as melt rates increase. When the ice vanishes, h_{BD} deepens again and $\Delta\sigma_\theta$ decreases. Green whirls indicate that mixing depth h_ε is constrained by h_{BD}. B: Evolution in BD-h_{BD} parameter space, cf. Fig. 3. Darker blue indicates higher melt rate which leads to higher BD and lower h_{BD} later in the season. C: h_{BD} vs. sea ice concentration as observed in the field, inferred from AMSR2 ASI (downloaded from *https://seaice.uni-bremen.de/amsr2/;* Spreen et al. 2008).

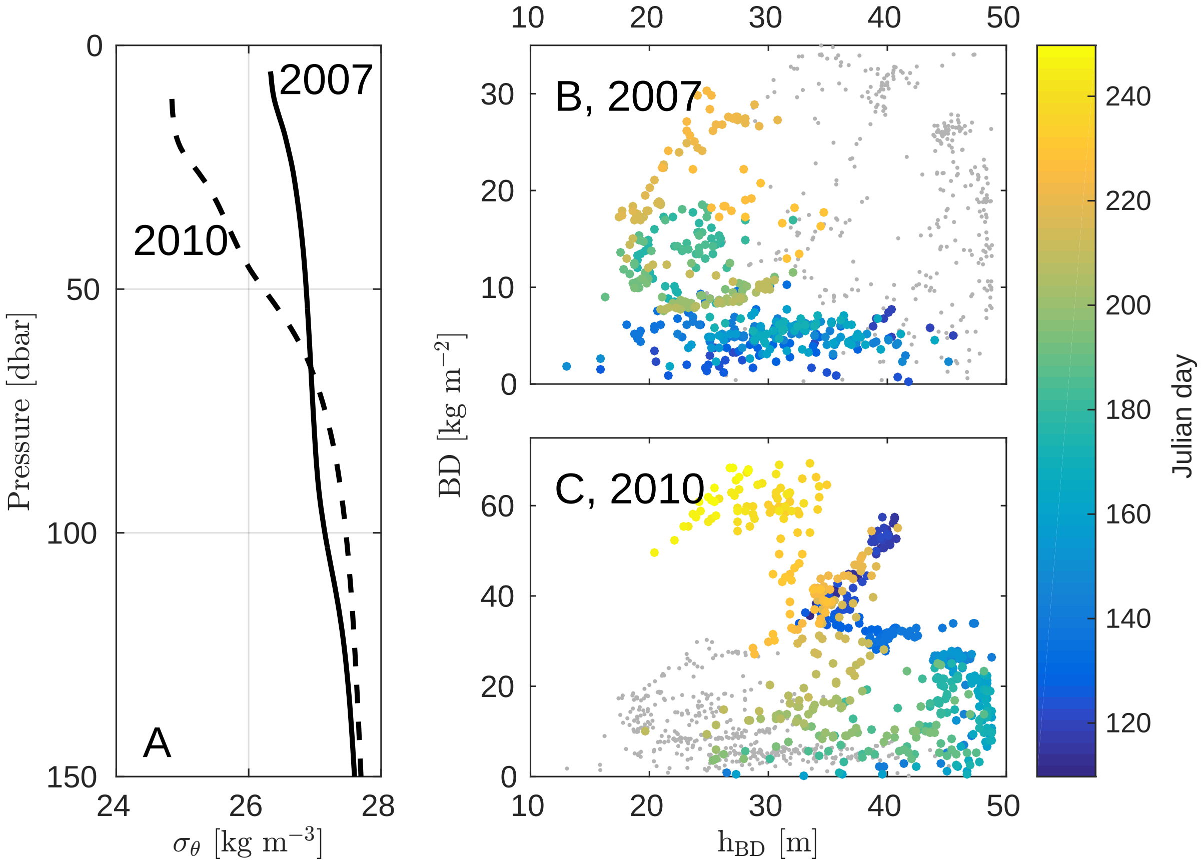

FIG. 11. Ice-Tethered Profiler data. A: Average density profiles sampled between 87.5 and 86 °N in 2007 (#7) and 2010 (#38). B, C: h_{BD}-BD characteristics (see also Fig. 3) from profiles located above 85 °N. Both are based on a reference depth of 50 m, which is robust for 2007; for 2010, the results are sensitive to this (mainly illustrative) choice. The grey dots in B and C show the data from the other panel, respectively, for comparison (note the change in scale on the y-axis).

IV

Randelhoff, A., I. Fer, A. Sundfjord, J.-É. Tremblay, and M. Reigstad (2016), Vertical fluxes of nitrate in the seasonal nitracline of the Atlantic sector of the Arctic Ocean, *Journal of Geophysical Research: Oceans*, *121*, 5282–5295, doi:10.1002/2016JC011779.

AGU PUBLICATIONS

JGR

Journal of Geophysical Research: Oceans

RESEARCH ARTICLE
10.1002/2016JC011779

Special Section:
Atmosphere–ice–ocean–ecosystem processes in a thinner Arctic sea ice regime: the Norwegian young sea ICE cruise 2015 (N–ICE2015)

Key Points:
- The nitrate drawdown in the photic zone is empirically strongly related to the development of seasonal stratification from ice melt
- Upward turbulent nitrate fluxes across the seasonal nitracline are small compared to estimates of annual nitrate drawdown on the shelves
- Under a future seasonal Arctic ice cover, increases in seasonal nitrate fluxes can be significant in the deep Eurasian Basin

Correspondence to:
A. Randelhoff,
achim@npolar.no

Citation:
Randelhoff, A., I. Fer, A. Sundfjord, J.–É. Tremblay, and M. Reigstad (2016), Vertical fluxes of nitrate in the seasonal nitracline of the Atlantic sector of the Arctic Ocean, *J. Geophys. Res. Oceans*, *121*, doi:10.1002/2016JC011779.

Received 7 MAR 2016
Accepted 20 JUN 2016
Accepted article online 23 JUN 2016

Vertical fluxes of nitrate in the seasonal nitracline of the Atlantic sector of the Arctic Ocean

Achim Randelhoff[1,2], Ilker Fer[3], Arild Sundfjord[2], Jean-Éric Tremblay[4], and Marit Reigstad[1]

[1]Institute for Arctic and Marine Biology, UiT The Arctic University of Norway, Tromsø, Norway, [2]Norwegian Polar Institute, Tromsø, Norway, [3]Geophysical Institute, University of Bergen and Bjerknes Centre for Climate Research, Bergen, Norway, [4]Québec-Océan and Takuvik, Département de biologie, Université Laval, Québec, Canada

Abstract This study compiles colocated oceanic observations of high-resolution vertical profiles of nitrate concentration and turbulent microstructure around the Svalbard shelf slope, covering both the permanently ice-free Fram Strait and the pack ice north of Svalbard. The authors present an overview over the seasonal evolution of the distribution of nitrate and its relation to upper ocean stratification. The average upward turbulent diffusive nitrate flux across the seasonal nitracline during the Arctic summer season is derived, with average values of 0.3 and 0.7 mmol m^{-2} d^{-1} for stations with and without ice cover, respectively. The increase under ice-free conditions is attributed to different patterns of stratification under sea ice versus open water. The nitrate flux obtained from microstructure measurements lacked a seasonal signal. However, bottle incubations indicate that August nitrate uptake was reduced by more than an order of magnitude relative to the May values. It remains inconclusive whether the new production was limited by an unidentified factor other than NO_3^- supply in late summer, or the uptake was underestimated by the incubation method.

1. Introduction

The paradigm of upper ocean primary productivity divides the production into "new" (based on allochthonous nitrogen, N, mostly nitrate, NO_3^-) and "regenerated" (autochthonous N, mostly ammonium, NH_4^+) production, and defines an f-ratio as the ratio of new production to total (i.e., sum of new and regenerated) production [e.g., *Dugdale and Goering*, 1967]. In this picture, once the phytoplankton bloom has consumed all available nitrate (high f-ratio), vertical fluxes across the base of the mixed layer are the only source of additional allochthonous nitrate, thereby constraining new (i.e., nitrate-based) production locally, leading to a small f-ratio in a community that feeds mostly on recycled nutrients. Strong seasonality of both photosynthetically available radiation and stratification in the upper Arctic Ocean leads to a seasonal cycle in nutrient concentrations, where nutrients are consumed during summer and replenished during winter. Apart from systems where (e.g., coastal) upwelling can lead to pulsed input of nutrients and intermittent or even sustained blooming [e.g., *Tremblay et al*., 2011], the major mode of nutrient supply to a postbloom ocean surface is diapycnal turbulent diffusion.

The significance of this vertical turbulent flux is twofold: on one hand, it contributes to the depth-integrated drawdown of nitrate. This can act as a measure of net community production, and thus also maximum possible vertical export of carbon [*Tremblay et al*., 2015]. When averaging over horizontal scales large enough to neglect advection with ocean currents, the vertical diffusive flux must also balance export production (i.e., N that is exported to "depth") on interannual time scales [*Eppley and Peterson*, 1979] (plus harvest of marine resources, if the system is not closed). On smaller scales, however, advection can significantly impact nutrient budgets as on the in and outflow shelves of the Arctic Ocean [*Torres-Valdés et al*., 2013].

On the other hand, even if the effect of the vertical nitrate flux on the annual nitrate drawdown is small, it determines the availability of NO_3^- versus NH_4^+ and therefore potentially ecosystem composition (favoring organisms that compete either better or worse for nitrate).

In qualitative terms, the nitrate flux ($F_{\mathcal{N}}$) is often assumed to be small due to the strong stratification in the seasonal pycnocline, but its magnitude and the processes behind remain to be quantified. In addition, upper ocean stratification in the Arctic might change as a consequence of increasing sea ice melt rates [e.g., *Stroeve et al.*, 2011], leading to additional uncertainties about future nutrient supply. Few observations of the upward turbulent nitrate flux in the Arctic exist as of now, often biased either toward a season, local processes, or by undersampling, and are thus potentially not representative of average figures. Here, we present average diffusive nitrate fluxes across the Arctic summer nitracline in ice-covered and open water conditions by compiling ocean microstructure and nitrate concentration profiles from the pack ice north of Svalbard, the Svalbard shelf slope and Fram Strait. The wider area around Svalbard is a region of strong horizontal gradients, featuring both perennial and seasonal ice cover and stratification, and the boundary current inflow of warm Atlantic Water (AW) along the shelf slope. In this study, we aim to quantify postbloom $F_{\mathcal{N}}$ across this wide range of conditions common to the Arctic Ocean and elucidate its relation to NO_3^- -based production.

2. Methods

2.1. Data

Colocated continuous vertical profiles of nitrate concentrations ($\mathcal{N}$) and turbulent microstructure were collected during four campaigns spanning the shelf, shelf slope area, Fram Strait and Nansen Basin west and north of Svalbard (Figure 1), and various types of ice cover, from open water and broken-up floes at the ice edge to near-complete ice cover.

Three of the campaigns were conducted in January, May, and August 2014, as part of the CarbonBridge project, aboard the ice-reinforced R/V Helmer Hanssen. Profiles were collected both on cross-shelf slope transects and on dedicated process stations with detailed measurements of biogeochemistry and lower trophic levels, including sampling both in the open water (ship-based) and in the marginal ice zone (either ship-based or from nearby ice floes). Microstructure shear was measured (only in May and August) using a loosely-tethered microstructure profiler MSS-90L (IWS Wassermesstechnik) with two airfoil shear probes, falling freely at a rate of $\sim$0.55 m s^{-1}. The microstructure shear is needed to obtain the vertical eddy diffusivity, K_ρ, used in calculation of nutrient fluxes (section 2.5). The microstructure sampling was made in sets of at least three consecutive repeat profiles. $\mathcal{N}$ was measured using an unpumped ISUS V3 (Satlantic), mounted on the shipboard SBE911+ (Sea-Bird Electronics, Bellevue, WA, USA) CTD (conductivity-temperature-depth) rosette system logging the analog output voltage of the ISUS. Downcast speed in the upper 200 m was 0.6 m s^{-1} and 1.0 m s^{-1} after that.

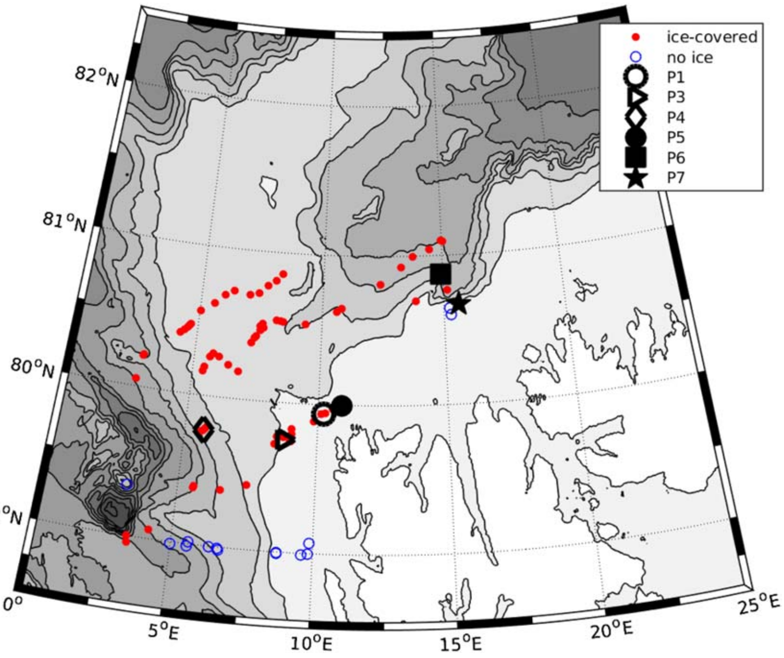

Figure 1. Location of nitrate and microstructure profiles used for $F_{\mathcal{N}}$ estimates. Bottom topography based on IBCAO V3 [*Jakobsson et al.*, 2012] and contoured at 500 m intervals. The white region is the Svalbard Archipelago.

A total of six free-drift process stations of approximately 24 h duration were conducted (location: see Figure 1) with bottle-incubation-based estimates of new and regenerated production in addition to multiple sets of microstructure data and ISUS profiles.

The fourth campaign was the N-ICE drift [*Granskog et al*., 2016], lasting from January to June 2015, based off R/V Lance, which was frozen into the ice or moored to a total of four successive ice floes during the 6 month period (with short breaks for relocation between ice camps). Sampling included at least one set of MSS casts a day (to 200–300 m depth, fall rates $\sim$0.8 m s^{-1}) and biweekly ISUS casts (to 120 m depth), with ISUS deployment frequency increasing to almost daily with the onset of the observed spring bloom in late May. Again, the ISUS was used in an unpumped configuration, mounted on a frame with an SBE19+ system that was programmed to sample the analog output voltage of the ISUS. The downcast speed during the N-ICE campaign was $\sim$0.2 m s^{-1} to meet the requirements of another instrument mounted on the same frame. Both MSS and ISUS were deployed through a hydrohole from a tent several hundred meters away from the ship.

A total of 130 ISUS profiles and 440 MSS casts were collected. In addition, three ISUS profiles across the Yermak plateau collected from R/V Polarstern in June 2015 as part of the TRANSSIZ cruise are presented to supplement the discussion of the large-scale distribution of nitrate.

2.2. Processing of MSS Data

MSS data were processed following *Fer* [2006]. Assuming local small-scale isotropy [*Yamazaki and Osborn*, 1990], dissipation of turbulent kinetic energy was estimated from the measured microscale shear as

$$\epsilon = 7.5\nu\langle(\partial_z u')^2\rangle, \tag{1}$$

where ν is the molecular viscosity of sea water and $\partial_z u'$ the turbulent shear. Resulting dissipation profiles are averaged in bins of 0.5 m. Eddy diffusivity of mass was estimated as $K_\rho = \Gamma\frac{\epsilon}{N^2}$, where the mixing efficiency is taken as $\Gamma = 0.2$ [*Osborn*, 1980] and N is the buoyancy frequency. In this study, for the flux calculations, K_ρ is obtained from the average dissipation over the depth range of the nitracline, and N from the density gradient across the nitracline (see section 2.5).

2.3. Processing of CTD and ISUS Data

CTD data were processed using standard SBE routines. To align the time stamps of ISUS and CTD, raw ISUS output logged on both ISUS and the respective CTD system were compared to find the time lag that produced the maximum correlation, and T and S records were then aligned to ISUS records. The internally logged absorption spectra were then processed mainly following *Sakamoto et al*. [2009], using their "temperature compensated, salinity subtracted" algorithm and a wave band of 217–240 nm. Resulting $\mathcal{N}$ profiles generally have a small (median 0.9 μM) depth-independent offset compared to bottle samples, but capture the vertical gradients well. Because $F_\mathcal{N}$ is obtained from vertical gradients (see section 2.5), the estimates do not depend on how the bias is determined. Details of the quality control and postprocessing procedure are deferred to Appendix A.

2.4. Nutrient Sample Analysis

For quality control and calibration, the ISUS profiles are supplemented with water sample profiles of nitrate concentrations from all campaigns, analyzed with standard methods. For CarbonBridge and TRANSSIZ, bottle samples were frozen until analysis at the University of Tromsø using a Flow Solution IV analyzer from O.I. Analytical, USA, calibrated with reference sea water from Ocean Scientific International Ltd., UK. The N-ICE nutrient samples were fixed with chloroform and stored cool until spectrophotometric analysis at the Institute of Marine Research, Norway, using a modified Skalar autoanalyzer [*Bendschneider and Robinson*, 1952]. $\mathcal{N}$ is significant to one decimal for both analyses, and detection limits are 0.02 μM for CarbonBridge and TRANSSIZ and 0.4 μM for N-ICE.

2.5. Calculation of Nitrate Fluxes

The definition of $F_\mathcal{N}$ employed in this study is $F_\mathcal{N} = K_\rho\frac{\partial\mathcal{N}}{\partial z}$, where the vertical eddy diffusivity of mass K_ρ and the vertical nitrate gradient $\frac{\partial\mathcal{N}}{\partial z}$ (defined positive upward) are both bulk quantities calculated over the nitracline. The nitracline is defined in terms of a density-scaled depth coordinate based on the CTD cast associated with the ISUS profile in order to eliminate the effect of isopycnal displacements in the calculation of K_ρ. Details are deferred to Appendix B.

All ~130 ISUS profiles collected during the four campaigns are used to present nitrate distribution patterns, covering the period from January 2014 to June 2015. The upward turbulent nitrate flux across the nitracline is quantified using a total of ~440 MSS casts and ~100 ISUS casts, resulting in a total of ~90 viable $F_\mathcal{N}$ estimates (i.e., where ISUS profiles contain a nitracline following the definition). Pooling the 2014 and 2015 data, the flux estimates cover the productive period between May and August as they are restricted to situations where the surface layer has experienced significant nitrate drawdown.

2.6. Primary Production Incubations

Water samples for incubations were taken at 0, 5, 10, 20, 30, 40, 50, and 75 m and subdivided in four 500 mL polycarbonate bottles for each depth. Two of the bottles were spiked with 15*N* ammonium chloride and two were spiked with 15*N* potassium nitrate, using the minimum amount of tracer (0.1 μM) required to get a reliable labeling signal. The bottles were hooked on a surface-tethered mooring and incubated in situ for 24 h. Incubations were terminated by filtration onto 24 mm glass microfiber filters (Whatman GF/F; vacuum pressure <250 mm Hg). All filters were desiccated at 60°C and stored dry for postcruise analysis. An elemental analyzer (ECS 4010, Costech Analytical Technologies Inc.) coupled to a mass spectrometer (Delta V Advantage, ThermoFinnigan) was used to determine isotopic enrichment and particulate organic carbon and nitrogen using a modified Dumas method (for details see *Blais et al*. [2012]). Nitrogen uptake was calculated using equation (3) of *Collos* [1987]:

$$\text{N uptake} = \left[N_f \cdot (C_p - C_0)\right] / \left[(C_d - C_0)\Delta t\right] \tag{2}$$

where N_f is the concentration of particulate organic nitrogen (μg L^{-1}), C_0 and C_p are the atom-% enrichments of the particulate material before and after the incubation, respectively, C_d is the natural 15*N* abundance (atom-%) of dissolved inorganic nitrogen at the beginning of the incubation and Δt is the duration of the incubation (h).

Ammonium concentrations were measured manually with the sensitive fluorometric method [*Holmes et al*., 1999] in order to supplement the discussion of the incubation results. Reagents were added within minutes of sample collection.

3. Results

3.1. Patterns of Upper Ocean Nitrate Distribution

Three contrasting regimes of upper ocean stratification were observed: (1) on-shelf and over the shelf slope where warm and salty AW reached up to the ice-free surface and stratification was weak, (2) late spring and summer, off-shelf and in ice-covered regions, where ice melt had led to haline stratification, and (3) winter, early spring, and deep into the pack ice/deep Arctic basin, where the surface mixed layer extended to 50–100 m depth (Figures 2–4; also note the mixed layer depths). Nitrate drawdown or even depletion was evident wherever there was significant upper ocean stratification (as signified by the density difference between surface and deeper layers; see Figure 5). Note that the two easternmost transects in Figure 2 are from different years, and the location of the ice edge and presence of stratified surface waters at the respective times (not shown) correspond well to where the vertical $\mathcal{N}$ gradient starts to appear.

Four representative profiles of hydrography, turbulent microstructure, and chlorophyll fluorescence (Figure 6) highlight both the seasonal evolution of $\mathcal{N}$ and its relation to the stratification. The two May profiles show a near-depletion of nitrate in the upper 20 m, coincident with elevated concentrations of chl-a fluorescence. The two August profiles show total depletion of surface $\mathcal{N}$ (equal zero to within measurement uncertainty) and a deepening of the nitracline which is not reflected in the pycnocline. However, the chl-a fluorescence now indicates the development of a subsurface chlorophyll maximum at the upper end of the nitracline. As opposed to the open-water profiles, the ice-covered profiles do not have a distinct surface mixed layer. Instead, sea ice melt provides a constant freshwater source that prohibits thorough mixing of the surface layer. Note that the dissipation of turbulent kinetic energy rapidly approaches background values at the base of the seasonal pycnocline, such that the August nitraclines are virtually decoupled from the wind-driven surface mixing. A more detailed description of the regional hydrography in relation to biogeochemical parameters will be reported elsewhere.

3.2. Nitrate Fluxes

The population of $F_{\mathcal{N}}$ values reported here deviates only slightly from a lognormal distribution (skewness ~0.4, kurtosis ~2.4) when excluding the top and bottom 5% quantiles to remove outliers. We therefore report $F_{\mathcal{N}}$ as the median of 1000 bootstrap iterations evaluated using a lognormal estimator (excluding eight outliers), and the associated 95% confidence interval in brackets. Pooled $F_{\mathcal{N}}$ values have a median value of 0.4 (0.3, 0.5) mmol m^{-2} d^{-1}. When calculated separately for ice-covered and open-water stations, the median values are 0.3 (0.2, 0.4) mmol m^{-2} d^{-1} and 0.7 (0.4, 1.1) mmol m^{-2} d^{-1}, respectively (see Figure 7 and Table 1).

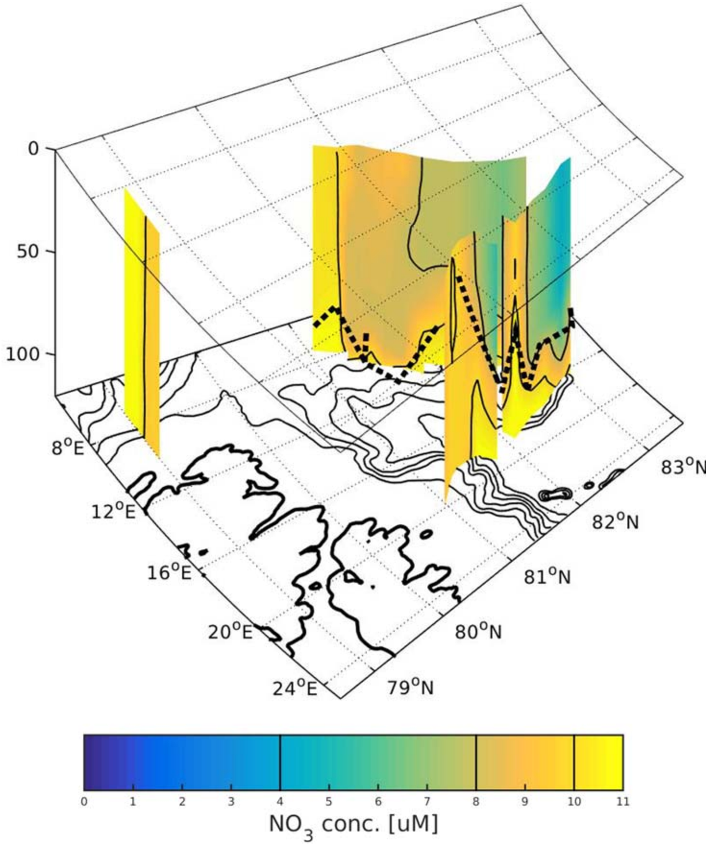

Figure 2. Curtain plots of nitrate concentration $\mathcal{N}$: Winter (N-ICE until 25 May, CarbonBridge January data). Mixed layer depth is plotted into the curtains as dotted lines.

3.3. New and Regenerated Production

Nitrate uptake determined from the incubations (integrated from the surface to halfway into the nitracline) for the May stations (P1-4) range from 2.6 to 8.4 mmol m^{-2} d^{-1}, while August stations (P5-P7) range from 0.015 to 0.048 mmol m^{-2} d^{-1} (see Tab. 2). Taking into account interpolation errors and the slight arbitrariness of the lower integration depth (± 5 m), we estimate a statistical uncertainty of approximately 10% in the uptake rates. $F_{\mathcal{N}}$ was smaller than NO_3^- uptake at the May stations, while at the August stations, $F_{\mathcal{N}}$ was more than an order of magnitude larger than uptake.

4. Discussion

4.1. Interpreting Nitrate Fluxes

Calculation and interpretation of the nitrate fluxes are hampered by (1) frequently shallow (<15 m) and complex pycnocline and nitracline structures, and (2) the frequently deeper vertical position of the nitracline relative to the pycnocline (Figure 6). (1) leads to a large degree of intermittency due to the proximity to wind forcing at the ocean surface. (2) Can be due to assimilation of nitrate under the pycnocline when the pycnocline is shallower than the euphotic zone, or because of continued ice melt which can shoal the seasonal pycnocline after the establishment of the nitracline. Therefore, although the pycnocline often presents the "bottleneck" in the upward transport of tracers due to its strong stratification, its effect on $F_{\mathcal{N}}$ in many cases is to isolate the nitracline from dissipation of wind energy [cf. *Randelhoff et al.*, 2014].

In the study area, advection of nutrients with the inflow of Atlantic Water is potentially an important process. Similarly, previous studies have pointed at the importance of eddies for the cross-slope transport of nutrients and biomass into the deep Arctic basin [e.g., *Watanabe et al.*, 2014]. Findings by *Hattermann et al.* [2016]

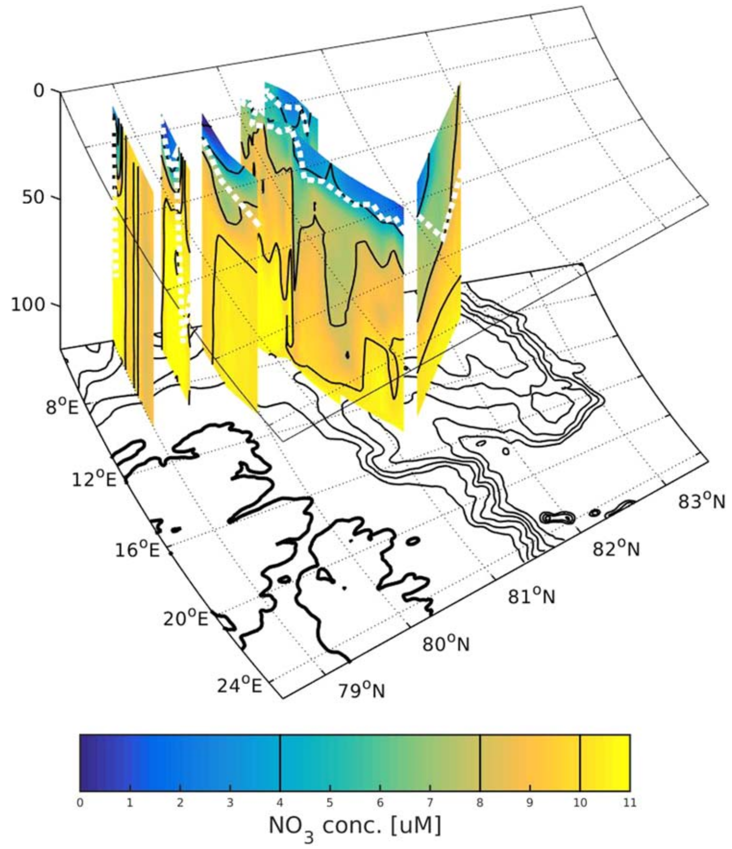

Figure 3. Curtain plots of nitrate concentration $\mathcal{N}$: Spring (N-ICE from 27 May, CarbonBridge May data, TRANSSIZ). Mixed layer depth is plotted into the curtains as dotted lines.

indicate that the Sofia Deep (the region between the Yermak Plateau and the shelf slope) does not have much eddy activity, but the western flank of the Yermak plateau does. In early spring, when differences in bloom timing lead to horizontal gradients, horizontal transport with eddies or the Atlantic Water can lead to a wide redistribution of nutrients. As the season progresses, however, surface waters become similarly depleted across the study area (Figure 4), decreasing the importance of horizontal transport. As we will show shortly, our measurements of the nitrate uptake rates do not indicate any additional supply of nitrate in late summer.

Upwelling, i.e., wind induced Ekman pumping, may lift the nitracline and bring nutrients closer to the surface. If this occurs in the summer season, local production may be temporarily increased by exposing more nitrate to sufficient radiation. However, analysis of wind curl over multiple years [*Lind and Ingvaldsen*, 2012] indicates that Ekman pumping in this area is substantially weaker in summer than in winter, when it would facilitate redistribution of nutrients in the water column rather than contribute directly to increased primary production. In slope areas where there currently is not enough vertical redistribution of nutrients to replenish the upper column in winter, enhanced upwelling may increase overall productivity. However, since the water column in the Svalbard shelf slope area is already well-mixed through large parts of the winter [see also *Randelhoff et al*., 2015], winter upwelling does not increase productivity in this area. Furthermore, the large increases in upwelling seen on the Canadian shelf [e.g., *Tremblay et al*., 2015] are also contingent on the dominant wind direction being east.

4.2. Magnitude and Spatial Patterns in Fluxes

Subsampling by season and presence of ice cover shows that the presence of ice cover has a larger influence on the magnitude of $F_{\mathcal{N}}$ (cf. Table 1) than the season. This means the seasonal variability is small as long as the ice concentrations are similar; however, the fluxes in open waters are generally larger. In August, nitraclines are deeper and less stratified, and the surface waters are more nutrient-depleted. Note that the weaker stratification in August is mostly due to the migration of the nitracline below the seasonal pycnocline. The small sample size ($n = 2$, out of seven relevant ISUS profiles with colocated MSS measurements) of open-water $F_{\mathcal{N}}$ in May demonstrates that most of the profiles do not show a sufficient amount of nitrate drawdown and hence no nitracline. Given the comparable vertical nitrate gradients in all subsamples, the consistently weaker stratification seems to be the main cause for the enhanced fluxes in open water since dissipation values show at most a small increase. Open water may allow for additional mixing processes at the surface such as gravity waves, Langmuir turbulence or enhanced input of near-inertial wind energy; however, no conclusive answer can be reached based on this data set. Most of the other external parameters relevant for mixing processes (e.g., bottom depth, tidal, and boundary current intensities, ice cover, surface stratification) largely covary with one another in this region, and attempts at separating their relative contributions have not proved fruitful in the present data set.

A frequent caveat in previous studies on turbulent nitrate fluxes in the Arctic is the small number of observations which makes the analysis prone to outliers, and renders deriving long-term averages speculative. *Sundfjord et al.* [2007] find 0.14 mmol m^{-2} d^{-1} for a rather quiescent station in the Northern Barents Sea, and contrast this with a much higher flux of 2.4 mmol m^{-2} d^{-1} at a nearby station subject to strong tidal mixing. Since these values bracket our estimates generously, we argue that they do not represent long-term or large-scale averages but might be indicative of relative geographical trends, and govern local biological processes on shorter time scales. The same is probably

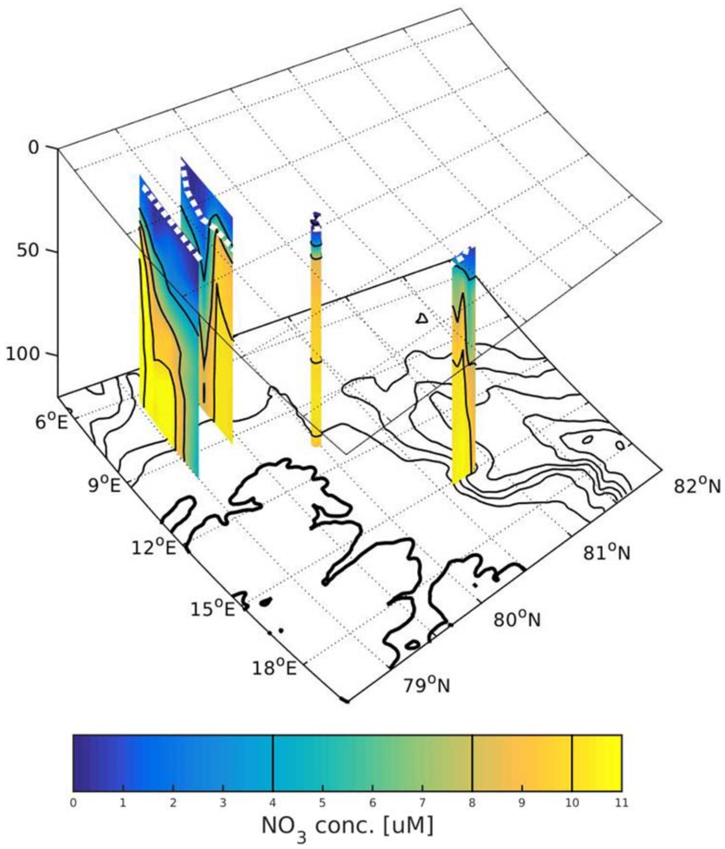

Figure 4. Curtain plots of nitrate concentration $\mathcal{N}$: Summer (CarbonBridge August data). Mixed layer depth is plotted into the curtains as dotted lines.

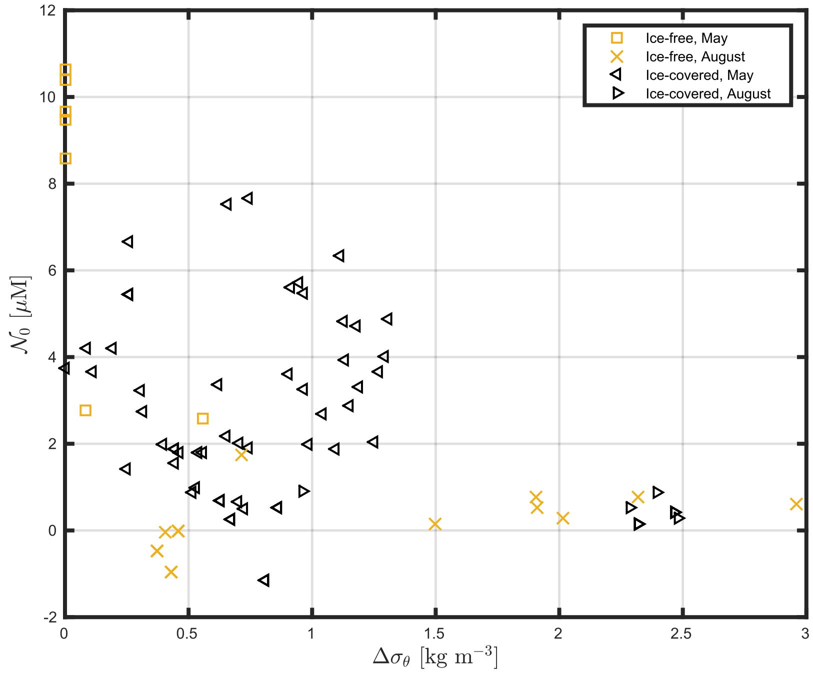

Figure 5. Surface nitrate concentration $\mathcal{N}_0$ plotted against the difference in potential density ($\Delta\sigma_\theta$) between surface and "deep" (50–60 m) water.

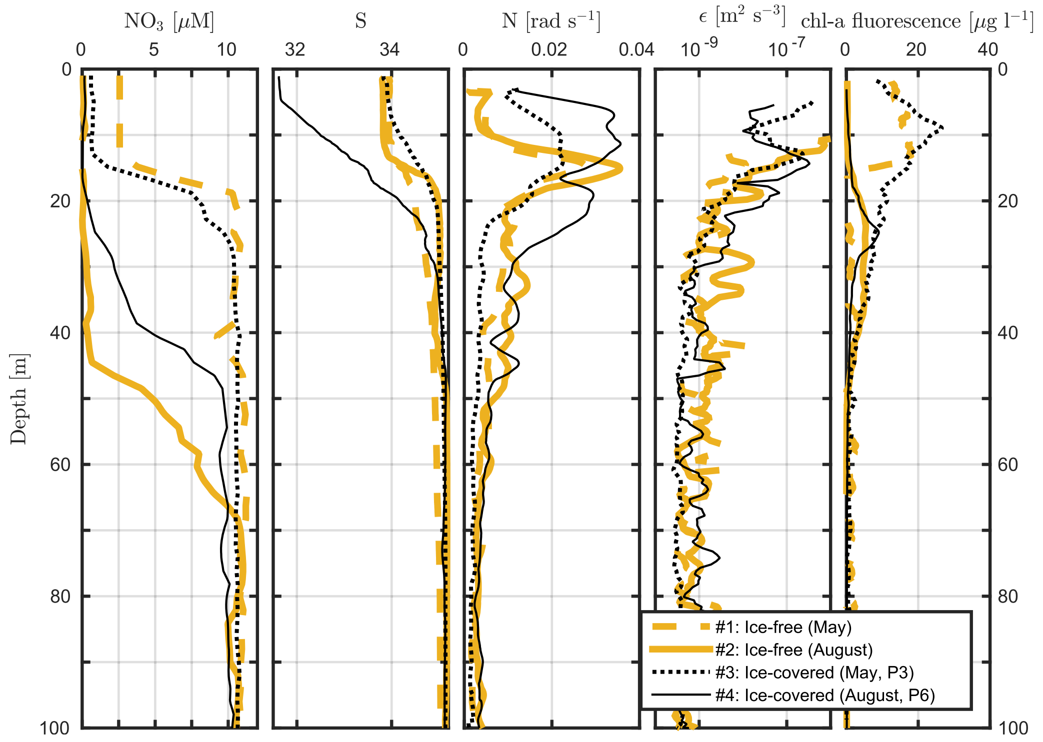

Figure 6. Four vertical profiles of NO_3^- concentration, salinity, buoyancy frequency, dissipation rate, and chl-a fluorescence highlighting aspects of the seasonality of primary productivity in the Arctic (#1, May, and #2, August: Open water, approximately 79° N, 5° E. #3: P3, #4: P6, both ice-covered, see also Figure 1). Chl-a fluorescence is uncalibrated, reported as measured by a Turner Cyclops-7 fluorometer mounted on the MSS. Note that the upper ~10 m of dissipation profiles sampled from the vessel are excluded.

true for two other estimates in the Barents Sea ($F_{\mathcal{N}} \sim 0.05$ mmol m^{-2} d^{-1} and $\sim$2 mmol m^{-2} d^{-1}, I. Wiedmann, personal communication, 2015), contrasting two different stratification regimes north and south of the Polar Front, respectively. *Bourgault et al.* [2011] estimate autumn $F_{\mathcal{N}}$ in the ice-covered southeast

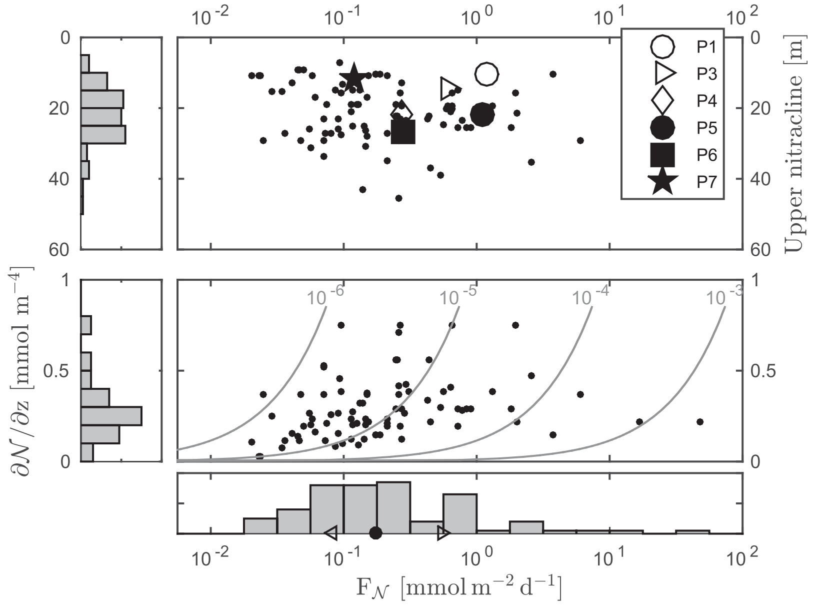

Figure 7. Histogram of nitrate fluxes. Black dot and triangles in the lower plot indicate median and 25% and 75% percentiles, respectively (see text). The grey contour lines indicate eddy diffusivity (units m^2 s^{-1}). "Upper nitracline" is the upper extent of the nitracline as determined by the algorithm described in Appendix B.

Table 1. Average Values of Selected Parameters Binned According to Ice Cover and Season[a]

	Ice Covered		No Ice	
	May	August	May	August
$F_{\mathcal{N}}$ (mmol m^{-2} d^{-1})	0.3 (0.2, 0.5)	0.2 (0.1, 0.9)	0.4	0.7 (0.4, 1.3)
ϵ ($10^{-9} \cdot$ m^2 s^{-3})	8.1 (6.3,14)	8.1 (3.4, 56)	2.8	11 (6.6, 26)
$\frac{\partial \mathcal{N}}{\partial z}$ (μM m^{-1})	0.2 (0.2, 0.4)	0.3 (0.2, 0.4)	0.32	0.3 (0.2, 0.5)
N^2 ($10^{-4} \cdot$ s^{-2})	2.0 (1.1, 3.1)	1.2 (1.0, 2.2)	0.5	0.9 (0.8, 1.2)
Δz (m)	4 (1, 8)	16 (13, 18)	0	13 (8, 17)
NO_3^- surface conc. (μM)	2 (0.8, 4.2)	0.4 (0.2, 0.5)	2.7	0.02
Sample size, n	56	12	2	18

[a] The sample size is the number of valid $F_{\mathcal{N}}$ estimates; the number of profiles might be larger (see text). "Averages" are either the median of the lognormal estimator used on 1000 bootstrap iterations ($F_{\mathcal{N}}$: vertical nitrate flux, ϵ: dissipation rate of turbulent kinetic energy in the nitracline) or the median values of all samples in the respective category for that parameter ($\frac{\partial \mathcal{N}}{\partial z}$: nitrate concentration gradient across nitracline, N^2: buoyancy frequency squared across nitracline, Δz: difference between the upper extents of the nitracline and the pycnocline (positive: nitracline deeper than pycnocline), NO_3^- surface concentration). In brackets, the 95% bootstrapped confidence interval or the first and third quartiles are given, respectively. For the two open-water profiles in May, just the mean values are given.

Beaufort Sea, and find a flux of 0.5 mmol m^{-2} d^{-1}, which is about twice as large as our estimate for $F_{\mathcal{N}}$ under ice-covered conditions. The season and regional hydrography are somewhat different and so the flux magnitudes compare reasonably well.

The vertical mixing that (together with remineralization) is responsible for restoring the prebloom nitrate pool during winter has been estimated to be slightly less than 2.5 mmol m^{-2} d^{-1} in the AW inflow [*Randelhoff et al*., 2015], likely aided by thermal convection and therefore reasonably high compared to our value. In addition, *Nishino et al*. [2015] found an upward nitrate flux of 3.5 mmol m^{-2} d^{-1} at the base of the mixed layer following several strong wind events in the northern Chukchi Sea in autumn, similarly suggesting that fall mixing might be stronger than the rather small values reported in the present study. Indeed, *Ardyna et al*. [2014] report an increase in the number of secondary late-autumn blooms which could also contribute to annual new production as a consequence of enhanced upward mixing of nitrate while there is still sufficient light. Our August cruise was probably too early to pick up any such bloom, but to our knowledge, they have so far not been investigated in the field in this area.

The data set presented in this paper covers a wide range of seasons, locations, and types of ice cover, with a large number of $F_{\mathcal{N}}$ estimates. We therefore expect that the statistics are robust and our data set can be used to constrain both observations of Arctic primary production and biogeochemical ocean circulation models.

4.3. Nitrate Uptake Rates

The fact that during May, $F_{\mathcal{N}}$ was smaller than NO_3^- uptake is consistent with the stipulation that early in the season surface $\mathcal{N}$ is large enough that it is not limiting new production, even when it is certainly approaching depletion. In addition, the nitracline is sufficiently shallow in May that nitrate demand can be

Table 2. Overview Over $F_{\mathcal{N}}$ (NO_3^- Fluxes) (Given As Bootstrap Using a Lognormal Estimator and 95% Confidence Interval in Brackets), Consumption of NO_3^- ($\int dz\ NO_3^-$ upt.) and NH_4^+ ($\int dz\ NH_4^+$ upt.) (Both (mmol m^{-2} d^{-1})), and Surface Concentrations (μM) of NO_3^- and NH_4^+ at the CarbonBridge Process Stations[a]

	$F_{\mathcal{N}}$	$\int dz\ NO_3^-$ upt.	$\int dz\ NH_4^+$ upt.	NO_3^- sfc. conc.	NH_4^+ sfc. conc.
P1	1.2 (0.2, 5.6)	2.6	1.1	2.5	0.07
P3	0.6 (0.2, 2)	3.1	5.3	0.44	0.17
P4	0.3 (0.2, 0.3)	8.4	4.8	0.33	0.05
P5	1.1 (0.7, 1.7)[b]	0.015	5.8	0.11	0.15
P6	0.3 (0.1, 0.8)	0.018	2.3	0.07	0.08
P7	0.1[c]	0.048	2.1	0.26	0.02

[a] P1-4 were conducted in May, P5-7 in August. For station locations, see Figure 1. P1 and P5 are approximately colocated. Uptake rates are integrated from the surface to halfway into the nitracline.

[b] This is after excluding the top and bottom 5% of the distribution to remove the outliers (as described in the text), all of which are located on P5. Not removing these results in an estimate 5.9 (1.5, 47) mmol m^{-2} d^{-1}, but it is difficult to assess the relative contribution of these high-mixing events due to the small sample number (n = 11 nitrate flux estimates).

[c] n = 1.

fulfilled by a net downward displacement of the standing stock, which then relies on ambient nitrate inventories to a greater extent than on $F_{\mathcal{N}}$.

Since August nutrient concentrations were extremely small, one would expect that the uptake of nitrate were bounded by its supply through vertical fluxes. However, our measurements suggest that the nitrate supplied through vertical mixing actually exceeded its uptake by a factor of more than 10. Smaller flagellates dominated the microalgal community in August. Thus although the low silicate concentration $<2\ \mu M$ (data not shown) likely inhibited growth of diatoms, it was not a limiting factor for nitrate uptake. Several other possibilities exist to explain the large discrepancy between measured values of $F_{\mathcal{N}}$ and NO_3^- uptake in August. If the measurements were to be inaccurate, the discrepancy could be either due to an overestimation of $F_{\mathcal{N}}$ or an underestimation of NO_3^- uptake. It seems implausible that the mixing efficiency used in the estimation of the eddy diffusivity would be consistently that much smaller than the value of 0.2 we used in this study (see section 2.2). At low $\mathcal{N}$, one might think that NO_3^- uptake during the incubation will make NO_3^- limitation even stronger, but the measured uptake rate is still orders of magnitude far from depleting the nitrate pool during the 24 h incubation period.

The lack of turbulence in the incubation bottles might artificially reduce the uptake rate. Indeed, *Aksnes and Egge* [1991] argue for an extension of NO_3^- uptake Michaelis-Menten kinetics that includes a toward-cell diffusive transport coefficient. At low nutrient concentrations, this implies a linear dependence on turbulent shear levels, which might account for the order-of-magnitude discrepancy between inside-bottle and hypothetical outside-bottle uptake rates.

It is worth noting that NH_4^+ uptake rates were two orders of magnitude higher than NO_3^- uptake rates at the surface of stations P5 and P6 (not shown but see Table 2 for integrated rates), despite the evenness of incubation conditions and ambient concentrations for the two nitrogen sources. This pattern suggests a strong preference of the community for reduced nitrogen and/or intense recycling within the incubation bottles. Under strong recycling, the nitrogen initially taken up as nitrate may not accumulate in phytoplankton biomass, either supporting a fast turnover of NH_4^+ or a transient build-up of dissolved organic pools (not measured here). In addition, previous studies have shown that net nitrate uptake (i.e., the accumulation of N in particulate matter) by phytoplankton may represent as little as 26% of gross nitrate uptake [*Bronk and Ward*, 2000], but this was not assessed here. In the case of preference, the upward supply of nitrate would lead to a progressive accumulation of NO_3^- into the euphotic zone, but this cannot be confirmed in the absence of Lagrangian sampling. Furthermore, the increase would be hardly noticeable over the involved timescales (for instance, a surplus of 0.5 mmol $m^{-2}\ d^{-1}$ distributed over 20 m depth corresponds to an increase of 0.75 μM $month^{-1}$).

If the inside-bottle uptake rates are indeed representative of the "real" uptake rates outside the bottles even in August, we will have to revise our hypothesis that new production is limited by NO_3^- availability. However, we have not found a compelling explanation for this scenario.

4.4. New Production

To put our flux estimates into context, assuming a Redfield C:N ratio of 106:16, $F_{\mathcal{N}} \approx 0.3 \text{mmol m}^{-2}\ \text{d}^{-1}$ would correspond to a new production of ~0.7 g C m^{-2} $month^{-1}$, amounting to approximately 3 g C m^{-2} during the summer season. Compared to nitrate-based estimates of yearly new production of around 47 g C m^{-2} (Barents Sea shelf), 31 g C m^{-2} (shelf slope) and 13 g C m^{-2} (Eurasian Basin) [*Codispoti et al*., 2013; *Randelhoff et al*., 2015], the vertical flux during summer only plays a small role in determining the annual nitrate drawdown on the productive shelves, and that (a) preconditioning (filling up the prebloom reservoir of nitrate) and (b) the development of a subsurface chlorophyll maximum account for most of the annual nitrate drawdown. Thus the increase in net primary production in the Barents Sea reported by *Arrigo and van Dijken* [2015] might represent mostly an increase in regenerated production, not supporting additional carbon export. The new production in summer might, however, represent a significant fraction of the annual nitrate drawdown in the Eurasian Basin and thus exert an important control on the export production there, including the modification of geochemical nutrient and carbon cycles. Strengthening of the perennial, deep stratification (for instance, between AW and the Polar Mixed Layer in the Eurasian Basin) by changing freshwater budgets [see e.g., *Nummelin et al*., 2015] is an altogether different issue and only marginally related to seasonal sea ice melt, and left to further studies.

At any rate, it can be expected that the magnitude of $F_{\mathcal{N}}$ will determine the extent to which a community enters a recycling (NH_4^+ -dependent) state postbloom, or that a smaller $F_{\mathcal{N}}$ favors smaller phytoplankton with higher affinity for reduced nitrogen resources [e.g., *Li et al*., 2009; *Sommer et al*., 2016]. This is also reflected in our observations: the phytoplankton community in May/June was dominated by a combination of both the haptophyte *Phaeocystis pouchetii* and larger diatoms (Carbon Bridge May cruise), or completely by *P. pouchetii* (N-ICE; P. Assmy, personal communication, 2016). In August, however, smaller flagellates dominated the phytoplankton community, probably in response to low nutrient concentrations. The relatively low values of $F_{\mathcal{N}}$ are therefore important because they help to produce these oligotrophic conditions.

5. Summary and Perspectives

Based on this study, we draw the following conclusions: (a) close to the shelf, upper ocean $\mathcal{N}$ is homogeneous with depth at approximately 10 μM, from early winter until the bloom starts. In the deep basin, permanent nitrate stratification exists also prebloom (albeit across a deep pycnocline), with surface mixed layer $\mathcal{N}$ as low as approximately 5 μM. (b) The $\mathcal{N}$ drawdown in the photic zone is empirically strongly related to the development of seasonal stratification from ice melt. This agrees with Sverdrup's critical mixing theory [*Sverdrup*, 1953] and is presumably related to reduction in eddy diffusivity with increasing stratification, which increases residence time of individual phytoplankton cells in the low-light photic zone of the Arctic Ocean. (c) Upward turbulent nitrate fluxes across the seasonal nitracline in the study area are small (~0.3 mmol m^{-2} d^{-1} in ice-covered areas, and about twice as much in ice-free conditions) compared to overall estimates of annual NO_3^- drawdown.

Comparison with estimates of late summer NO_3^- uptake was inconclusive. We have not found a compelling explanation for what else might have limited NO_3^- accumulation in particulate matter by an order of magnitude more than $F_{\mathcal{N}}$, and it is possible that the bottle incubation technique underestimated NO_3^- uptake. However, we observed a strong uptake preference for NH_4^+, and the corresponding increase in $\mathcal{N}$ would be small and hard to detect even with dedicated sampling schemes.

On a pan-Arctic scale, the near-surface warm AW inflow along the shelf slope is a regional anomaly. In the context of this study, AW heat leads to stronger melt rates [*Onarheim et al*., 2014] and therefore earlier onset of stratification and might thus be indirectly linked to bloom development (cf. point (b) above). However, we expect that much of the seasonal upper ocean hydrography and accordingly nitrate fluxes are governed by similar mechanisms across the ice-covered Arctic, with local adjustments for different melt rates, thus vertical density gradients, and different nitrate concentration gradients.

The vertical nitrate fluxes presented here could entail an increase in new production of a few g C m^{-2} under the transition to a seasonal ice cover, with ensuing changes in boundary layer stratification being the biggest driver. This would be a significant fraction of the current export production in the deep Eurasian Basin, but hardly noticeable on the productive shelves.

Appendix A: ISUS Data Processing and Quality Control

Some ISUS profiles show clear signs of "nitrate spiking" when the CTD traverses a halo or thermocline (akin to salinity spiking known from standard CTD processing procedures), indicating (1) some degree of misalignment between ISUS and T-S records, and (2) low-pass effects stemming from using the ISUS in an unpumped configuration. While these features could be somewhat relieved by adjusting the ISUS lag for individual casts (introduced to account for the combined effect of differing heights of the sensors on the instrument package and the T-S package being pumped), finding objective criteria proved difficult, presumably among other things due to different horizontal velocities of the instrument package relative to the surrounding water, leading to variable turnover times of the water parcel in the sensor tip. However, averaging vertically in 2 m bins, bulk $\mathcal{N}$ gradients in the nitracline are found to be virtually independent of the specific choice of the time lag within a few seconds.

Most often, a depth-independent bias in computed $\mathcal{N}$ was detected from comparison with bottle samples taken during the same CTD casts during the CarbonBridge campaigns, the ISUS being biased high by about 0 to 2μM on a per-campaign basis (cf. Figure 8). Each profile was then adjusted by subtracting a

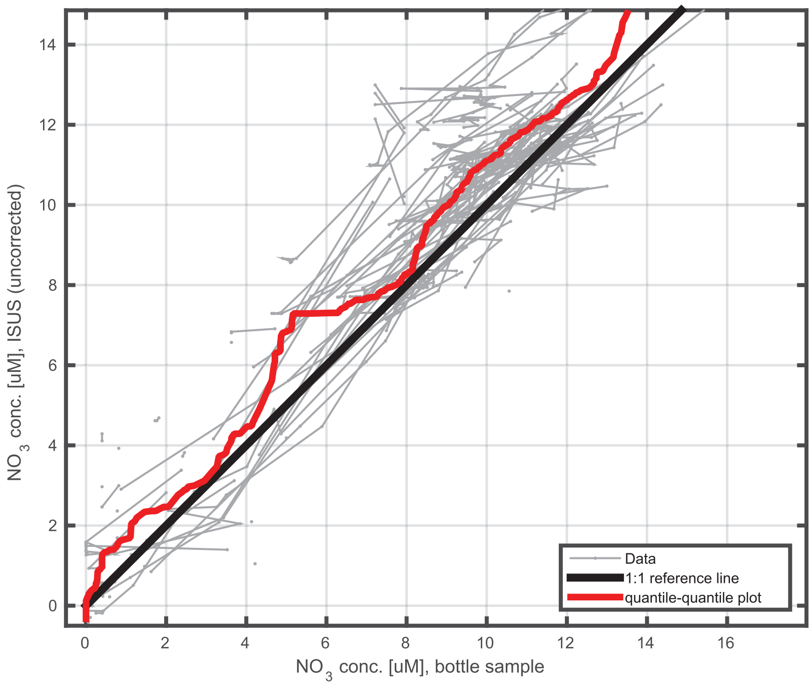

Figure 8. $\mathcal{N}$ from ISUS versus bottle samples. Individual profiles are connected by thin lines. Note that these ISUS concentration values are not corrected against bottle samples.

constant offset, determined for each profile individually as the average offset between bottle samples and ISUS.

For the N-ICE campaign, bottle samples were generally farther removed from ISUS profiles, both in time and accordingly in space. For all profiles, manually selected bottle sample profiles sufficiently close in space, T-S properties, and vertical $\mathcal{N}$ structure were compared to judge and correct for a depth-independent bias. In some instances, profiles lacking good quality data in the uppermost few tens of meters (presumably due to either turbid waters or instrument lamp warmup issues) were extrapolated using the bottle profile given that these were sufficiently close in T-S properties.

Quantiles of profile-wise RMSEs between ISUS and bottle samples were 0.4, 0.9, 1.2, and 3.5 μM (in this order: median corrected and uncorrected and 95% quantile corrected and uncorrected). A quantile-quantile plot (see Figure 8) further demonstrates that the ISUS has a tendency to overestimate bottle $\mathcal{N}$ (slight offset above the 1:1 reference line), but importantly no systematic deviation from a linear response (as indicated by the 1:1 slope).

Final profiles of $\mathcal{N}$ were produced at 2 m resolution. The resulting $\mathcal{N}$ profiles from all campaigns were visually quality-controlled.

Appendix B: Nitracline Detection and Estimation of the Vertical Turbulent Nitrate Flux

The nitracline is defined as the depth interval where $\mathcal{N}$ crosses from 20% to 80% of the $\mathcal{N}$ difference between the surface value (calculated across 3–8 m) and a "deep" reference value (calculated across 50–60 m). The 50–60 m depth interval was selected after inspection of all potential density (σ_θ) profiles included in this study. The pycnocline is defined similarly for σ_θ, except, in order to account for the strong near-surface stratification, the surface value is calculated as the average between 3 m and the depth where the buoyancy frequency N exceeds $2 \cdot 10^{-3}$ s^{-1} for the first time. A density-scaled depth coordinate $r_\sigma = (\sigma_\theta(z) - \sigma_\theta(\mathrm{sfc}))/\Delta\sigma_\theta$ is introduced which corresponds to how much of the density difference $\Delta\sigma_\theta$ between "surface" and "deep" value the density profile has crossed, such that it is always 0 in the surface and 1 below 60 m. $\frac{\partial \mathcal{N}}{\partial z}$ is the slope of the linear regression of $\mathcal{N}$ against depth over the nitracline. For an individual profile, K_ρ is calculated as $0.2\epsilon/N^2$, where ϵ

is the mean of all dissipation values across the nitracline for a given profile, and the buoyancy frequency N is calculated using the density gradient obtained from a least-squares regression of σ_θ against depth for each profile. To ensure that variations in depths of isopycnals between individual profiles do not disturb the averages by including elevated near-surface values of K_ρ, the nitracline is expressed as an interval of r_σ (based on the density profile associated with the CTD+ISUS cast), and the nitracline in an MSS profile is defined as the same r_σ interval, based on the σ_θ profile associated with the MSS cast. This definition of isopycnals ensures that drift in the conductivity cells does not lead to a bias in the densities and thus to artificial isopycnal excursions. Since surface layer values are calculated between 3 and 8 m depth, we do not expect ship-based CTD salinities to be significantly biased high due to ship disturbance, relative to ice-floe-based MSS profiles.

Acknowledgments
CarbonBridge data collection and A.R.'s work was supported through the project CARBON BRIDGE: Bridging marine productivity regimes: How Atlantic advective inflow affects productivity, carbon cycling, and export in a melting Arctic Ocean, a Polar Programme (project 226415) funded by the Norwegian Research Council. N-ICE data collection was supported by the Norwegian Polar Institutes Centre for Ice, Climate and Ecosystems (ICE) through the N-ICE project, with additional support from the Ministry of Climate and Environment, and Ministry of Foreign Affairs of Norway. The ISUS deployments from R/V Polarstern were conducted during the ARKXXIX/1-PS92 TRANSSIZ cruise (Transitions in the Arctic Seasonal Sea Ice Zone), grant no. AWI_PS92_00. We thank the captains and crews of R/Vs Helmer Hanssen, Lance and Polarstern, and all the scientists involved in the field campaigns for their support. Svein Kristiansen analyzed the nitrate samples for the CarbonBridge and TransSIZ campaigns. We thank two anonymous reviewers for their comments. The data published in this article will be made accessible through the Norwegian Polar Data Centre (data.npolar.no) and the Norwegian Marine Data Centre (www.nmdc.no).

References

Aksnes, D., and J. Egge (1991), A theoretical model for nutrient uptake in phytoplankton, *Mar. Ecol. Prog. Ser.*, *70*(1), 65–72.

Ardyna, M., M. Babin, M. Gosselin, E. Devred, L. Rainville, and J.-E. Tremblay (2014), Recent Arctic Ocean sea ice loss triggers novel fall phytoplankton blooms, *Geophys. Res. Lett.*, *41*, 6207–6212, doi:10.1002/2014GL061047.

Arrigo, K. R., and G. L. van Dijken (2015), Continued increases in Arctic Ocean primary production, *Prog. Oceanogr.*, *136*, 60–70, doi:10.1016/j.pocean.2015.05.002.

Bendschneider, K., and R. Robinson (1952), A new spectrophotometric method for the determination of nitrite in sea water, *J. Mar. Res.*, *11*, 87–96.

Blais, M., J.-E. Tremblay, A. D. Jungblut, J. Gagnon, J. Martin, M. Thaler, and C. Lovejoy (2012), Nitrogen fixation and identification of potential diazotrophs in the Canadian Arctic, *Global Biogeochem. Cycles*, *26*, GB3022, doi:10.1029/2011GB004096.

Bourgault, D., C. Hamel, F. Cyr, J.-E. Tremblay, P. S. Galbraith, D. Dumont, and Y. Gratton (2011), Turbulent nitrate fluxes in the Amundsen Gulf during ice-covered conditions, *Geophys. Res. Lett.*, *38*, L15602, doi:10.1029/2011GL047936.

Bronk, D. A., and B. B. Ward (2000), Magnitude of dissolved organic nitrogen release relative to gross nitrogen uptake in marine systems, *Limnol. Oceanogr.*, *45*(8), 1879–1883, doi:10.4319/lo.2000.45.8.1879.

Codispoti, L., V. Kelly, A. Thessen, P. Matrai, S. Suttles, V. Hill, M. Steele, and B. Light (2013), Synthesis of primary production in the Arctic Ocean: III. Nitrate and phosphate based estimates of net community production, *Prog. Oceanogr.*, *110*, 126–150, doi:10.1016/j.pocean.2012.11.006.

Collos, Y. (1987), Calculations of 15N uptake rates by phytoplankton assimilating one or several nitrogen sources, *Int. J. Rad. Appl. Instrum. A*, *38*(4), 275–282, doi:10.1016/0883-2889(87)90038-4.

Dugdale, R. C., and J. J. Goering (1967), Uptake of new and regenerated forms of nitrogen in primary productivity, *Limnol. Oceanogr.*, *12*(2), 196–206, doi:10.4319/lo.1967.12.2. 0196.

Eppley, R., and B. Peterson (1979), The flux of particulate organic matter to the deep ocean and its relation to planktonic new production, *Nature*, *282*, 677–680.

Fer, I. (2006), Scaling turbulent dissipation in an Arctic fjord, *Deep Sea Res., Part II*, *53*, 77–95, doi:10.1016/j.dsr2.2006.01.003.

Granskog, M., P. Assmy, S. Gerland, G. Spreen, H. Steen, and L. Smedsrud (2016), Arctic research on thin ice: Consequences of Arctic sea ice loss, *Eos Trans. AGU*, *97*, doi:10.1029/2016eo044097.

Hattermann, T., P. E. Isachsen, W.-J. von Appen, J. Albretsen, and A. Sundfjord (2016), Eddy-driven recirculation of Atlantic water in Fram Strait, *Geophys. Res. Lett.*, *43*, 3406–3414, doi:10.1002/2016GL068323.

Holmes, R. M., A. Aminot, R. Kérouel, B. A. Hooker, and B. J. Peterson (1999), A simple and precise method for measuring ammonium in marine and freshwater ecosystems, *Can. J. Fish. Aquat. Sci.*, *56*(10), 1801–1808, doi:10.1139/f99-128.

Jakobsson, M., et al. (2012), The International Bathymetric Chart of the Arctic Ocean (IBCAO) Version 3.0, *Geophys. Res. Lett.*, *39*, L12609, doi:10.1029/2012GL052219.

Li, W. K. W., F. A. McLaughlin, C. Lovejoy, and E. C. Carmack (2009), Smallest algae thrive as the Arctic Ocean freshens, *Science*, *326*(5952), 539–539, doi:10.1126/science.1179798.

Lind, S., and R. B. Ingvaldsen (2012), Variability and impacts of Atlantic Water entering the Barents Sea from the north, *Deep Sea Res., Part I*, *62*, 70–88, doi:10.1016/j.dsr.2011.12.007.

Nishino, S., Y. Kawaguchi, J. Inoue, T. Hirawake, A. Fujiwara, R. Futsuki, J. Onodera, and M. Aoyama (2015), Nutrient supply and biological response to wind-induced mixing, inertial motion, internal waves, and currents in the northern Chukchi Sea, *J. Geophys. Res. Oceans*, *120*, 1975–1992, doi:10.1002/2014JC010407.

Nummelin, A., M. Ilicak, C. Li, and L. H. Smedsrud (2015), Consequences of future increased Arctic runoff on Arctic Ocean stratification, circulation, and sea ice cover, *J. Geophys. Res. Oceans*, *121*, 617–637, doi:10.1002/2015JC011156.

Onarheim, I. H., L. H. Smedsrud, R. B. Ingvaldsen, and F. Nilsen (2014), Loss of sea ice during winter north of svalbard, *Tellus Ser. A*, *66*, doi:10.3402/tellusa.v66.23933.

Osborn, T. R. (1980), Estimates of the local rate of vertical diffusion from dissipation measurements, *J. Phys. Oceanogr.*, *10*(1), 83–89, doi:10.1175/1520-0485(1980)010<0083:EOTLRO>2.0.CO;2.

Randelhoff, A., A. Sundfjord, and A. H. H. Renner (2014), Effects of a shallow pycnocline and surface meltwater on sea ice-ocean drag and turbulent heat flux, *J. Phys. Oceanogr.*, *44*(8), 2176–2190, doi:10.1175/jpo-d-13-0231.1.

Randelhoff, A., A. Sundfjord, and M. Reigstad (2015), Seasonal variability and fluxes of nitrate in the surface waters over the Arctic shelf slope, *Geophys. Res. Lett.*, *42*, 3442–3449, doi:10.1002/2015GL063655.

Sakamoto, C. M., K. S. Johnson, and L. J. Coletti (2009), Improved algorithm for the computation of nitrate concentrations in seawater using an in situ ultraviolet spectrophotometer, *Limnol. Oceanogr. Methods*, *7*, 132–143.

Sommer, U., K. H. Peter, S. Genitsaris, and M. Moustaka-Gouni (2016), Do marine phytoplankton follow Bergmanns rule sensu lato?, *Biol. Rev.*, doi:10.1111/brv.12266, in press.

Stroeve, J. C., M. C. Serreze, M. M. Holland, J. E. Kay, J. Malanik, and A. P. Barrett (2011), The Arctics rapidly shrinking sea ice cover: A research synthesis, *Clim. Change*, *110*(3-4), 1005–1027, doi:10.1007/s10584-011-0101-1.

Sundfjord, A., I. Fer, Y. Kasajima, and H. Svendsen (2007), Observations of turbulent mixing and hydrography in the marginal ice zone of the Barents Sea, *J. Geophys. Res.*, *112*, C05008, doi:10.1029/2006JC003524.

Sverdrup, H. (1953), On conditions for the vernal blooming of phytoplankton, *ICES J. Mar. Sci.*, *18*(3), 287–295.

Torres-Valdés, S., T. Tsubouchi, S. Bacon, A. C. Naveira-Garabato, R. Sanders, F. A. McLaughlin, B. Petrie, G. Kattner, K. Azetsu-Scott, and T. E. Whitledge (2013), Export of nutrients from the Arctic Ocean, *J. Geophys. Res. Oceans*, *118*, 1625–1644, doi:10.1002/jgrc.20063.

Tremblay, J.-E., et al. (2011), Climate forcing multiplies biological productivity in the coastal Arctic Ocean, *Geophys. Res. Lett.*, *38*, L18604, doi:10.1029/2011GL048825.

Tremblay, J.-E., L. G. Anderson, P. Matrai, P. Coupel, S. Bélanger, C. Michel, and M. Reigstad (2015), Global and regional drivers of nutrient supply, primary production and CO2 drawdown in the changing Arctic Ocean, *Prog. Oceanogr.*, *139*, 171–196, doi:10.1016/j.pocean.2015.08.009.

Watanabe, E., et al. (2014), Enhanced role of eddies in the Arctic marine biological pump, *Nat. Commun.*, *5*, 3950, doi:10.1038/ncomms4950.

Yamazaki, H., and T. Osborn (1990), Dissipation estimates for stratified turbulence, *J. Geophys. Res.*, *95*(C6), 9739–9744, doi:10.1029/JC095iC06p09739.